Precision Measurement of Radiative Neutron Decay

by

Matthew J. Bales

A dissertation submitted in partial fulfillment
of the requirements for the degree of
Doctor of Philosophy
(Physics)
in the University of Michigan
2014

Doctoral Committee:

Professor Timothy E. Chupp, Chair
Assistant Professor Christine A. Aidala
Professor Zhong He
Professor Georg A. Raithel

2014

This dissertation is dedicated to my patient and supportive wife,
Amanda.
She has suffered many Michigan winters to see this work done and I could not
have completed it without her.

Acknowledgments

Tim Chupp, my advisor, has supported me in every step of my graduate studies, including advising me in research, teaching, and my future career path. I am eternally thankful that he was randomly assigned as my faculty contact and that he wisely asked me to work with him during my first week at the University of Michigan.

I'd like to thank the other members of my doctoral committee: Georg Raithel, Christine Aidala, and Zhong He. Although none of them were members of my preliminary committee, they all readily agreed to serve in my defense and I thank them for their valuable time.

I also thank the entire RDK II Collaboration and in particular "the regulars:" Jeff Nico for always patiently answering my questions and for his constant support. Also for the help of his friend, the "Masked Possum." Tom Gentile for keeping us on task when we wander afield, for encouraging me to give conference talks, and for including me in hands-on-work at Brookhaven. You made a simulationist feel like an experimentalist! Herbert Breuer for his detailed virtual tours of the RDK II apparatus and for always providing brainstorming when we needed it. Kevin Coakley for being patient with me while explaining statistics and for teaching me the importance of precision (or is it accuracy?) in what I say. Ben O'Neill for being my only fellow RDK II student for so long. Rob Cooper for coming before me and paving the way and for his advice on the path ahead.

My gratitude to my group-mate, Skyler, for many far-roaming conversations. I'm sure I will be seeking your sage wisdom shortly in my work in Munich.

Thank you to all the friends I made first year: Sarah, Langechuan, Ryo, Bo, Kevin, Grant, Tim, Melinda, Li, Alex, Ben, Chao, Paul, and Joe. In particular Kevin and Michelle who have been my great friends and fellow commiserators through the years. I really don't think I could have made it through graduate school without you two.

Thank you to all the people in our the weekly roleplaying and boardgames group: Craig, Mark, Dan, Kevin, Michelle, and Amanda. Or should I say: Bell, Kasib, Garrett, Carric, Divya, and Kethria? In either case, it was always a blast telling stories with you. Through it, I made a really solid and awesome group of friends that I will be very sad to travel so far away from. Also: KAAAAZZZZZZ!

Thank you to Sandor and Katie for your nerdy board game nights and good company.

To all my former coworkers and friends from a little medical start-up (Dave, Don, Lane, Garret, Oleg, Craig, Chris, Emily, Krista, Khounma, Keo, Tana, Jason, Clay, and everyone), thank you. The lessons I learned there, both professional and personal, have served me well in graduate school.

TABLE OF CONTENTS

LIST OF FIGURES

LIST OF TABLES

LIST OF APPENDICES

LIST OF ABBREVIATIONS

APD avalanche photodiode

BGO bismuth germanium oxide

BNL Brookhaven National Laboratory

CKM Cabibbo-Kobayash-Maskawa

DAQ data acquisition

ep electron and proton coincidence

epγ electron, proton, and photon/gamma coincidence

F Fermi

FWHM full width half maximum

GT Gamow-Teller

HPC high performance computing

HPGe high purity germanium

IB inner bremsstrahlung

ILL Institut Laue-Langevin

JTW Jackson, Treiman, and Wyld

LAAPD large-area avalanche photodiode

LANL Los Alamos National Laboratory

MC Monte Carlo

MCA multi-channel analyzer

MCP microchannel-plate

MCNP Monte Carlo N-Particle

NCNR NIST Center for Neutron Research

NIST National Institute of Standards and Technology

NSLS National Synchrotron Light Source

ODE ordinary differential equation

ORNL Oak Ridge National Laboratory

PCI peripheral component interconnect

PDG Particle Data Group

PMT photomultiplier tube

QCD quantum chromodynamics

QED quantum electrodynamics

RDK a radiative decay experiment/collaboration name

RK4 Runge-Kutta method

SBD surface barrier detector

SCA single channel analyzer

SM Standard Model

SURF Synchrotron Ultraviolet Radiation Facility

TAC time-to-amplitude convertor

UCN ultra cold neutron

V–A vector minus axial vector

ABSTRACT

Precision Measurement of Radiative Neutron Decay

by

Matthew J. Bales

Chair: Timothy Chupp

The theory of quantum electrodynamics (QED) predicts that a neutron's decay into a proton, electron, and anti-neutrino will be accompanied by a radiative photon spectrum. While neutron decay is a prototypical example of weak decay, detection of its radiative photons has been difficult to measure due to strong sources of background photons related to neutron capture and neutron production. By the simultaneous detection of a prompt photon and electron followed by a delayed proton, the RDK II experiment was able to reliably identify radiative neutron decays relative to non-radiative decays in the photon energy range of approximately 0.5 keV to the 782 keV endpoint. RDK II serves as not only a test of QED but as a stepping stone towards an improved measurement of radiative neutron decay, which could test quantum chromodynamics (QCD) and beyond the SM theories. In this dissertation, the relevant theory is introduced first, followed by a detailed description of the RDK II experimental apparatus. The author's primary contribution to the experiment, a MC simulation of the apparatus, is then discussed. Next, a preliminary analysis of the experimental data is compared to the simulated data. This comparison shows good agreement between the two data sets across many relevant experimental parameters. Finally, future experiments and analysis related to RDK II are examined.

CHAPTER 1

History and Theory

In this chapter, the RDK II radiative neutron decay experiment is introduced before discussing in general the neutron, its decay, and its radiative decay. Historical discoveries are covered briefly (see Frank [1, 2] for additional detail) for and are used to introduce relevant theoretical topics. Knowledge of basic quantum field theory is presumed and is better learned from other sources [3, 4]. Finally, previous radiative decay experiments are discussed.

1.1   Introduction

The topic of this dissertation is the RDK II experiment which measured radiative photons originating from the beta decay of the free neutron. RDK is not an acronym but instead simply a play on the words "radiative decay". While radiative decays have been measured in nuclear systems for some time, only recently, in 2006 [5, 6], has it been measured in the free neutron. The decay of the free neutron through the weak interaction has the potential to test many aspects of the Standard Model (SM) of physics [2].

While RDK II is primarily a test of the theory of quantum electrodynamics (QED), an improved experiment, with an uncertainty in its measurement of the branching of below 1%, could test the direct emission from the weak vertex including recoil order corrections [7]. A future experiment could also investigate the Dirac structure of the weak current by measuring the polarization of radiative decay from polarized neutrons [7–9]. Furthermore, improved statistics and uncertainties at higher radiative photon energies could test a possible source of time-reversal violation [10, 11].

The RDK II collaboration includes scientists working at the National Institute of Standards and Technology (NIST) laboratories, Arizona State University, the University of Tulane, the University of Maryland, the University of Indiana, and the University of Michigan. The experiment ran on the NIST Center for Neutron Research (NCNR) neutron beamline

from December 2008 until November 2009. The past five years have been spent analyzing the experimental data and creating simulations of the experimental apparatus. The result of this work will be a measurement of radiative photon spectrum which spans three decades of energy scale and which will be the most precise measurement of the neutron's radiative branching ratio over any energy range. This work, while almost complete, is waiting for key contributions from collaborators to be completed before a measured value can be stated. This dissertation contains both experimental and simulated data which should be considered preliminary, but should be very close to RDK II's final published values.

1.2   The Neutron

While neutrons have existed since around ten microseconds after the Big Bang or 13.8 billion years ago [12], it wasn't until 1920 A.D that the human species first postulated their existence. Ernest Rutherford predicted their presence as a way of explaining the differences seen between the chemical properties of the elements and their masses [13]. This prediction turned out to be correct, though he was mistaken in his prediction that the neutron was simply a proton with a nuclear electron.

This incorrect model of the neutron persisted until a mysterious radiation entered the scene. First Walter Bothe and Herbert Becker in 1931 [14] and then Irene Joliot-Curie and Frédéric Joliot in 1932 [15] found evidence of a new radiation produced from alpha particles striking light elements. This radiation was found to be highly penetrating and ejected protons from hydrogenic substances. At first it was presumed this radiation was simply a high energy gamma ray.

Then, in 1932, James Chadwick, a student of Ernest Rutherford, performed a series of experiments [16] that provided evidence that this radiation was in fact from a massive neutral particle, the neutron. The neutron explained both the mass differences in matter and the properties of the mysterious radiation. After this discovery, Chadwick urged further research to determine what the neutron's substructure was, if any, and to describe the neutron's short range forces [17].

In the coming years, a veritable zoo of particles was discovered: muons, pions, kaons, etas, and anti-protons. This zoo was reduced when, in 1964, Gell-Mann [18] and Zweig [19] independently proposed that hadrons (mesons and baryons) were in fact composed of sub-nucleonic particles called quarks. It is now known that the neutron is a baryon formed from three valence quarks, two down quarks and one up quark. These quarks are bound together by gluons, carriers of the strong interaction. The neutron's mass is 939.565379±0.000021 MeV [20] with 9.4 MeV of this mass taken up by the valence
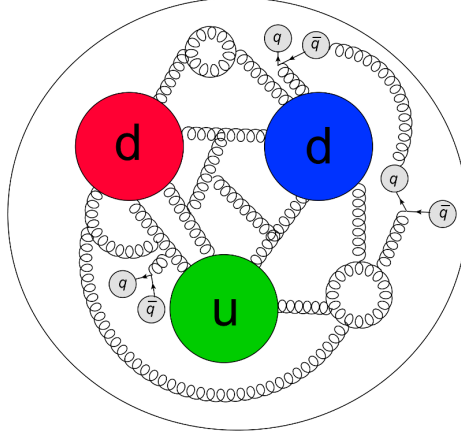
Figure 1.1: A cartoon of the modern view of what a neutron is made of. A neutron in the SM is known to be composed of three valence quarks (large for emphasis only) bound together by self-interacting gluons. Quark-anti-quark pairs can pop in and out of existence. The true composition of a neutron or any hadron is probabilistic.

quarks. The remaining 930 MeV of mass resides in the gluons and the sea of quark/anti-quark pairs (see Figure 1.1).

1.3 Neutron Beta Decay

In 1899, Rutherford observed two different forms of radiation emitted by radioactive atoms. He called them alpha and beta rays [21]. Soon Becquerel was able to identify these beta rays as electrons [22] and that they had an inhomogeneous velocity spectrum. From momentum conservation, this created a contradiction as decays into two particles should produce discrete energies. Thus the idea of a "massless" third decay product, the neutrino, was born in a letter from Pauli in 1930 [23]. This was expanded into a theory of beta decay by Fermi in 1934 [24]. His theory presumed that neutrons decayed into protons, electrons, and neutrinos. However the theoretical underpinnings were difficult to determine as experimental measurements had only been performed with complex radioactive nuclei.

In the neutron, further experiments by Chadwick and Goldhaber [25] in 1934 demonstrated that the mass of the neutron was ever so slightly greater than that of the proton. They did this by examining the photo-disintegration of the deuteron. This implied that the neutron was energetically allowed to decay into a proton, though the small size of the difference also makes detecting the decay much more difficult. The first reason it makes it more difficult is that it causes the neutron to have a relatively long lifetime, about fifteen minutes. The second reason is that it causes the neutron decay products to have relatively

low kinetic energies (< 782 keV). This issue is further compounded by strong sources of background that typically accompany strong sources of neutrons. It took fourteen years for these challenges to be overcome and for the first observation of neutron decay to be made by Snell and Miller in 1948. They observed the disappearance of a fraction of a neutron beam from a reactor pile at Oak Ridge National Laboratory (ORNL) [26]. This was soon followed by the discovery in 1950, by multiple groups [27–30], that neutrons decayed into protons and a continuous spectrum of electrons. The half-life of the free neutron was measured to be on the order of 10 minutes [31].

All seemed well until Lee and Yang postulated that perhaps the symmetry of parity might not be conserved [32] in the weak interaction. If parity is a conserved symmetry, then flipping the three spatial dimensions of an interaction should produce an interaction that exists in nature. The symmetry also implies that chirality or handedness is preserved. For example, the right-hand-rule learned in introductory physics was determined arbitrarily for consistency's sake. A left-hand-rule works equally as well. If parity is not conserved than neither is chirality. If there is parity violation, the startling implication would be that the universe has a preferred handedness!

This strange idea was confirmed in 1957, when Wu et al. [33] discovered parity violation in the beta decay of spin polarized radioactive ^{60}Co. If the ^{60}Co atoms had a clockwise spin, the electrons from decay were preferentially emitted in one direction, if they were counter-clockwise, the electrons preferred the other direction. Later experiments [34] showed that the the helicity of the emitted electrons was in fact negative. It was then known that the weak interaction, which mediates beta decay, was purely left-handed and maximally violated parity. In 1960, this parity violation was measured in the free neutron [35].

1.3.1 Neutron Beta Decay Theory

In the SM of particle physics, represented by the gauge group U(1)x SU(2)x SU(3) plus gravity, there are four, distinct fundamental interactions at energies below about 100 GeV: the strong interaction, the weak interaction, electromagnetism, and gravity. The neutron is stable under all but the weak interaction. The weak interaction violates quark flavor conservation and can convert a down quark to an up quark by emitting a virtual W^- gauge boson, the carrier of the weak force. Because of the small mass difference between a neutron and proton, the W^- boson itself can only decay into one lepton generation: an electron and an electron anti-neutrino (see Figure 1.2).

In principle, any quantum field theory in the Dirac representation is composed of a
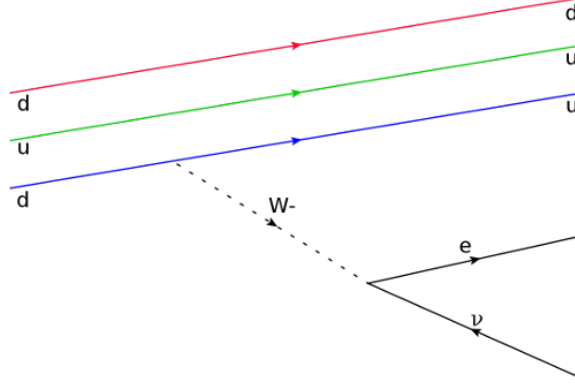
Figure 1.2: Feynman diagram for neutron decay. One of the down quarks is converted to an up quark emitting a virtual W^- boson that then decays into an electron and its anti-neutrino.

combination of the five Dirac bilinear components: scalar (S), pseudo-scalar (P), vector (V), axial vector (A), and tensor (T). In the case of the weak interaction, parity has so far proven to be maximally violated. This necessitates that the weak interaction only contain a mixture of vectors and axial vectors in a linear combination. Thus a parity violating theory of the weak interaction must be a vector minus axial vector (V–A) theory.

The emitted electron and anti-neutrino can either be emitted with their spin vectors anti-parallel, a Fermi (F) transition, or in parallel, a Gamow-Teller (GT) transition. A F transition preserves total angular momentum and isospin and consequently it preserves parity. A GT transition can change the total angular momentum and isospin by 0 or 1 but with a transition of $0 \rightarrow 0$ forbidden. F transitions arise from either S or V interaction, while GT transition arise from either A or T interactions. P interactions are negligible in allowed transitions and are generally ignored. Under V–A theory, the weak interaction is therefore a mix of F and GT transitions with V and A components respectively.

The neutron decay rate (Γ_n) or lifetime (τ_n^{-1}) can then be expressed using Fermi's golden rule

$$\Gamma = \tau^{-1} = \frac{2\pi}{\hbar} |\mathcal{M}|^2 \rho, \tag{1.1}$$

where $\mathcal{M}$ is the matrix element of the interaction, ρ is the density of final states, and $\hbar$ is the reduced Planck's constant. Presuming V–A theory, unpolarized neutrons, and low momentum transfer, it can be shown [2] that for neutron beta decay

$$\Gamma_n = \tau_n^{-1} = \frac{m_e{}^5 c^4}{2\pi^3 \hbar^7} |\mathcal{M}|^2 f, \tag{1.2}$$

where m_e is the mass of the electron, c is the speed of light, and

$$f = \int_0^{E_0} F(E_e) p_e E_e (E_0 - E_e)^2 dE_e \tag{1.3}$$

is the phase space factor where E_e is the electron energy, p_e is the electron momentum, E_0 is equal to the electron endpoint energy, and $F(E_e)$ is the Fermi function for neutron decay, which corrects for Coulomb attraction between the final state electron and proton.

The matrix element, $\mathcal{M}$, is defined as

$$\mathcal{M} = i\bar{\psi}_p \gamma_\mu (g_V + g_A \gamma_5) \psi_n g_{\mu v} \bar{\psi}_e \gamma^\mu (1 - \gamma_5) \psi_\nu, \tag{1.4}$$

where $\psi_{p,n,e,\nu}$ are the fermion fields for the proton, neutron, electron, and anti-neutrino respectively. The weak coupling constants, g_A and g_V, are defined as $g_V \equiv V_{ud} G_F$ and $g_A \equiv \lambda V_{ud} G_F$ where $G_F/(\hbar c)^3 = 1.166364(5) \times 10^5$ GeV^{-2} [36] is the Fermi coupling constant, which is calculated from muon decay and V_{ud} is a component of the Cabibbo-Kobayash-Maskawa (CKM) matrix, which will be covered later. The λ factor originates from g_A's dependence on the hadronic current and it is defined as $\lambda \equiv g_A/g_V$ and measured to be -1.2701 $\pm$ 0.0025 [20]. If time-reversal violation exists in weak decay, then a relative phase is included: $\lambda \rightarrow |\lambda| e^{i\phi}$.

After evaluation of the matrix elements and letting $K \equiv \frac{2\pi^3 \hbar^7}{m_e^5 c^4}$, it can be shown that Equation (1.2) will become

$$\tau_n^{-1} = \frac{1}{K}(g_V^2 + 3g_A^2)f = \frac{1}{K V_{ud}^2 G_F^2}(1 + 3\lambda^2)f. \tag{1.5}$$

If radiative corrections are included (see Section 1.4) there are two corrections to Equation (1.5) that can be applied: a nucleus dependent radiative correction modifying $f \rightarrow f(1 + \delta_r) =$ and $g_V^2 \rightarrow g_V^2(1 + \Delta_R^V)$ [2]. These corrections result in a shift of the lifetime by +3.886%$\pm$0.039% [37, 38].

The Cabibbo-Kobayash-Maskawa (CKM) matrix or quark mixing matrix is the 3×3 parametrization of weak interaction's flavor changing strength. It represents the difference between the weak eigenstates of the quarks and the mass eignenstates of the quarks. If the two were identical, then the matrix would be all 1's on the diagonal and flavor-changing between generations in the weak interaction would not exist. If there are only three generations of quarks and only SM physics is present, the matrix should be unitary. Current experimental measurements are consistent with this. Presuming unitarity, the matrix can be further reduced to four free parameters typically defined by three mixing angles and a

complex phase. From the Particle Data Group (PDG) [20], the CKM matrix is

$$
\begin{pmatrix} V_{ud} & V_{us} & V_{ub} \\ V_{cd} & V_{cs} & V_{cb} \\ V_{td} & V_{ts} & V_{tb} \end{pmatrix} = \begin{pmatrix} 0.97427 \pm 0.00015 & 0.22534 \pm 0.00065 & 0.00351^{+0.00015}_{-0.00014} \\ 0.22520 \pm 0.00065 & 0.97344 \pm 0.00016 & 0.0412^{+0.0011}_{-0.0005} \\ 0.00867^{+0.00029}_{-0.00031} & 0.0404^{+0.0011}_{-0.0005} & 0.999146^{+0.000021}_{-0.000046} \end{pmatrix}.
$$
(1.6)

Currently the best value of V_{ud} comes from measurements of super-allowed beta decays, but it can also be determined from the neutron lifetime by evaluating Equation (1.5), which results in [20]

$$
V_{ud} = \sqrt{\frac{4908.7(1.9)s}{\tau_n(1 + 3|\lambda|^2)}} = 0.9774 \pm 0.0014.
$$
(1.7)

This number is 2.5σ from the measurements of V_{ud} in super-allowed decays. However there have recently been large discrepancies in both measurements of λ and τ_n^{-1}. For example, the neutron lifetime experiments using cold neutron beams differ from those that use ultra cold neutrons (UCNs) trapped in bottles by 3.8σ [39]. As such, there are many future experiments that plan to measure both to high accuracy. It is worth noting that the RDK II's solenoid magnet will next be used for a future cold neutron beam lifetime measurement, which could shed light on this discrepancy (see Chapter 5).

1.3.2 Neutron Decay Correlations

A trio of scientists, Jackson, Treiman, and Wyld (JTW), in 1957 formulated a general form for the first order partial differential cross section for neutron decay [40, 41] using a parametrization from Lee and Yang [32]. In this general form, the nature of whether the weak force was vector, axial-vector, scalar, tensor, or a combination was left up to the strength of unknown coupling constants. These coupling constants correspond to the strengths of momentum and energy correlations in the decay products of neutron decay. The JTW equation for neutron beta decay can be written as

$$
\frac{\mathrm{d}\Gamma_n}{\mathrm{d}E_e \mathrm{d}\Omega_e \mathrm{d}\Omega_\nu} \propto |\mathbf{p}_e| E_e (E^0 - E_e)^2 \times
$$
$$
\left[1 + a\frac{\mathbf{p}_e \cdot \mathbf{p}_\nu}{E_e E_\nu} + b\frac{m_e}{E_e} + \frac{\mathbf{J}_n}{|\mathbf{J}_n|} \cdot \left(A\frac{\mathbf{p}_e}{E_e} + B\frac{\mathbf{p}_\nu}{E_\nu} + D\frac{\mathbf{p}_e \times \mathbf{p}_\nu}{E_e E_\nu}\right)\right],
$$
(1.8)

where $\mathbf{p}$ and E are the momenta and energies of the decay particles, E^0 is the electron endpoint energy, and $\mathbf{J}_n/|\mathbf{J}_n|$ is the neutron polarization. This leaves a, b, A, B, and D as constants to be measured by experiment. These constants can be shown, to first order to

Constant	Name	First Order Expression	Experimental Value
a	Electron-antineutrino correlation	$\frac{1-|\lambda|^2}{1+3|\lambda|^2}$	-0.103 $\pm$ 0.004
b	Fierz interference	0	
A	Spin-electron asymmetry	$-2\frac{|\lambda|^2+|\lambda|\cos\phi}{1+3|\lambda|^2}$	-0.1176 $\pm$ 0.0011
B	Spin-antineutrino asymmetry	$2\frac{|\lambda|^2-|\lambda|\cos\phi}{1+3|\lambda|^2}$	0.9807 $\pm$ 0.0030
D	Triple correlation	$2\frac{|\lambda|\sin\phi}{1+3|\lambda|^2}$	(-1.2 $\pm$ 2.0) $\times$ 10^{-4}

Table 1.1: JTW neutron decay correlation coefficients. λ is the coefficient representing the ratio of GT decays to F decays, ϕ is the relative phase if time reversal violation exists. Experimental values are from the PDG compilation [20].

have simple expressions relating them to λ and ϕ (see Table 1.1).

1.4 Radiative Corrections

Dirac [42], Fermi [43], and many others formulated a relativistic quantum theory of radiation in the 1920's and 1930's [4]. The theory, however, was not without its issues. Infinities present in its predictions were confusing and nonsensical [44–46]. One example of such an infinity was labeled the "infrared catastrophe" [47] by some. It was predicted that photons should be emitted from charged particles in decays, such as the electron and proton from neutron decay. The "catastrophe" was that the probability of emission increased without limit as one approached lower and lower energies due to the zero mass of the photon. In 1937, Bloch and Nordsieck [47] showed that this sort of infinity could be dealt with by considering a detectable cutoff energy for the radiation. It is now understood that radiative emission diagrams cancel with corresponding radiative loop diagrams at all orders.

By 1949, Tomonago, Schwinger, Feynman, Dyson and others had solved some of the other "problems of infinities" through renormalization [4]. The theory that emerged, QED, has been described as "the most stringently tested and the most dramatically successful of all physical theories" [3]. For example, standard model theory and measurements of the electron magnetic moment agree to ten digits that the fine structure constant, the coupling constant of electromagnetism, is 137.0359990 [48].

Meanwhile, the first measurements of radiative photons from nuclear beta decays were observed by Aston in 1927 [49]. Nuclei are simply put, complicated. Electron capture, nuclear excited states, and atomic structure can all affect the probability of radiative photon emission. This also accounts for the wide variety of half-lives and energy spectra seen in other isotopes that undergo beta decay. The radiative decay mode of the free neutron, on
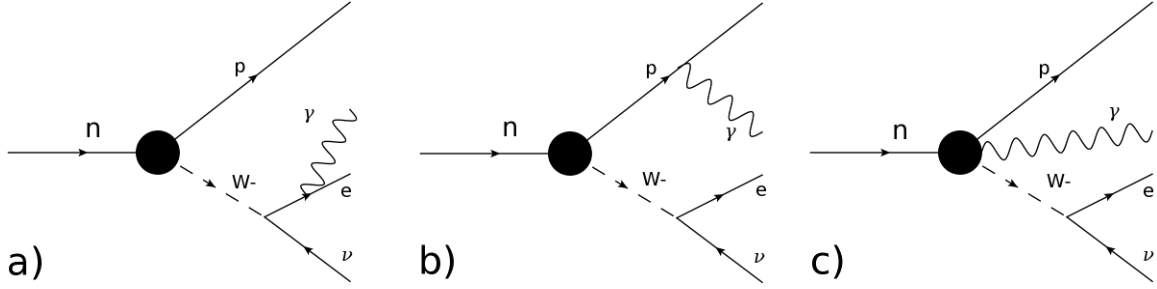
Figure 1.3: Feynman diagrams of the three primary contributors, in order, to radiative decay. a) electron inner bremsstrahlung (IB) b) proton inner bremsstrahlung (IB) c) weak-vertex inner bremsstrahlung (IB)

the other hand is free many of these complications or the corrections are calculable. While theoretically simpler, experimental difficulty remained in the neutron's long lifetime, the neutron's low energy daughters, and the neutron's reactor or accelerator produced origins.

1.4.1 Radiative Decay

Radiative photons emitted from the decay of the neutron are said to be from inner bremsstrahlung (IB). Bremsstrahlung is electromagnetic radiation produced by deceleration of charged particles in matter and similarly, IB can be thought of as originating from the sudden acceleration of the charged decay products in the neutron's decay. However, this classical picture is insufficient for a detailed understanding and quantum field theory must be used.

To proceed with a calculation of the partial decay rate in a field theory, it is first important to define what final state particles are detected. In the case of a neutron decay experiment that is sensitive to photons, it is important to define what the experiment's detectable energy range is and how many photons it can detect. For now, it will be assumed that multiple photons do not contribute significantly to the calculation of the partial decay rate.

For a single photon emission, three diagrams at order α will be considered (see Figure 1.3). The diagrams represent electron IB, proton IB, and weak-vertex IB. Electron IB dominates radiative decay while weak-vertex IB has been shown by heavy chiral perturbation theory to contribute less than 1% radiative decay [7, 50].

Taking the first two diagrams from Figure 1.3, a matrix element can be formed [9, 51]

$$
\begin{aligned}
\mathcal{M} =& e\frac{G_F}{\sqrt{2}}V_{ud}\left[\bar{\psi}_p\gamma^\mu(1+\lambda\gamma^5)\psi_n\right]\frac{1}{2\mathbf{q}\cdot\mathbf{p}_e}\left[\bar{\psi}_e\left((2\epsilon^*\cdot\mathbf{p}_e+\not{\epsilon}^*\not{q})\gamma_\mu\left(1-\gamma^5\right)\psi_\nu\right]\right. \\
&-e\frac{G_F}{\sqrt{2}}V_{ud}\frac{1}{2\mathbf{q}\cdot\mathbf{p}_p}\left[\bar{\psi}_p\left((2\epsilon^*\cdot\mathbf{p}_p+\not{\epsilon}^*\not{q}\right)\gamma_\mu\left(1-\gamma^5\right)\psi_n\right]\left[\bar{\psi}_e\gamma^\mu\left(1+\lambda\gamma^5\right)\psi_\nu\right],
\end{aligned}
\tag{1.9}
$$

where ϵ and $\mathbf{q}$ are the polarization vector and four momentum for the photon. Using this matrix element, it can be shown that the differential decay rate is [9]

$$
\begin{aligned}
\frac{\mathrm{d}\Gamma_n}{\mathrm{d}E_e\mathrm{d}\omega\mathrm{d}\Omega_\nu\mathrm{d}\Omega_\gamma} =& -\alpha F(E_e)\frac{g_V{}^2|\mathbf{p}_e|E_\nu\omega}{(2\pi)^7}\left(1+3|\lambda|^2\right)\times \\
&\left[E_\nu\left(\frac{1}{\omega}+\frac{E_e}{\omega^2}+\frac{m_e{}^2\left(E_e+\omega\right)}{(\mathbf{p}_e\cdot\mathbf{k})^2}-\frac{2E_e+\omega}{\mathbf{p}_e\cdot\mathbf{k}}-\frac{2E_e{}^2}{\omega\left(\mathbf{p}_e\cdot\mathbf{k}\right)}\right)\right. \\
&\left.+a\mathbf{p}_\nu\cdot\left(\frac{\mathbf{p}_e}{\omega^2}+\frac{m_e{}^2\left(\mathbf{p}_e+\mathbf{k}\right)}{(\mathbf{p}_e\cdot\mathbf{k})^2}-\frac{\mathbf{p}_e+\mathbf{k}}{\mathbf{p}_e\cdot\mathbf{k}}-\frac{E_e\left(2\mathbf{p}_e+\mathbf{k}\right)}{\omega\left(\mathbf{p}_e\cdot\mathbf{k}\right)}\right)\right],
\end{aligned}
\tag{1.10}
$$

where w and $\mathbf{k}$ are the energy and three momentum of the photon.

This differential decay rate was incorporated into a computer simulation described in Chapter 3, though in a slightly different form (see Appendix A). Using this event generator as a numerical integrator it is possible to determine the branching ratio of radiative decay within a specified photon energy range (see Figure 1.4). This determination is in agreement with other calculations of the radiative branching ratio [7, 8, 50, 51].
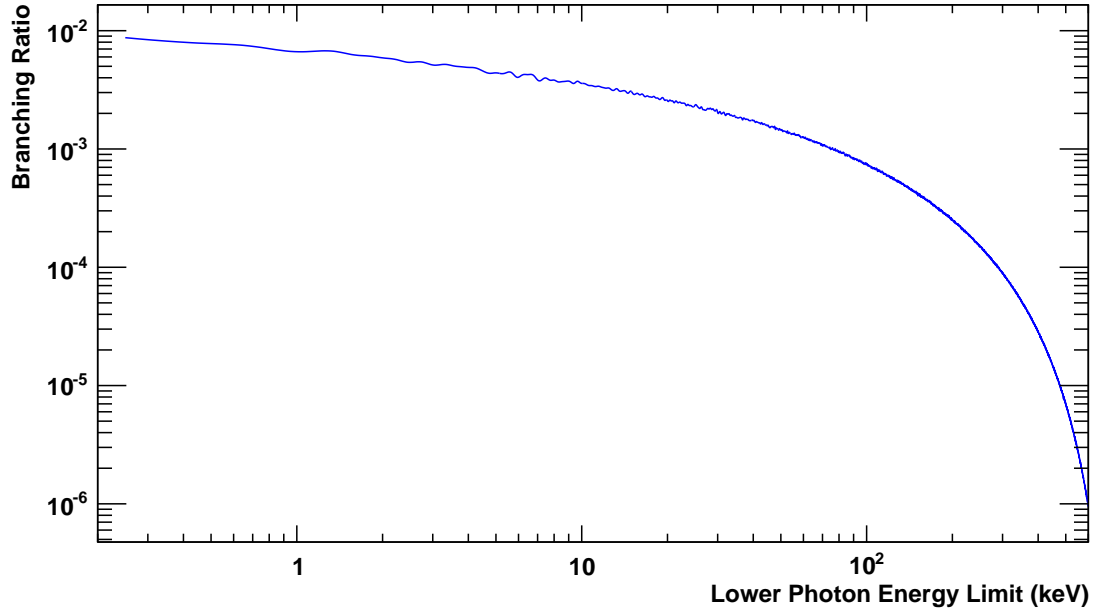
Figure 1.4: Plot of the radiative branching ratio determined from event generator. The x-axis represents the lower energy cutoff with the high energy cutoff fixed to the endpoint energy.
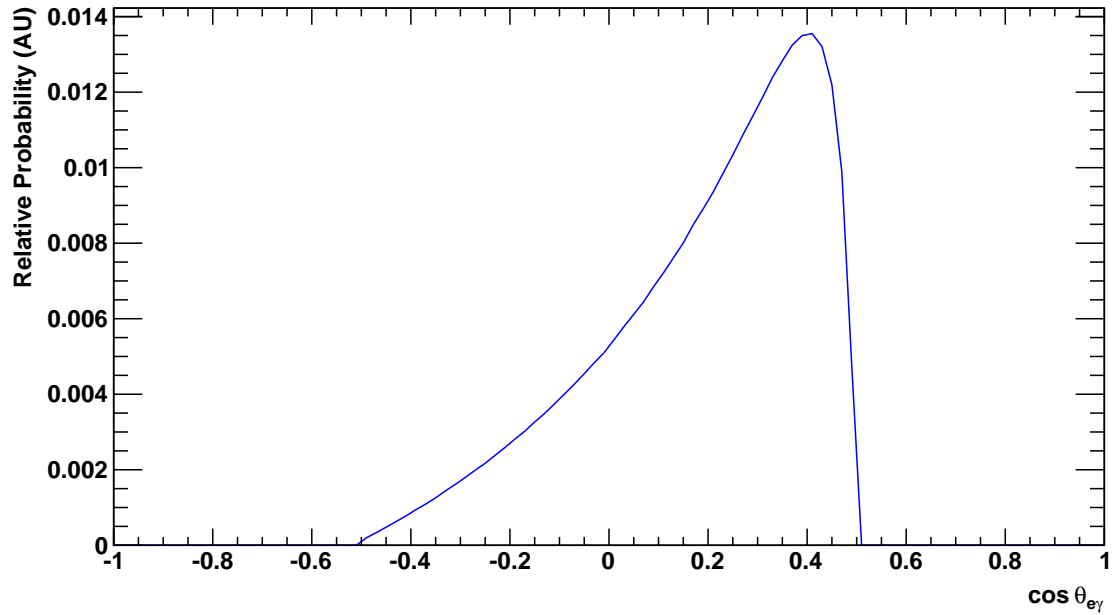
Figure 1.5: Plot of the electron-photon angular correlation in radiative neutron decay. The x axis represents the $\cos \theta$ angle between the two particles's momenta while the y-axis represents the relative probability. Due to the dominance of electron IB, the particles are correlated.

1.5 Radiative Neutron Decay Experiments

In 2002, the first limit on the branching ratio of radiative free neutron decay was made by Beck et al. [52]. They pioneered a method of triple coincidence that measured the photon in coincidence with the electron and proton to subtract background sources of radiation. Beck et al. used the cold neutron beam at the Institut Laue-Langevin (ILL) to illuminate an experimental apparatus, which consisted of a microchannel-plate (MCP) to detect protons, a plastic scintillator to detect electrons, and six CsI(Tl) scintillators coupled to photomultiplier tubes (PMTs) to serve as photon detectors. The six photon detectors surrounded the electron detector on one side of the neutron beam while the proton detector was on the opposite side. This took advantage of the angular correlations present between the three decay particles. Ultimately, the experiment was unable to overcome the photon backgrounds present and they measured a limit of $<6.9\times 10^{-3}$ (90% C.L.) for the branching ratio for photon energies of 35 to 100 keV.

Then in 2006, using the method of triple coincidence, the RDK I collaboration reported a radiative branching ratio for the neutron of $(3.09 \pm 0.32)\times 10^{-3}$ for the energy range of 15 to 340 keV [5,6] while leading order QED theory calculations predicted 2.85×10^{-3}. In the experiment, a cold neutron beam at NIST passed through a strong magnetic field that guided electrons and protons from neutron decay off-axis to a surface barrier detector (SBD) that measured them. An electrostatic mirror reflected protons traveling in wrong direction and had a voltage that could be varied. A single bismuth germanium oxide (BGO) scintillator coupled to an avalanche photodiode (APD) was directly exposed to the beam in the decay region. As the charged particle detector was located off-axis, external electron-induced bremsstrahlung was reduced. The RDK I experiment extracted the radiative branching ratio by forming a ratio of electron, proton, and photon/gamma coincidence (epγ) with electron and proton coincidence (ep) and then compared it with Monte Carlo (MC) simulations of the apparatus at various electrostatic mirror voltages.

In the context of the topic of this dissertation, the RDK II experiment improved upon RDK I in many ways. First, RDK II detected a significantly greater number of radiative decays than RDK I. This is primarily due to the addition of eleven additional BGO photon detectors to RDK I's single detector. RDK II also modified the collimation of the neutron beam, which allowed for a factor of two improvement in the neutron rate through the apparatus.

Another improvement that RDK II made was in the photon energy range measured. RDK I measured an energy range from 15 keV to 340 keV with a BGO scintillator coupled to an APD detector while RDK II measured an energy range from approximately 14 keV

to 781 keV (the neutron's endpoint energy) with its own BGO detectors. Additionally, a secondary set of large-area avalanche photodiode (LAAPD) detectors measured photons directly in the range from approximately 300 eV to 20 keV.

Finally, there were significant improvements to the analysis and simulation. This included greater understanding in areas such as pulse shape analysis, electron backscattering, magnetic reflections, and scintillator light response. The non-proportionality of BGO scintillator light response in particular produced a significant change to the actual energy range measured by these experiments, and an estimate of a correction to the RDK I measurement is found in Section 2.5.1.2.

CHAPTER 2

Experimental Apparatus

In this chapter, an overview of the RDK II experimental apparatus is covered followed by a detailed description of the components of the experiment.

2.1 Experimental Overview

The RDK II experiment operated at the NG-6 fundamental physics end-station [53] at the Center for Neutron Research (NCNR) at the NIST in Gaithersburg from December 2008 to November 2009. The reactor-produced cold neutron beam (see Section 2.2) was guided to the experiment using ^{58}Ni coated guides and was collimated with a series of ^{6}LiF apertures backed with lead. A calibrated ^{6}Li-foil neutron flux monitor [39, 54] was mounted downstream of the detection region (see Figure 2.1).

The detection of the neutron's decay products in coincidence was critical to the RDK II experiment and was pioneered by the ILL experiment [52] (see Section 1.5). To the leading order of radiative decay (order α), four particles are emitted by the decay. The neutrino interacted minimally with the matter of the experimental apparatus and escaped
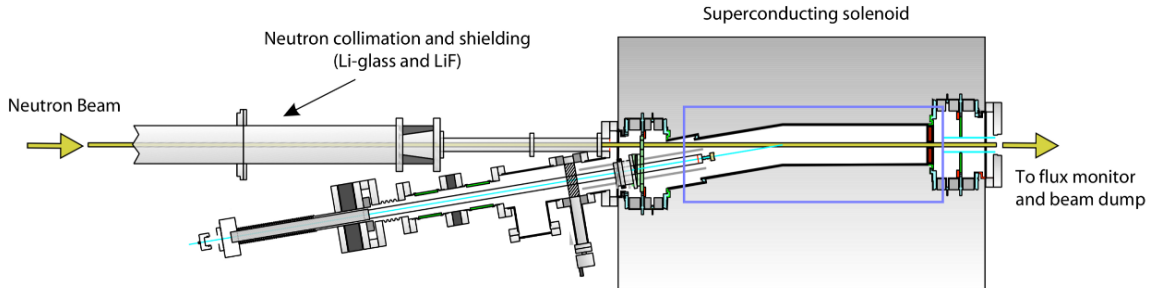
Figure 2.1: Diagram showing the relationship between the cryostat containing the solenoids and the detectors relative to the neutron beamline and flux monitor. The apparatus in the blue square is shown in more detail in Figure 2.2a
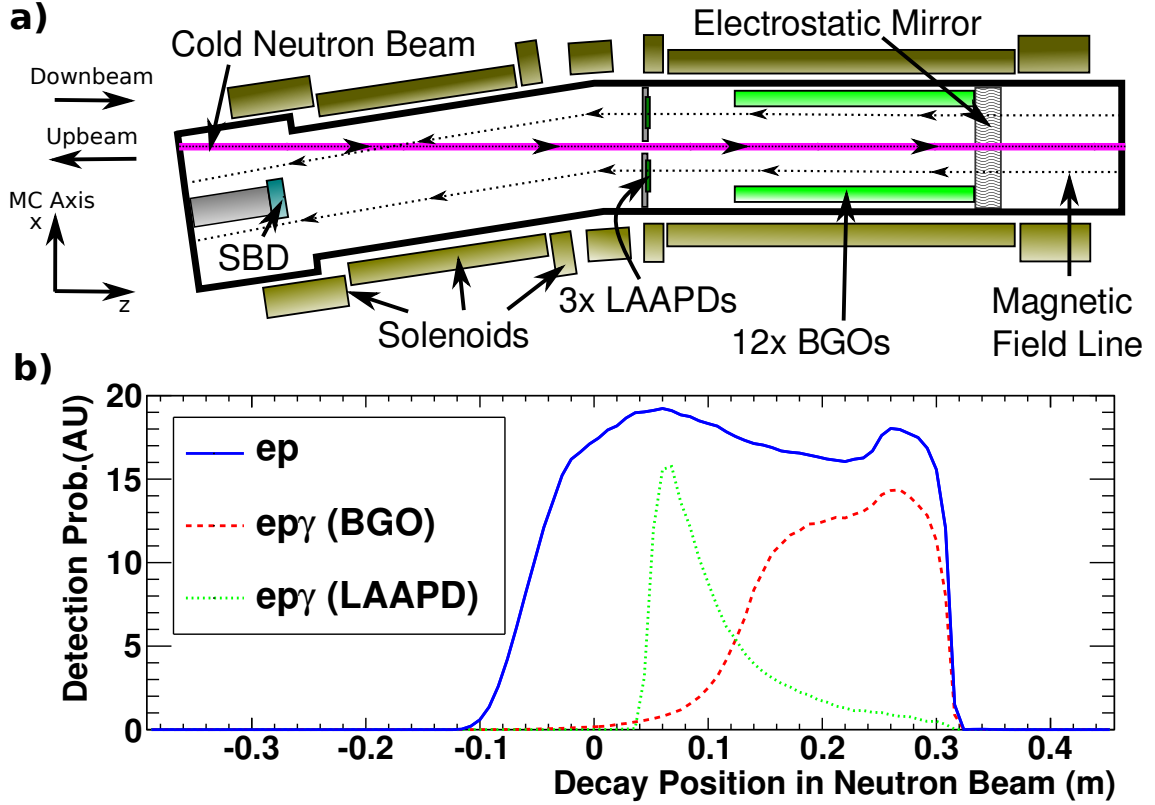
Figure 2.2: a) Cross-sectional diagram of RDK II's sensitive detection region. Objects are to approximate scale. View is from the top of the apparatus. b) Plot from the RDK II simulation that demonstrates the detection sensitivity along the neutron beam for various particle coincidences. Each coincidence type is scaled independently. Note that for this plot "0 m" represents the location of the center of the 9.5° bend in the magnetic field and is aligned with the diagram above. Acronyms in the figure: surface barrier detector (SBD), bismuth germanium oxide (BGO), large-area avalanche photodiode (LAAPD), electron and proton coincidence (ep), and electron, proton, and photon/gamma coincidence (epγ).

undetected. The other particles, the electron, the proton, and the radiative photon, were detectable.

The active region was defined by a strong magnetic field (3.3 to 4.6 T) created by a set of superconducting solenoids (see Section 2.3). A ring of aluminum charged to 1400 V served as an electrostatic mirror. The mirror created an ≈800 V barrier to protons and defined the downstream end of the active detection region. Approximately 34 cm upstream of the mirror, the magnetic field bent at a 9.5° angle, which defined the upstream end of the detection region (see Figure 2.2a).

If a neutron decayed between these two points, the charged decay products, an electron and a proton, followed adiabatic helical orbits around the field. If the electron was emitted

in the direction of the beam, or downstream, its energy, on the order of hundreds of keV, was usually sufficient to escape the detection region and the electron remained undetected. If the electron was instead emitted in the opposite direction, upstream, it followed the magnetic field to a surface barrier detector (SBD) in a time on the order of nanoseconds. The proton, with an energy less than 750 eV, was detected if it was emitted in either direction as the electrostatic mirror was sufficient to reflect it. The proton traveled to the SBD in a time on the order of microseconds (see Section 2.4).

Two separate photon detector arrays surrounded the neutron beam in the active region [55]. The higher energy photon detector array consisted of twelve bismuth germanium oxide (BGO) scintillator crystals coupled to avalanche photodiodes (APDs) (see Section 2.5). The secondary photon detector array consisted of three large-area avalanche photodiodes (LAAPDs) that directly measured low energy photons without a scintillator (see Section 2.6). The BGO detectors overall systematic and statistical uncertainty is expected to be on the order of 4%, while the LAAPD detectors uncertainty is expected to be on the order of 14%. The significantly greater uncertainty in measurements with the LAAPD detectors is a result of the uncertainty of its complex energy response at low energies (see Sections 2.6.1.

A data acquisition (DAQ) system [55, 56] was used to to record the waveform data from the particle detectors. In its non-diagnostic mode, the DAQ system utilized two single channel analyzers and a time-to-amplitude converter to trigger data recording. The signal of an ep was assumed to be detected when the SBD registered a voltage signal equivalent to ≈50 keV or more (an electron) followed by a voltage signal equivalent to ≈7 keV or more (an accelerated proton) within a timing window of 0.25 to 25 μs of the first peak, data was recorded to disk from both the SBD and both photon detector arrays. The recorded waveforms spanned 2048 channels: from ≈25 μs before the electron signal to ≈57 μs after (see Section 2.7).

The experiment detected in two modes of coincidence. An electron and proton coincidence (ep) occurred when the SBD detected an electron signal followed by a delayed proton signal. An electron, proton, and photon/gamma coincidence (epγ) coincidence occurred when the SBD detected an electron signal followed by a delayed proton signal while one of the photon detectors detects a photon/gamma signal simultaneously with the electron signal. RDK II experiments use the detection of the electron and proton to validate that the photon originated from neutron decay and not from a background photon. This is covered in greater detail in Chapter 4.

The two coincidence modes depended significantly on the decay position along the neutron beam (see Figure 2.2b). In addition, there are numerous correlations between

momenta and energies of neutron decay's daughter particles that must be accounted for. This necessitated a sophisticated MC simulation be used to interpret the experimental data (see Section 3).

2.2 Cold Neutron Beam

Fundamental neutron decay experiments require a large number of neutrons to decay within their experimental volume in order to produce statistically significant results. This is achieved by producing a beam of cold neutrons or by producing and storing ultra cold neutron (UCN). The source of neutrons used in RDK II originated from the NCNR located in Gaithersburg.

2.2.1 NCNR Cold Neutron Source

The source of neutrons used in RDK II originated from the NCNR located in Gaithersburg. The NCNR is a 20 MW reactor operating on highly enriched (93%) ^{235}U fuel [57]. Neutrons from fission have an average energy of approximately 20 MeV. These neutrons were then moderated by the deuterated or heavy water (D_2O) that surrounded the fuel rods. This reduced the average energy of the neutrons to the 30 meV range or "thermal neutron energies". Inside the reactor, there was a neutron cold source, which consisted of cooled D_2O surrounded by a liquid hydrogen (LH_2) volume. This further cooled the neutrons to a median energy of 2 meV or 6.4 Å.

2.2.2 NG-6 Neutron Beamline

These cold neutrons are transported out of the reactor and cold source via ^{58}Ni coated glass tubes, which terminate near the cold source. Cold neutrons strike the walls of these tubes and, through a spin-spin interaction, undergo total internal reflection as the ^{58}Ni coated tubes have an effective refractive index of less than one [58]. Much like a fiber optic cable, the neutron is transmitted through these evacuated guides away from the reactor and to various scientific experiments. The NCNR at the time of the RDK II experiment had eight operational cold neutron beamlines. RDK II occupied the NG-6 beamline [53] during its operation. A series of Li glass collimators and LiF scrapers collimated and defined the cold neutron beam and removed divergent or stray neutrons.

The beam enters the active detection region, which is held at a vacuum that is less than a 10^{-9} mbar. These pressure measurements were made near the ion pumps located relatively
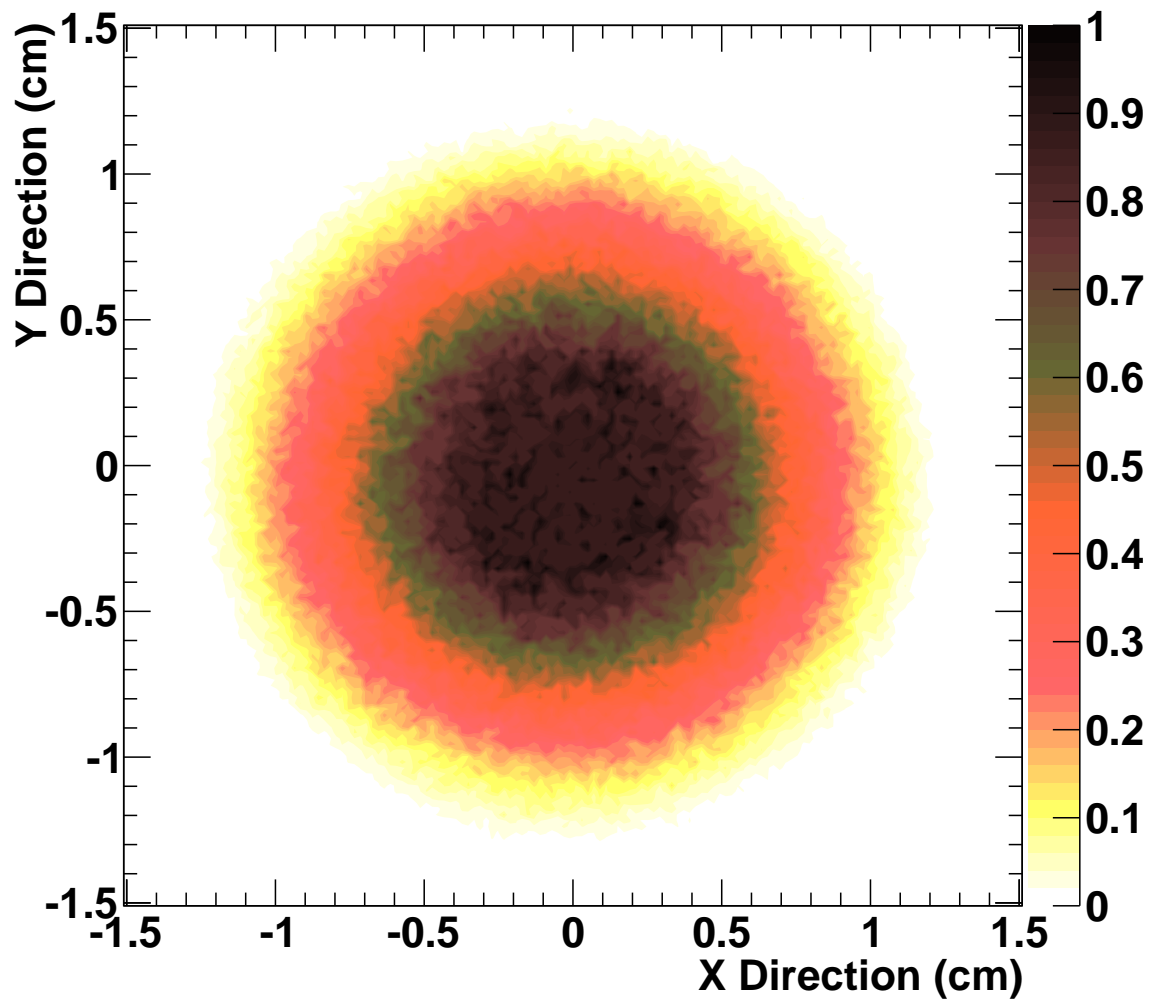
Figure 2.3: Profile of cold neutron beam taken downstream of the active detection region. A dysprosium foil was exposed and activated by the neutron beam. The beta decays from these activations were measured by exposing a photographic plate to the foil. A small piece of cadmium foil located in the center of the image was placed on the dysprosium foil to serve as a marker, which was digitally removed in this profile.

far from the neutron beam line. Due to the cryogenic environment of the experiment, it is actually expected that the vacuum was significantly better at the center where the neutron beam is located. Irrespective of whether the center was at lower pressure, there was minimal attenuation of the protons by any residual gas.

2.2.3 Neutron Beam Monitor

A ^{6}Li-foil neutron flux monitor [39, 54] was mounted downstream of the detection region. Incoming neutrons produce charged alphas and tritons through the ^{6}Li(n,t)^{4}He reaction. Four calibrated surface barrier detectors measured the charged particles produced. The flux monitor measured an average neutron capture flux of 1.07×10^8 neutrons per second, which was roughly twice that of RDK I. This was primarily due to reduced collimation of the beam.

2.3 Electric and Magnetic Fields

A set of superconducting solenoids made by Oxford Instruments [59] was used to generate the magnetic fields in the active detection region of the RDK II apparatus (see Figure 2.2a). The magnet consisted of 11 coils made from niobium-titanium filaments in a copper matrix. The coils ranged from 14 cm to 24 cm in diameter [59]. The coils were arranged such that there was a 9.5° bend that directed charged particles off the beam axis towards the SBD. The magnet was cooled with liquid helium and generated a maximum field of 4.6 T during operation. At this field strength, both electrons and protons from neutron decay followed cyclotron orbits around the field with a radius on the order of 0.1 mm (see Figure 2.4).

The magnet has been used in previous experiments including RDK I, an electron-antineutrino angular correlation experiment [60], and neutron lifetime experiments [54, 61]. The magnet will be used for an updated and improved neutron beam lifetime experiment that is currently underway.

Electric fields in the active detection region can affect the adiabatic motion of the charged particles. As a particle follows a magnetic field line, the component of its kinetic energy along that field line must overcome any sources of differential potential (see Section 3.5.1 for more details on adiabatic motion in magnetic fields). In the experiment, there were three sources of electric potential in the active detector region that could have potentially influenced charged particle motion: the electrostatic mirror, the SBD, and the LAAPDs' bias field (see Figure 2.6).

The electrostatic mirror was a simple aluminum ring 2 cm wide with a 4.76 cm diameter
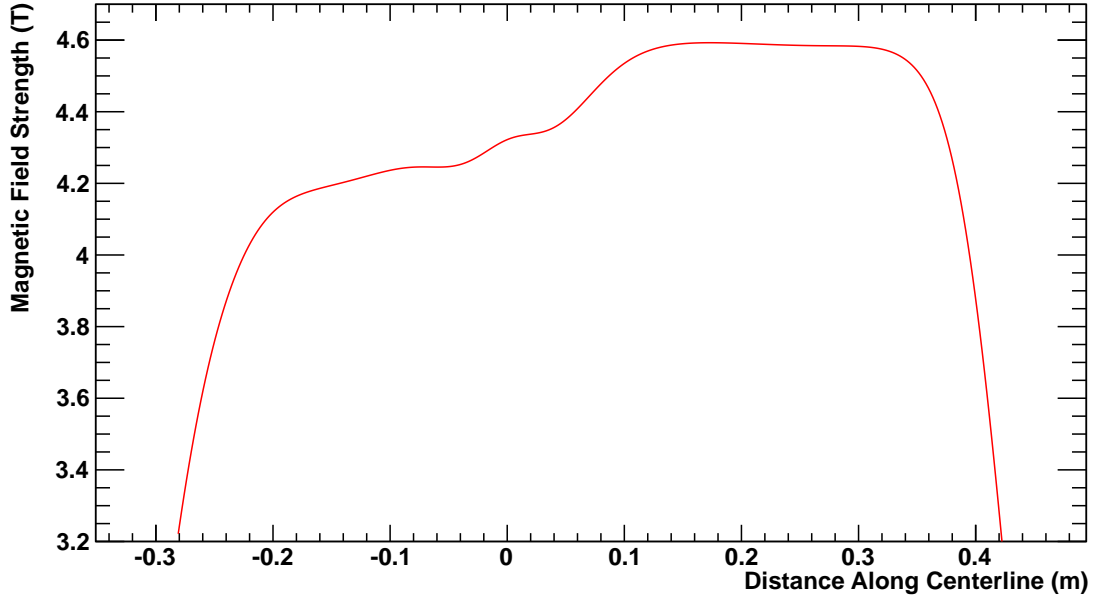
Figure 2.4: Plot of the simulated magnetic field strength from the RDK II solenoids along the central magnetic field line (see Chapter 3.
)

and was located 33.7 cm downstream of the center of the bend. It was charged to +1.4 kV relative to the bore and other grounded materials. At its center, it created an ≈880 V barrier to any charged particles.

The SBD was held at -25 kV relative to ground. When protons approached the SBD, the field generated served to accelerate them from the energy range of 100's of eV to 25 keV, which allowed the protons to penetrate the conductive gold layer on the front face of the SBD (see Section 2.4).

The LAAPDs were biased by approximately 1350 V. While the first version of the detector array shielded this potential from the active detection region, the second version was not completely shielded (see Section 2.6). This caused a small electrostatic potential of ≈5 V at the center of the beam, which potentially reflected protons. MC simulations indicated that this correction did not significantly affect the measurement.
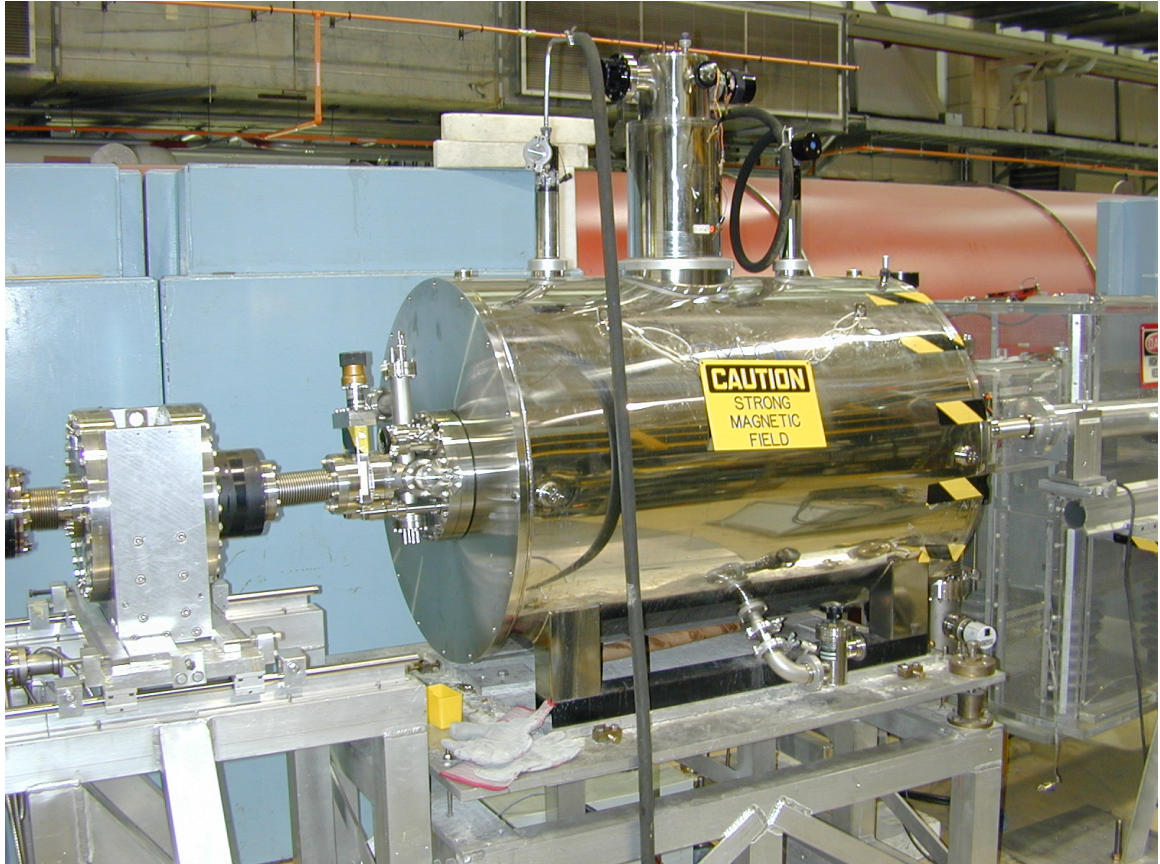
Figure 2.5: Photo of the cryostat which contains the RDK II solenoids and the active detection region. The high voltage isolation cage that supplies the -25 kV potential for the SBD field is visible on the right.
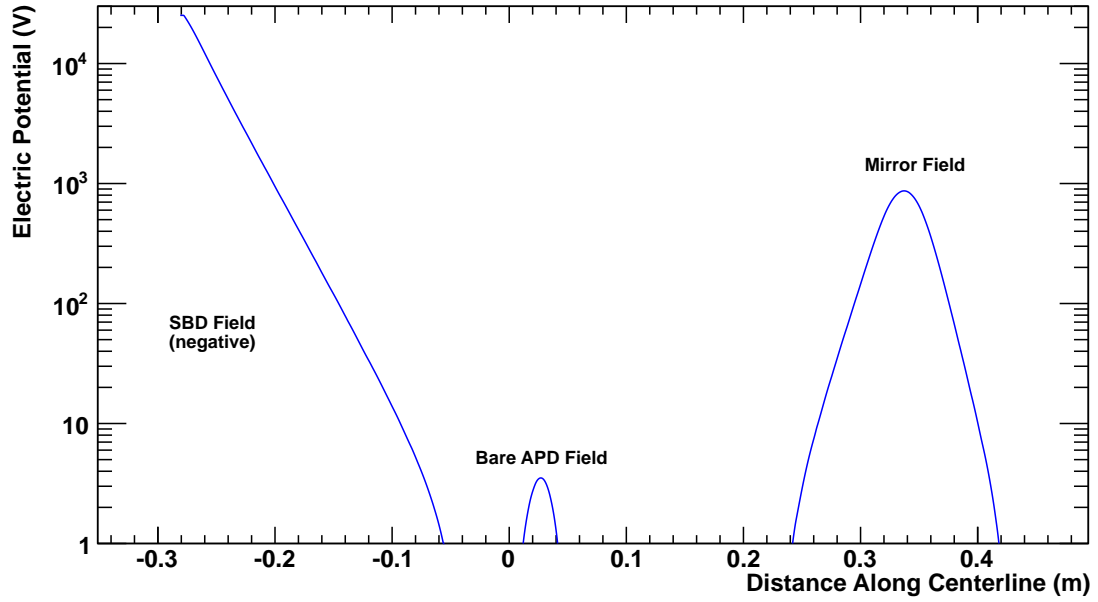
Figure 2.6: Plot of the simulated electric field potential from the electrostatic mirror, the leakage field from the LAAPD bias potential, and from the charged SBD. The SBD's potential was negative under operation and served to accelerate protons through the SBD's gold layer (see Section 3.3).

2.4   Surface Barrier Detector

A surface barrier detector (SBD) serves as the charged particle detector for both protons and electrons in the RDK II apparatus. A SBD is a semiconductor device made from a silicon crystal with doped impurity elements that are either pentavalent to create n-type material, or trivalent to create p-type material [62]. N-type materials have loosely bound electrons in the conduction band while P-type materials have loosely bound positive holes in the conduction band. In the case of a SBD, a P-N junction is formed and a reverse bias is applied. This creates a depletion region at front side of the detector. At liquid nitrogen temperatures, one electron-hole pair is created for every 3.76 eV of ionizing radiation that is absorbed in this region [62]. By biasing the device with an electric field, the holes travel in one direction with the electrons traveling in the other to create a signal. While a fraction of the signal will be lost to impurities in the silicon crystal, the large number of charge carriers created gives the SBD excellent energy resolution.

Both 1 mm and 1.5 mm thick silicon detectors were used in the experiment. They were made by ORTEC® [63] and had an active area of 600 mm^2. They consisted of a wafer of doped silicon coated with 20 nm of gold on the front face, which provides the positive electrical contact, and layer of aluminum, which serves as the contact, on the opposite,
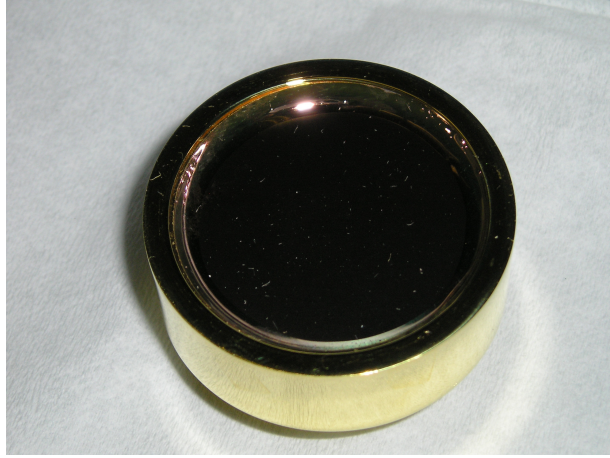
Figure 2.7: Photo of the front of a SBD. The gold coated front of the silicon faces the camera and the epoxy, which connects it to the outer canister, can be seen on the inner edge.

inner face. The wafer was contained within a brass canister which terminated in a microdot connector. During operation, the SBD was located off the beam axis 27.8 cm from the center of the bend. While the SBD as a whole was held at -25 kV, the detector itself was only biased by 100 V. It was radiatively cooled down to approximately 150 K.

2.4.1 SBD Energy Response

In order to convert the recorded pulse height to an energy incident on the SBD detector, both calibrations were performed offline, with the neutron beam off, and online, while the neutron beam was on. Offline, ^{241}Am and ^{57}Co were used as gamma sources while ^{133}Ba, ^{113}Sn, ^{207}Bi, and ^{36}Cl were used as electron sources. These sources, along with studies using a pulser system, identified a small quadratic correction to the proportionality of the detector, which was included in the analysis. The energy resolution of the SBD was determined to have a full width half maximum (FWHM) of 5.4 keV, which remained stable over its operational range.

While online, the electron endpoint energy from neutron decay, 781.6 keV, was monitored to account for gain drift in the SBD and amplification electronics. A functional form was fit to the endpoint of the detected electron spectrum, which presumed that all electrons that reached the SBD lost 25 keV of energy from the SBD's electric field. From this fit, the pulse height to energy conversion was determined. The functional form was tested against the simulated electron energy spectrum and was confirmed to correctly identify the electron endpoint energy.

2.5 BGO Photon Detectors

An array of twelve BGO scintillation crystals coupled to APDs served as the primary photon detectors for RDK II. Each crystal was 1.2 cm x 1.2 cm x 20 cm and their inner edges were located 3.6 cm from the center of the neutron beam. The upstream ends of the crystals were painted with a reflective paint and each crystal was wrapped in "two layers of aluminized Mylar ("total of 12.4 μm Mylar and 0.065 μm aluminum). An additional aluminized Mylar sheet (12.7 μm Mylar and 0.049 μm aluminum)" [55] The downstream ends coupled to the APDs. Because of the liquid nitrogen temperatures, optical grease was not used on this connection.

The pure inorganic scintillator crystal, $Bi_5Ge_3O_{12}$, also known as bismuth germanium oxide (BGO) or bismuth germanate, contains no added activator, unlike many other scintillators used in radiation detection [62]. It was chosen in part because its high density, 7.13 g/cm^3, makes it one of the best absorbers [62] of high energy photons. This allowed detection of photons with energy up to radiative decay's endpoint energy, 781 keV. In addition BGO's light yield at liquid nitrogen temperatures actually exceeds that of NaI(Tl) scintillators, a common alternative. BGO does suffer from having both a factor of two slower response time than NaI(Tl) and a higher index of refraction, which must be coupled carefully to the light detection device. This and other considerations are discussed in more detail in other references [9, 64].

Avalanche photodiodes (APDs) are semiconductor devices that use an internal gain created by strong electric fields that multiply the number of charge carriers that are collected. They have a higher quantum efficiency, lower power consumption, and are smaller than PMTs, and most importantly, unlike an PMTs, they can operate in a high magnetic field. An APD's band gap energy is between 1 to 2 eV making it similar in operation to a solar cell [62].

Incoming photons from neutron decay were absorbed in the high density BGOs crystal. This produced quantities of scintillation light at 520 nm [65] nominally proportional to the amount of energy absorbed. This scintillation light was then collected by the APDs, which produced a voltage signal proportional to the quantity of hole-pairs it detected.

2.5.1 BGO Energy Response

Calibrations on the BGO array were performed both off-beam and on-beam. Off-beam calibrations were performed with the magnetic field off and at liquid nitrogen temperatures. Radioactive sources, including ^{137}Cs, ^{133}Ba, ^{57}Co, and ^{241}Am, were attached to a rod and placed in the center of the detector array using a reentrant tube that allowed the magnet's
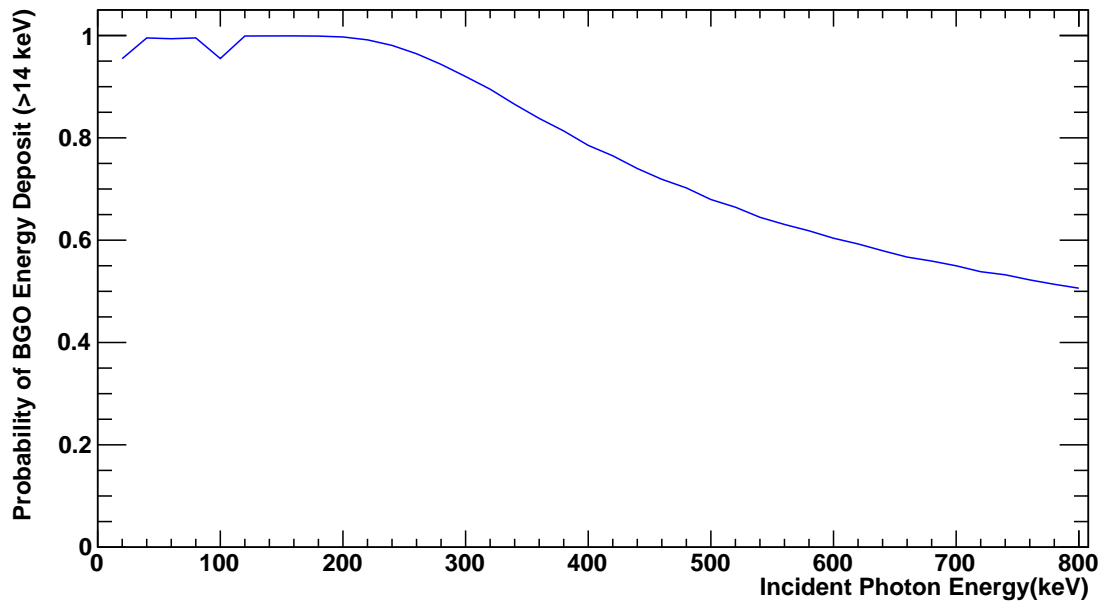
Figure 2.8: Plot of the RDK II BGO crystal's photon attenuation based on the incident photon energy. Data was generated from Geant4 simulations.
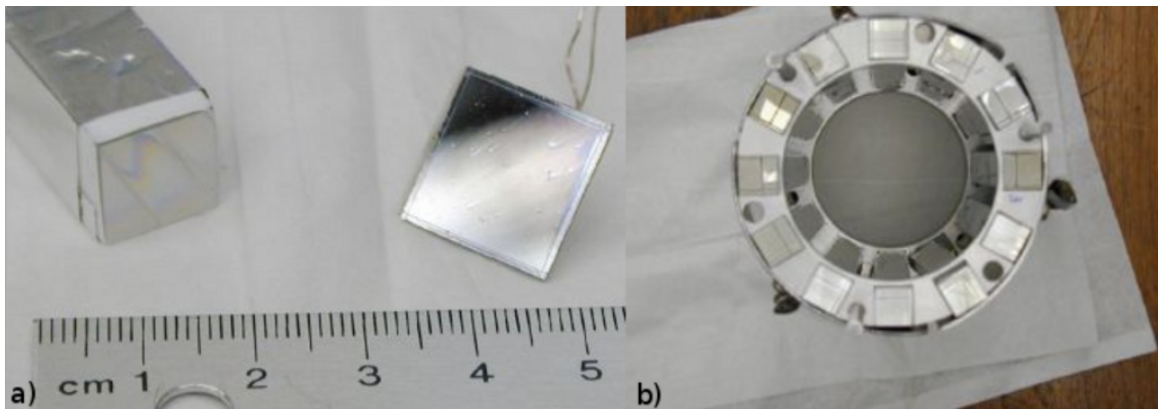
Figure 2.9: a) Photo of one end of a wrapped BGO crystal and its corresponding APD. b) The 12 element BGO crystal array.
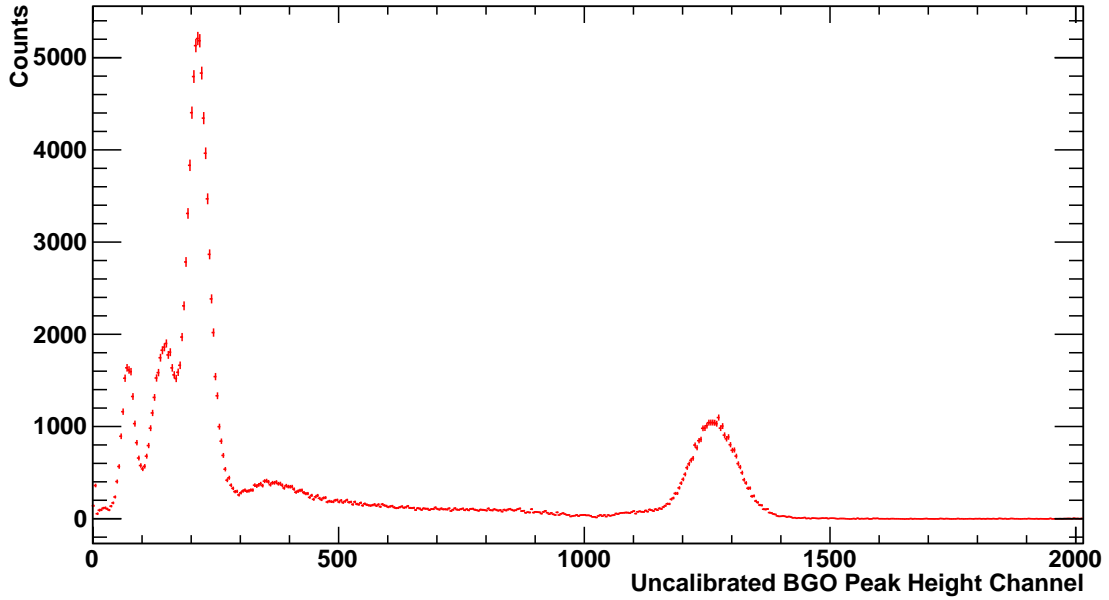
Figure 2.10: Plot of the response of a BGO detector to a combination of ^{57}Co and ^{137}Cs sources.

vacuum chamber to remain sealed. From these calibrations an energy resolution of the BGO detectors was measured and it was determined to follow a Poisson distribution that at 511 keV resulted in a FWHM of ≈60 keV.

On-beam calibrations utilized a 511 keV peak located in the background photon spectrum. This peak resulted from electron-positron annihilations occurring from a variety of sources associated with the reactor-produced neutron beam. This peak was monitored and the energy of recorded data was scaled appropriately. In addition, two more complex photon response phenomena were investigated: position dependent light collection and non-proportional energy response.

2.5.1.1 BGO Light Collection

One of the properties that influenced the energy response of the apparatus was the positional dependence of the BGO crystal's light collection. This positional dependent response originated from the manner in which the scintillation light was collected and reflected by the ends of the BGO crystal. This problem has been previously studied and is well understood [66]. Light collection was less efficient at the center of the crystal than at either end: either the end coupled to the APD or the end with reflective paint (see Figure 2.11). Given the same incident photon energy, the APD measured a greater number of scintillation photons from the BGO if the originating photon struck the ends of the crystal. This results

26

in a proportionally greater peak height detected by the electronics at the ends than when the originating photon struck the center of the crystal. To measure this phenomenon for RDK II BGO crystals, radioactive sources were collimated and then positioned to expose different regions of the crystal to the radiation. Measurements of the RDK II BGO crystals indicated that the relative effect of this light collection is independent of incident energy and of the particular crystal examined.

In addition to increasing the energy resolution of any sample measured, positional dependence must be accounted for when performing energy calibrations. During radioactive source calibration measurements, a physical source was placed in a position located in the center of the BGO array. Calibrations were made relative to the energy of ^{137}Cs, which has a strong peak located at 662 keV. During the on-beam operations of the RDK II experiment, the 511 keV electron annihilation peak was used as an energy calibration. The annihilations arose from neutron capture events on materials within the apparatus and are assumed to evenly fall on the BGO crystals. Because the ^{137}Cs source was centered on the BGO crystal, the calibration differed from the annihilation events due to the positional dependence. A multi-polynomial fit of positional dependence along the crystal's beam axis was included in the simulations used to study the experiment (see Figure 2.11). The absolute normalization of this was adjusted such that 511 keV photons simulated by the MC simulation code resulted in a peak centered at the calibrated peak height channel equal to 511 (see Section 3.7).

2.5.1.2   BGO Non-proportionality

Above and near 662 keV, the BGO scintillation response is reasonably linear, producing a proportional amount of scintillation photons for a given incident energy. As the incident photon energy is decreased, the light output is proportionally less than expected. The source of this non-proportionality is thought to be recombination of liberated electrons-hole pairs, but the process is not completely understood [67]. This phenomenon had been measured in BGO previously [68–72] and is present in other scintillator crystals. This non-proportionality in the light output of BGO forms one of the largest sources of systematic error for RDK II and its inclusion dramatically affects the radiative photon spectrum.

Studies of BGO have shown that the non-proportionality is independent of crystal dimensions and temperature [68, 69]. It is standard practice to use the 662 keV peak of ^{137}Cs as a baseline, by defining its relative light output to be "1.0". If a scintillator is completely proportional, the relative light output would be constant at "1.0" for all energies.

To characterize the non-proportionality of RDK II BGO crystals, both published values in BGO and measurements taken with radioactive sources on RDK II crystals were used.
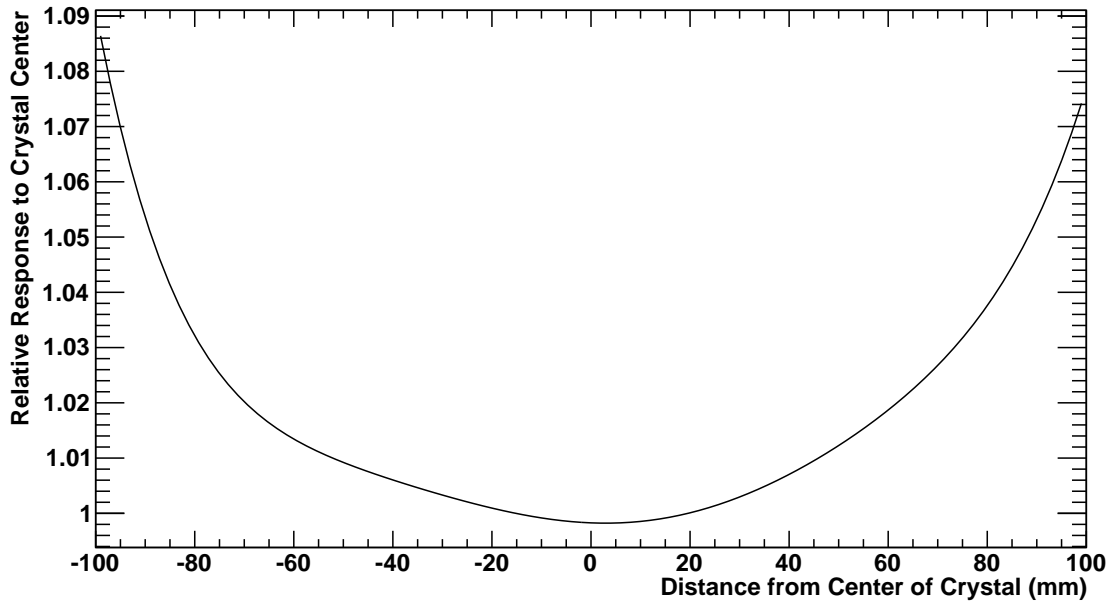
Figure 2.11: Plot of the average response of eleven BGO crystals relative to the center position as a function of the collimated source position.

The first study illuminated a single RDK II BGO crystal and APD in a small test cryostat with a variety of radioactive sources ([57]Co, [109]Cd, [133]Ba, ^{137}Cs, [153]Gd, [235]U, and [241]Am). The DAQ system for this study consisted solely of a preamplifier, shaping amplifier, and a multi-channel analyzer (MCA). The second study utilized the calibration measurements detailed in Section 2.5.1. This study included the complete DAQ system as described in Section 2.7.

Figures 2.12 and 2.13 include data from other publications as well as data points extracted from RDK II crystals. Clearly visible are large discontinuities at energies corresponding with the K and L electron edges of bismuth near 85 keV and 15 keV respectively. A parametrized model was used to fit the data and incorporated into the simulation. Energies lower than 10 keV were extrapolated to follow the trend present in data near 10 keV.

Due to this non-proportionality, it is difficult to define an experimentally detected energy scale without resorting to a complex deconvolution analysis. It was decided instead to define a detected peak height scale and reference peak height channel 511 to 511 keV. From the non-proportionality analysis this makes the peak height channel cutoff of 10 equivalent to approximately 14 keV.

In the original RDK I experiment, this non-proportionality was not known to the collaboration and was not accounted for. In the experiment, the energy range measured was

28
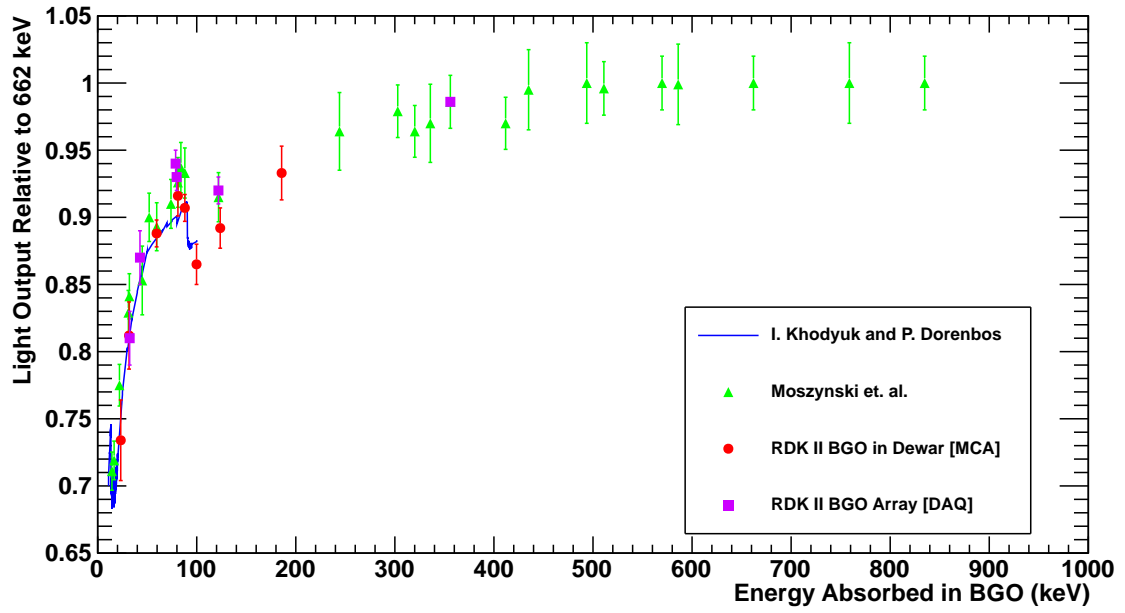
Figure 2.12: Plot of the experimentally measured [68, 69, 73] non-proportional response of BGO crystals in the energy range of 10-1000 keV.
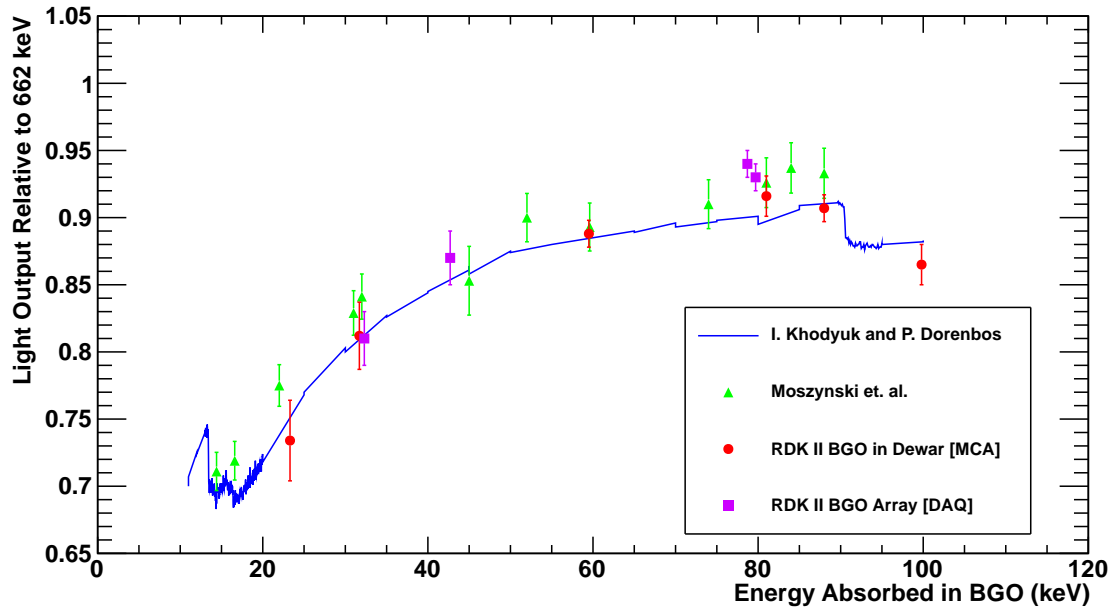
Figure 2.13: Plot of the experimentally measured [68, 69, 73] non-proportional response of BGO crystals in the energy range of 10-120 keV.

described as 15 keV to 340 keV. Knowing that this energy range was calibrated with an energy peak from an ^{241}Am source at 60 keV, we now know that the actual energy range measured was 19 keV to 308 keV, which changes the branching ratio predicted by theory from 2.85×10^{-3} to 2.52×10^{-3}.

2.6 LAAPD Photon Detectors

Partway through the experiment, a detector array capable of detecting photons in the energy range of 100 eV to 20 keV was installed. It utilized LAAPDs that were not coupled to a scintillator. Low energy photons from radiative decay interacted with the doped silicon in the LAAPD and were detected directly.

Two versions of the LAAPD apparatus were installed. The first version ran with the bias field of the APDs perpendicular to the magnetic field of the experiment (see Figure 2.14). The 4.6 T field combined with the low temperature at which the detector operated, lead to detrimental detector behavior. This behavior had not been seen before in an APD [74]. No usable data was recorded with this version of the apparatus.

The second version of the apparatus consisted of an array of three LAAPDs that had a bias field parallel to the magnetic field (see Figure 2.15). The LAAPDs have an active area of 2.8 cm by 2.8 cm by 60 μm. Their front faces face downstream and their centers are located at 3.5 cm radius from the beam. This second version operated successfully and was used for the remainder of the experiment.

2.6.1 LAAPD Energy Response

Calibrations of the LAAPD array were performed both offline and online. Offline calibrations first began with measurements of x-ray fluorescence using ^{55}Fe down to aluminum's k-shell line at 1.5 keV. However, it was not possible to extract a meaningful calibration below 900 eV. Following this attempt, data were taken utilizing two synchrotron light sources. The first of these measurements was taken at NIST at the Synchrotron Ultraviolet Radiation Facility (SURF) III facility on the BL3 beam line. Measurements were taken using the synchrotron's continuous spectrum modified by material filters made of aluminum and Mylar. The second of these measurements was made at BNL at the NSLS on the U3C beam line. The U3C beamline incorporated a monochromator that produced monochromatic energies at six energies between 350 eV and 1500 eV (see Figure 2.16). These measurements are detailed in a separate paper [75]. On-beam calibrations utilized an ^{55}Fe source, which was positioned off of the beam axis. The $\approx$5.9 keV line from the source was background
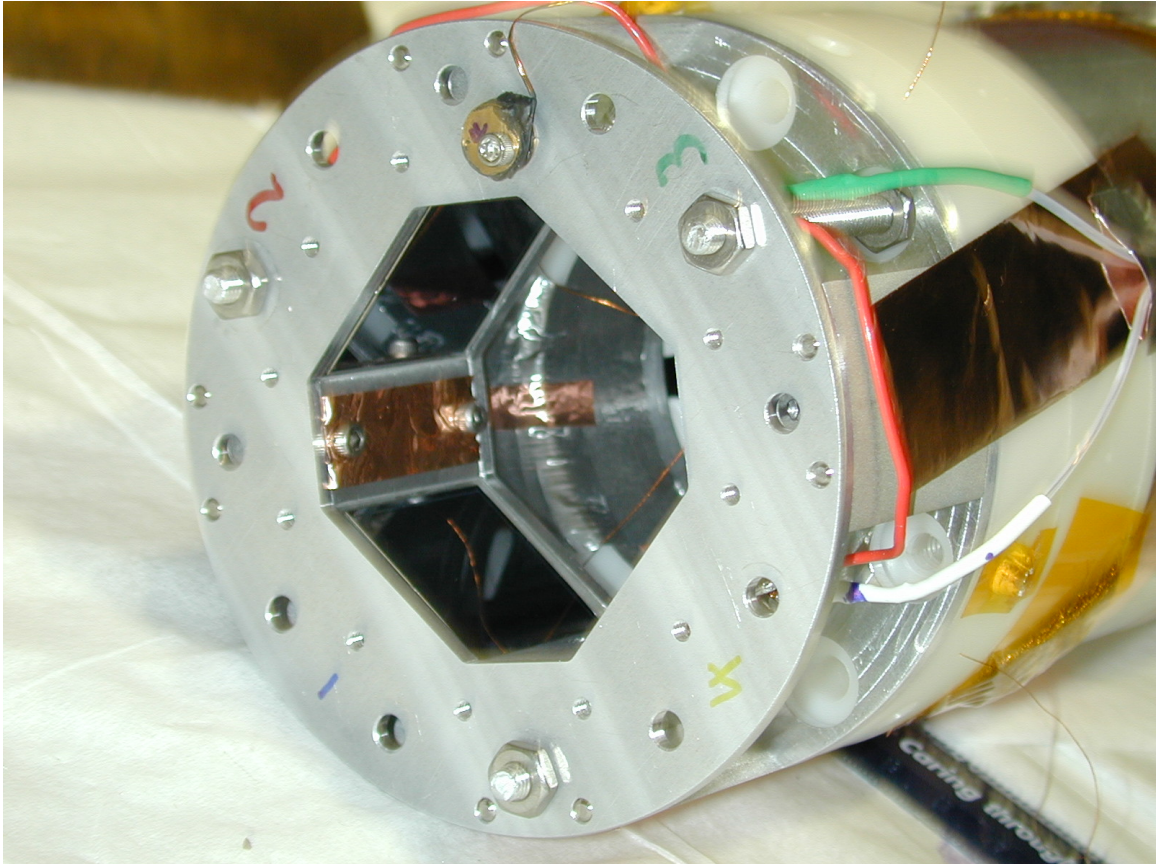
Figure 2.14: Photo of version 1 of the LAAPD detector array, which was present during approximately one third of RDK II's operation but did not take useable data. Two of the four LAAPDs are visible in this photo.

Figure 2.15: Photo of version 2 of the LAAPD detector array, which was present during approximately one third of RDK II's operation. This view is shown in the direction that is upstream of the neutron beam. The three LAAPDs are partially visible. The aluminized Mylar wrap around the BGO detector array can be seen at the edges of the photo. All data presented in this dissertation was taken using this version of the apparatus.
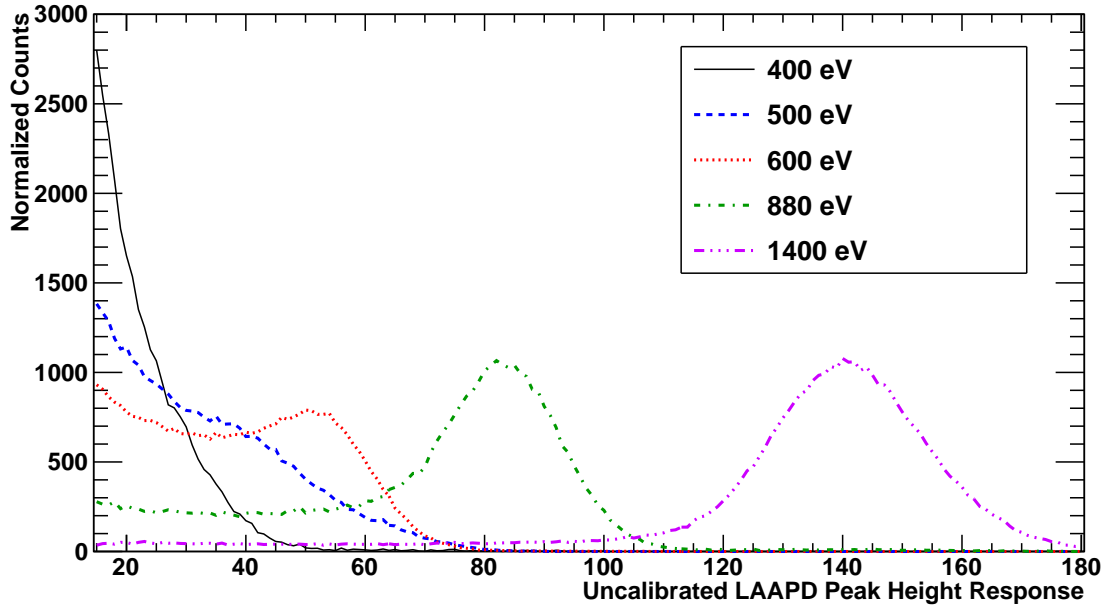
Figure 2.16: Plot of the response of LAAPD to energies from monochromatic light from the monochromator at the National Synchrotron Light Source (NSLS) at Brookhaven National Laboratory (BNL). An ^{55}Fe source produced a peak at approximately channel 600 (not shown), which corresponds to 5.9 keV.

subtracted from the epγ correlated results.

2.6.2 LAAPD Low Energy Response Modeling

The energy response of the LAAPDs was due to variations in photoelectron collection efficiency versus absorption depth [75]. An example of the collection efficiency model that was applied to the simulation can be found in Figure 2.17. The different slopes in the collection efficiency model represent regions where the doping levels varied at different rates. This was determined through both consultation with the manufacturer and through fitting. Overall variations between the individual LAAPDs and the agreement between the two synchrotron measurements resulted a large systematic uncertainty assigned to the LAAPD measurements.
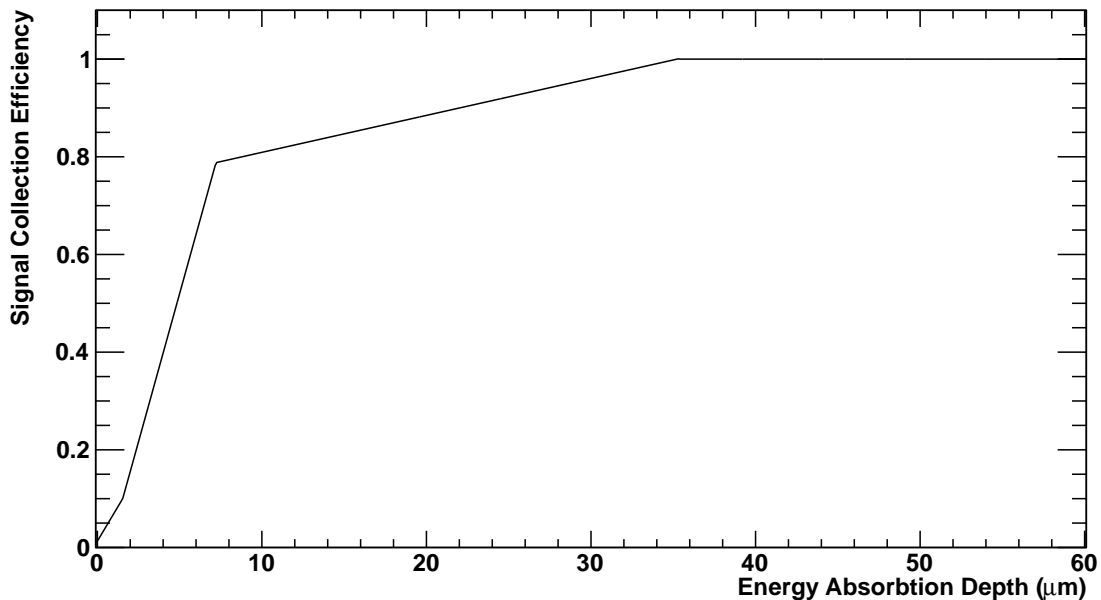
Figure 2.17: Plot of the model used to describe the collection efficiency versus photon absorption depth in one of the LAAPDs used in RDK II.

2.7   Data Acquisition

The goal of the data acquisition (DAQ) system is to convert a detector's particle signal efficiently into data while minimizing both background signals and deadtime. RDK II's DAQ system did this by triggering off of the combination of both an electron and a proton signal.

The signal originating from the SBD first entered a preamplifier, which was within the -25 kV isolation cage with the SBD. The pre-amplified signal was transmitted out of the isolation cage via optical couplers and through an optical fiber. The signal was then split into three signals, with two going to shaping amplifiers and the last to the digitizer channel [56]. One analyzer was set at low gain for the electron signal and the other was set to high gain for the proton signal and both were set to 0.25 μs shaping time. These signals were run through single channel analyzers (SCAs), gate generators, and a time-to-amplitude convertor (TAC) to trigger two digital oscilloscopes to take data (see Figure 2.18 for a diagram of the DAQ system).

The digital oscilloscopes were each 16 bit peripheral component interconnect (PCI) cards made by GaGe Applied Technologies. Each card had eight channels and operated at a 25 MHz sampling rate. The number of active photon detectors varied during RDK II's operation but was ultimately limited to fourteen active detectors as there were a limited
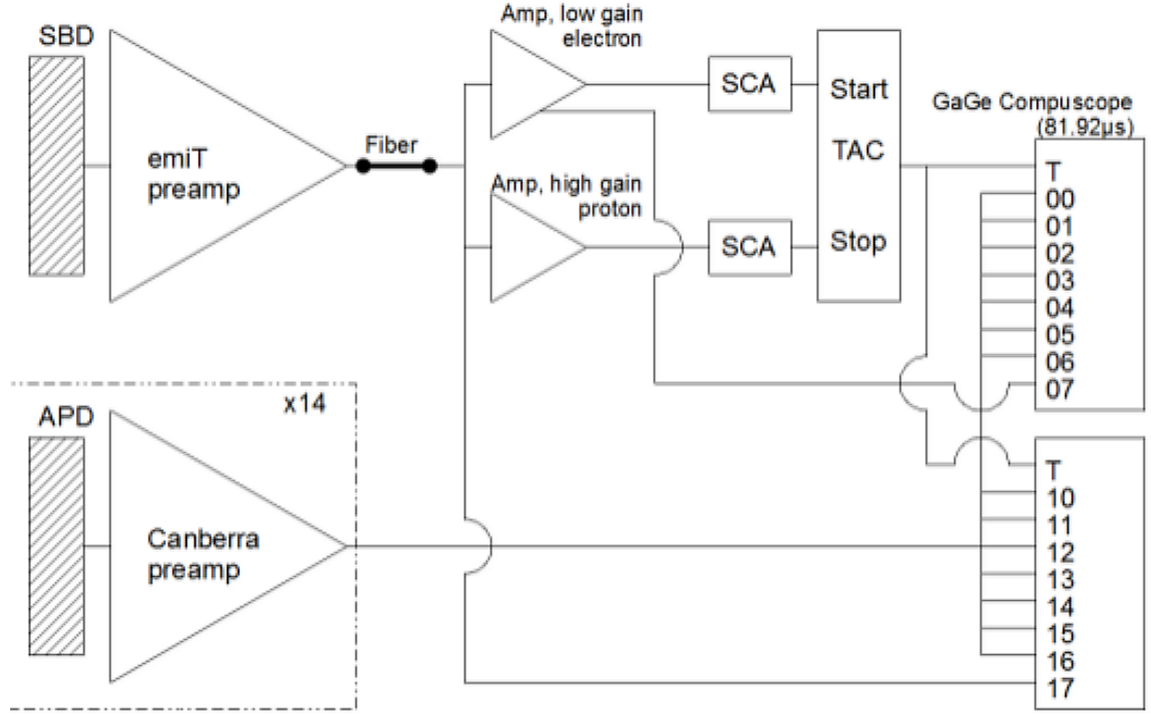
Figure 2.18: Diagram of RDK II's DAQ system. Signals originating from the SBD were used to trigger the digital oscilloscope cards.

number of channels available in the system. This, for instance, resulted in at least one inactive BGO detector during LAAPD operation.

In RDK II's primary operating mode, the voltage triggers were set to record only when a large pulse height with an energy equivalent to at least $\approx$50 keV is followed by a small pulse of at least $\approx$7 keV. This second pulse was required to occur at least 250 ns after the large pulse for the DAQ system to trigger. The exact values of these triggers were gain dependent and were manually set during the experiment's operation. Further and more well defined software cuts are applied later in subsequent analysis (see Chapter 4).

When the DAQ triggered, waveform data were recorded from the SBD detector and both photon detector arrays. These waveforms ranged from $\approx$25 μs before the electron signal and for $\approx$57 μs after and spanned 2048 channels (1 channel = 40 ns) in time.
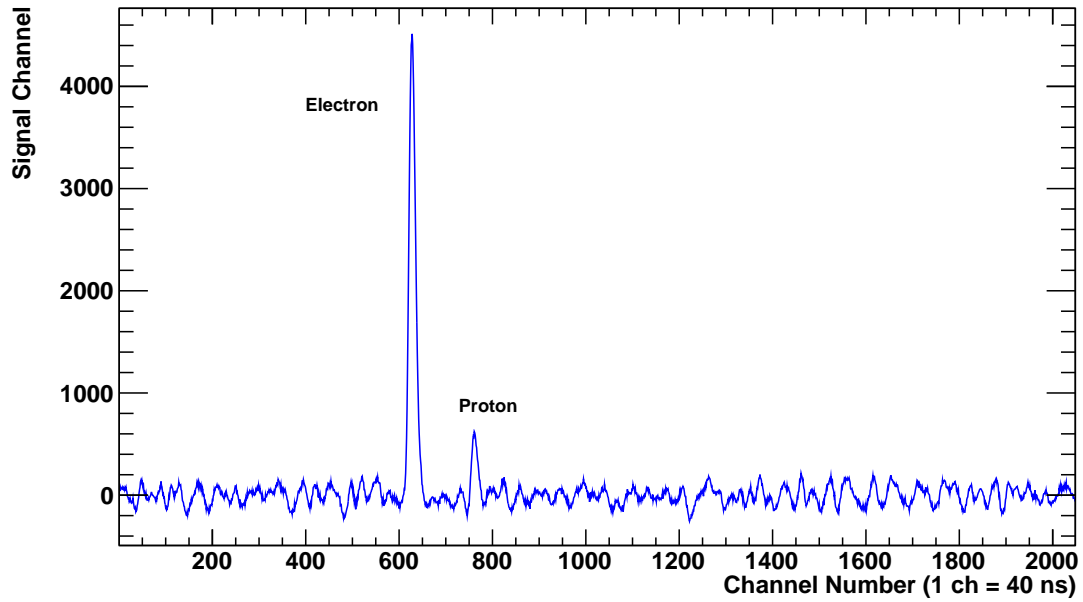
Figure 2.19: Plot of an example ep waveform detected by the SBD.

2.8 Waveform Data Analysis

2.8.1 SBD Waveforms

An example of a signal recorded by the SBD detector (see Section 2.4) is shown in Fig. 2.19. In order to identify the height of both the prompt "electron" peak and the delayed "proton" peak, two waveform analysis methods were utilized: the peak height method and the peak fit method. In both methods, the electron pulse height, the proton pulse height, and the timing between the two was determined. As the electron's travel time is negligable in comparison, on the order of nanoseconds, this time is referred to as the proton's time-of-flight.

The first method, the peak height method, identified peaks by first finding the highest point on the waveform and identifying it as an electron. The algorithm then found the next highest point on the waveform after the electron peak, while presuming a small delay to allow for the electron signal to settle to background levels. This second peak was identified as a proton. Background levels were also measured before the electron signal and subtracted from the recorded electron and proton peak heights.

The second analysis method, the peak fit method, also identified the largest peak and second delayed peak. The primary difference from the peak height method is that this method fit both the electron and proton to a functional form that included a local back-
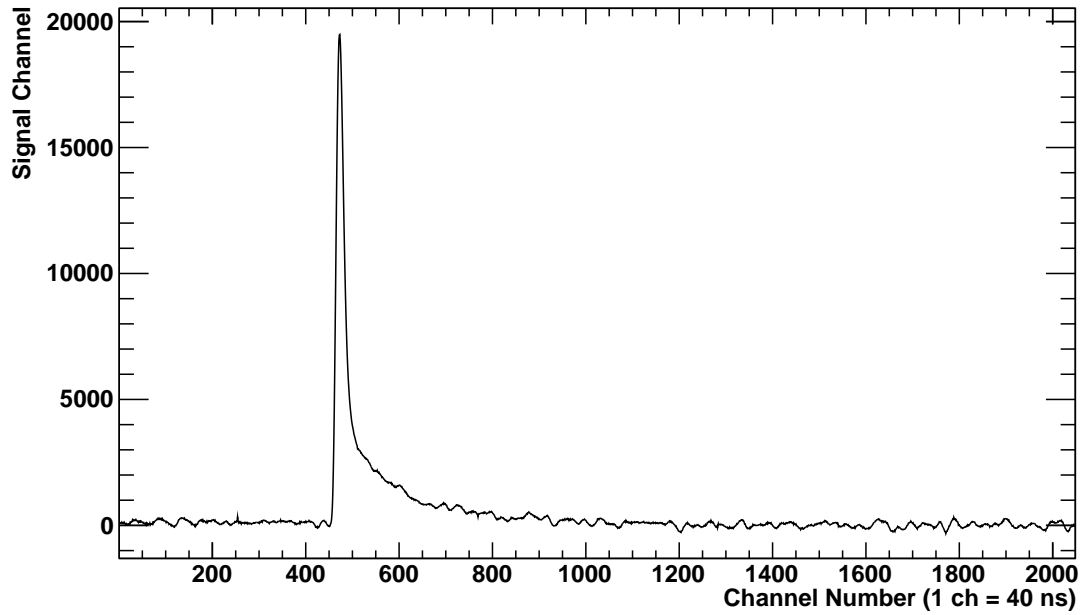
Figure 2.20: Plot of a SBD waveform where the baseline from an electron was not reestablished in the SBD.

ground. The two methods were found to be in general agreement but it was determined that the peak fit method was superior.

There were a few classes of events that showed electronic artifacts. This included events where "ringing" of the electron signal occurred. This was characterized by waveforms that appeared to take the form of a damped harmonic oscillator. Another electronic artifact type was waveforms where the baseline was not reestablished after the electron peak (see Figure 2.20 for an example where the baseline was not reestablished). In both of these cases, the DAQ's ep trigger recorded data but it was unclear whether there was a proton signal or when it occurred. These events were attributable to instrumentation malfunction and were removed from the analysis. Associated systematic errors were estimated based on the quantity of events that were removed.

2.8.2 BGO Waveforms

An example of a signal recorded by a BGO detector (see Section 2.5) is shown in Figure 2.21. As described in Section 2.7, in its primary operating mode, the BGO array was triggered to record only when an ep signal was detected by the SBD. In the analysis, the largest peak in the waveform was fit to a template and a peak height was extracted from it. This template was formed by averaging waveforms from the calibration runs. If the
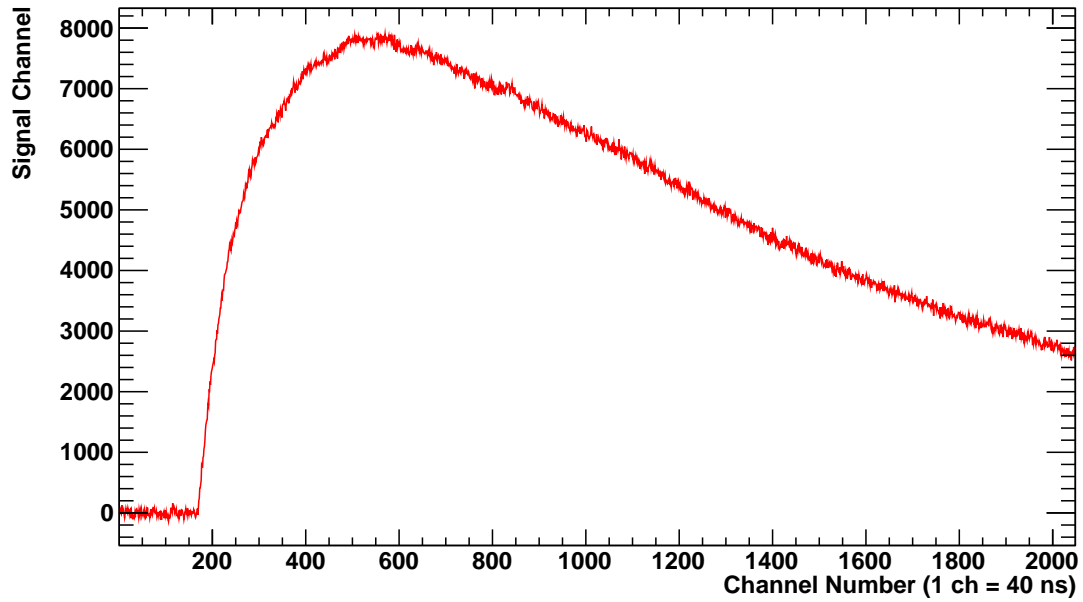
Figure 2.21: Plot of an example waveform from a BGO + APD detector.

extracted peak height was greater than a cut value equivalent to approximately 14 keV, then the BGO was considered to have detected a photon. It was determined that multiple photons within a single ep trigger did not contribute significantly to the analysis.

Photons that were detected at nearly the same time as the electron were primarily radiative photons from neutron decay. Photons detected much earlier or much later in the signal were primarily from background sources of radiation such as neutron capture. This can be seen when detected photons are plotted over time (see Figure 4.1). To determine the number of radiative photons detected, three timing windows were created. A peak window was centered around events near the electron trigger while pre-peak and a post-peak background windows were created in uncorrelated regions. From this, a background subtracted result was determined presuming that background events were equally likely to occur at any time across the data set.

2.8.3 LAAPD Waveforms

An example of a signal recorded by a LAAPD detector (see Section 2.6) is shown in Fig 2.22. As described in Section 2.7 and similar to the BGO detector array in its primary operating mode, the LAAPD array was triggered to record only when an ep signal was detected by the SBD. The largest peak in this waveform was identified (a template fit was not used). This highest point was extracted as the photon peak height. If the peak height

38
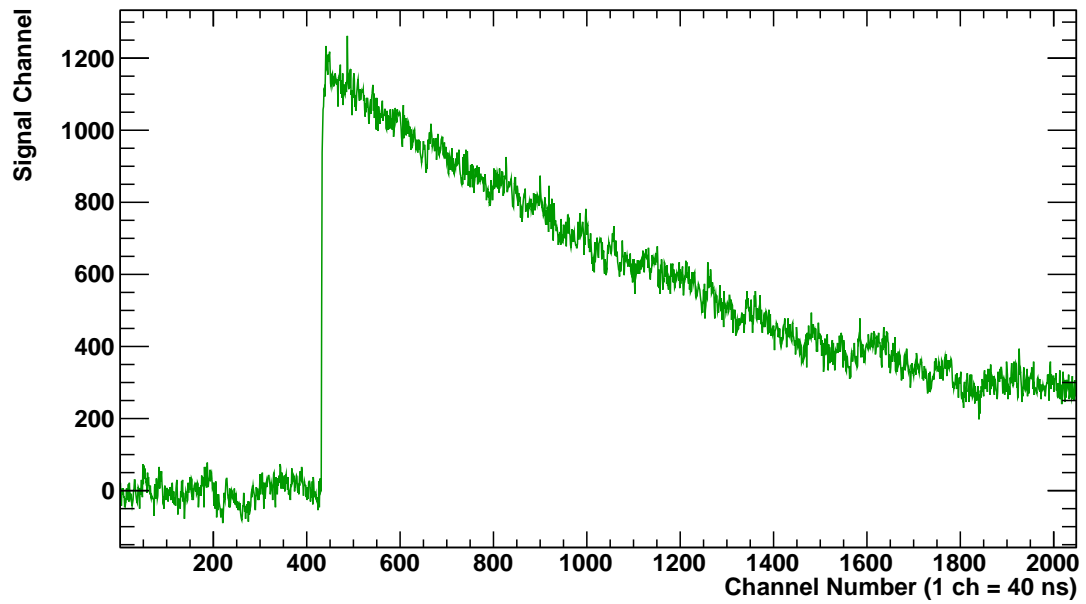
Figure 2.22: Plot of an example waveform from a LAAPD detector.

was greater than a cut value equivalent to approximately 300 eV, than the LAAPD was considered to have detected a photon. It was determined that multiple photons did not contribute significantly to the analysis. Similar to the BGO array, the LAAPD array peak height signals were background subtracted using pre-peak and post-peak windows.

CHAPTER 3

Simulations and Modeling

In this chapter, the Monte Carlo (MC) simulation of the RDK II apparatus is discussed. First, the goals of the simulation are described. Then Geant4, the primary software package used, is covered before detailing each portion of the particle simulation (see Figure 3.1). Some results of the simulations are presented in this chapter, but most results can be found in the comparisons to experimental data in Chapter 4.
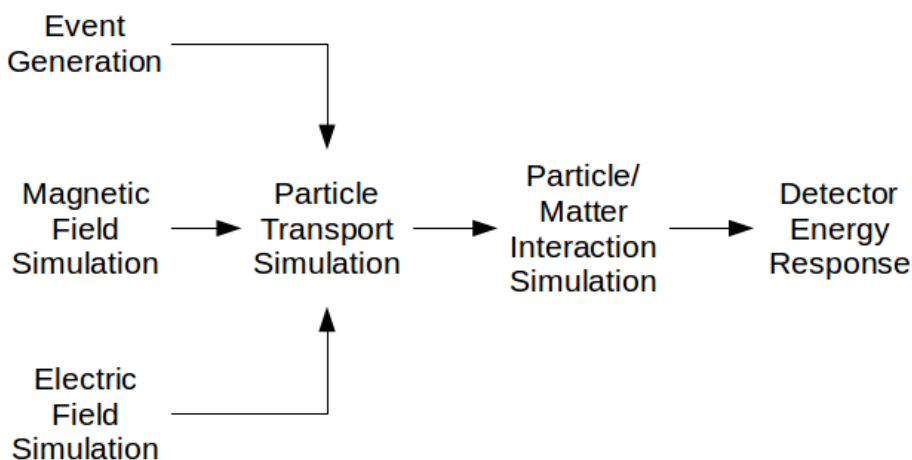
Figure 3.1: Flow chart for the MC simulation of the RDK II apparatus.

3.1 Simulation Goals

A major goal of RDK II was to compare the experimental data with the results from theoretical quantum field theory calculations to determine if theory accurately describes the experimental results. To achieve this, it was necessary to use a detailed simulation to model both the complex geometry and the nonlinear energy response of the apparatus. This simulation served as a bridge between the experimental results from the detectors and the

Detector Type	Calibration Energy
SBD	781 keV
BGO	511 keV
LAAPD	5.9 keV

Table 3.1: Calibration points used to generate the calibrated peak height scale used to compare simulated and experimental data.

predictions of quantum field theory. For instance, at one extreme, it is possible to begin with theoretically generated events and simulate what the resulting waveform voltage responses for each detector would have been. Or, in the other extreme, the results of the experimental analysis could be unfolded using the simulated detector response. This would have generated a prediction of the original energy spectrum of photons, which could then be compared with the result from a theoretical calculation. This latter extreme proved to be too difficult to produce due to the experimental statistics. In addition, as seen in Figure 4.9, the preliminary BGO photon spectrum appears to show a shape consistent with QED theory.

For RDK II, an intermediate path was chosen where calibrated peak heights were intercompared between experiment and simulated theory. A calibrated peak height is the amplitude of a waveform from a detector's response to a particle that is calibrated linearly to a known energy. To do this, MC simulations of neutron decay products generated by theory were transported through the geometry of the active detection region. The simulation then allowed one to estimate the energy absorbed in the sensitive regions of the detector with further energy response effects added to produce calibrated peak height data. The experimental peak height results were in turn linearly scaled by calibration points discussed in Chapter 2 (see Table 3.1). This created a peak height scale that closely represented the energy absorbed in the detectors, but differed depending on the detector's non-linearity. It should be noted that the branching ratio extracted from the experimental measurements, which is discussed in detail in Section 4.2, will be directly comparable to theoretical measurements.

The simulation also provided data in additional channels such as the electron-proton time delay (proton time of flight), the electron peak height, and the proton energy. Comparisons of these additional data channels with experimental data helped to validate the simulation's accuracy. The simulation also allowed for the exploration of phenomena that were impossible to explore in the experiment, which allowed for a better understanding of the experiment's operation. For example, the response of the detectors along the neutron beam (see Figure 2.2b) was not fully understood until the simulation was completed. Finally, the simulation provided an excellent tool to explore systematic uncertainties. This

subject is covered in depth in Chapter 4.

3.2 Geant4

The primary simulation software used in RDK II was Geant4 Version 9.6.p02 [76]. The
Geant4 website [77] describes the software:

> Geant4 is a toolkit for the simulation of the passage of particles through matter.
> Its areas of application include high energy, nuclear and accelerator physics, as
> well as studies in medical and space science.

Geant4 is a C++ library, not a single pre-built software package. This versatility allows
Geant4 to perform well in in a wide variety of particle simulation applications. It is the
user's responsibility to program the geometry, tracking, data storage, and particle interac-
tions that are relevant to the physics of the simulation problem. To assist in this, Geant4
provides extensive example programs that can be built upon and copied from. RDK II's
Geant4 simulation utilized these examples extensively.

The RDK II detection region was modeled directly in C++ code using primitive Boolean
operations on geometric objects such as cylinders and boxes. See Appendix B for additional
details. This approximation is appropriate as the apparatus is very radially symmetric. The
active detection region of each detector was assigned to record the time, location, and
energy of any particle entering or exiting the volume as well as the total energy absorbed
from simulated particles. Data were stored using the ROOT libraries [78, 79]. Particle
transport and particle/matter interactions in Geant4 are discussed in Sections 3.5 and 3.6
respectively.

Geant4 has been used in applications that span many orders of magnitude in energy
(μeV to TeV), however, it was originally created for use in high energy physics. The
range at which neutron decay takes place is considered to be "low-energy" to the default
Geant4 setup. Despite its original purpose, Geant4 has been shown to produce excellent
agreement with experimental results at these energies [80, 81] with some exceptions such
as with electron backscattering. There are two primary low energy physics electromagnetic
interaction libraries used in Geant4: Livermore and Penelope. Both of these libraries were
tested in the RDK II simulation and they produced statistically identical results.

Source	Type	Grid Size	Density	Software
Solenoids	B	89x31x501	1 mm^3	BioSavart
Mirror	E	49x49x221	1 mm^3	COMSOL Multiphysics®
SBD	E	211x121x301	1 mm^3	COMSOL Multiphysics®

Table 3.2: Magnetic and electric fields included in the RDK II Geant4 simulation.

3.3 Electromagnetic Field Calculations

An accurate mapping of the electric and magnetic fields was necessary to track the charged decay products' helical orbits in the apparatus. These fields were both static and highly symmetric. The simulated fields calculated shown in Chapter 2 (see Figures 2.4 and 2.6).

The magnetic field from the solenoids was calculated using a program called BioSavart [82], which integrates Bio Savart's equation along each coil (see Table 3.2).

The electric fields were calculated using a finite element analysis code written in IGOR Pro [83] [9] and then using COMSOL Multiphysics® [84]. All fields were linearly interpolated. Cubic interpolation was confirmed to have a minimal effect on the result of the simulation and had significantly slower performance. Fields were generated for the electrostatic mirror and the SBD (see Table 3.2).

After the RDK II apparatus was removed from the beamline, it was realized that the voltage bias on the second version of the LAAPD detector array could possibly have influenced charged particle transport. This field was modeled in COMSOL Multiphysics®(see Figure 3.2) and it was determined to have minimal impact on simulated results.
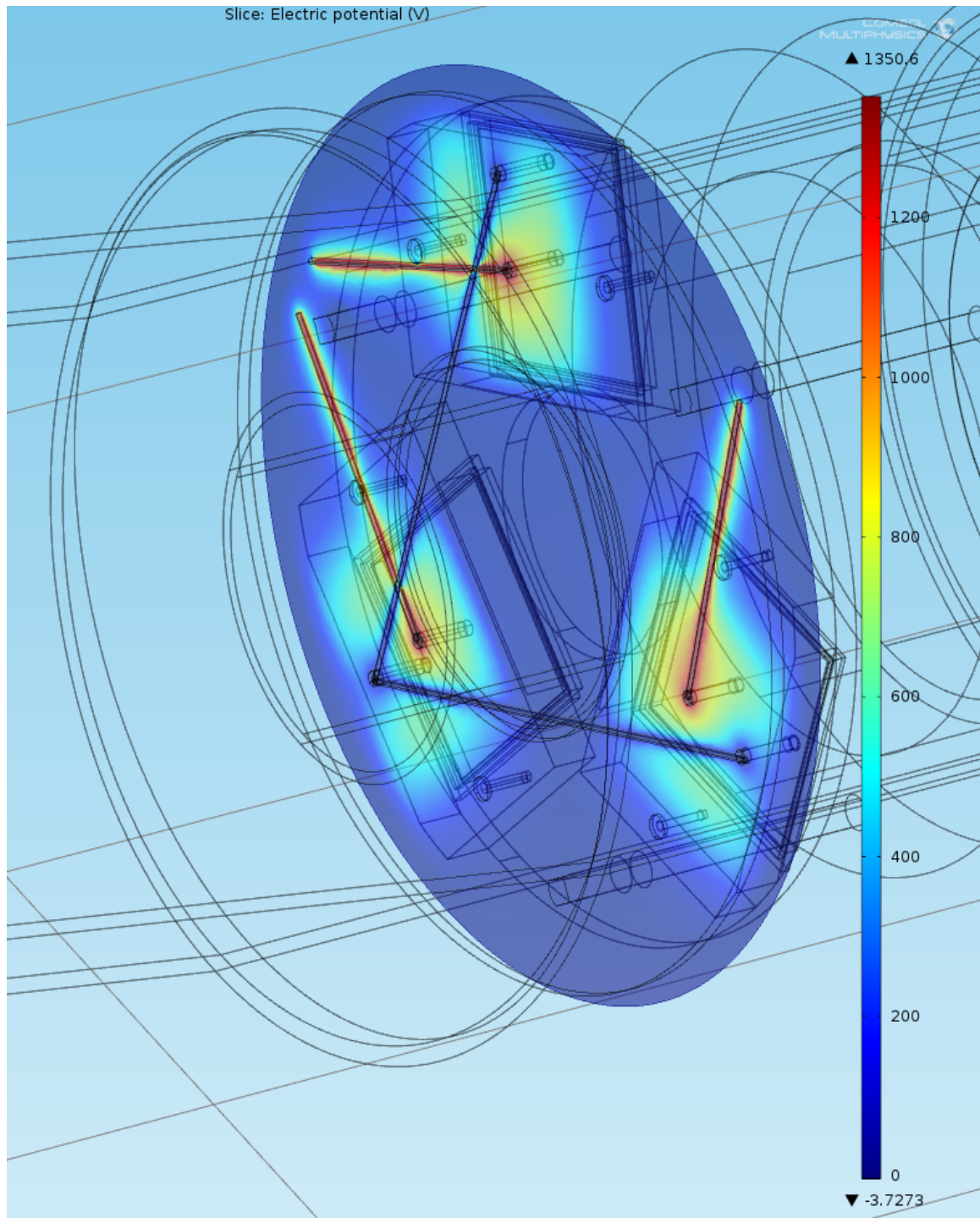
Figure 3.2: COMSOL model of the LAAPD detectors including the high voltage and ground wires that provided the detectors with their voltage bias.

3.4   Event Generation

The momenta and positions of the decay products of neutron decay were randomly generated to begin the MC simulation process. In all cases a pseudo random number generator using the Mersene Twister algorithm [85] was used to generate random numbers, ensuring that no sequence of numbers would repeat itself in practice as the generator has a period of 2^{219937}-1. Events were generated using random, but fixed number seeds determined from atmospheric noise [86]. This allowed for systematic changes in the simulation to be tested easily on identical sets of events and allowed for independent simulation of each of the decay products.

3.4.1   Neutron Beam

A simulated beam profile was created to randomly sample potential neutron decay locations within the sensitive detection region. To generate this profile, an image of the neutron beam was taken 45.68 cm away from the center of the bend in the magnetic field. The image was taken using a sheet of ^{6}Li foil that was exposed to the beam during the experiment's operation. A piece of dysprosium, which is a strong absorber of neutrons, was positioned to indicate the geometric center of the detector. The ^{6}Li film was measured by exposing a photographic plate to the activated foil. The resulting data were translated into a two dimensional histogram that was proportional to neutron flux (see Figure 2.3).

A very small percentage of neutrons decayed over the length of the active detection region, and therefore it was presumed that neutrons decayed uniformly along the beam's path. Through tracking simulations, the regions in which either ep or epγ events could be detected were identified and only decay positions within these bounds were generated to minimize computations. Beam positions were generated randomly in this region: from -18 cm to 62 cm from the bend. The two dimensional histogram of the beam profile was then sampled using Von Neumann rejection. Random x and y coordinates were chosen and then a random number, from 0 to the maximum flux detected, was generated. If the number was greater than the contents of that bin, the process was repeated with a new random coordinate. If the number was less than the bin content, this event was kept and a neutron decay location was generated. A correction was then applied to account for the divergence of the neutron beam as it emerged from the neutron collimating system. The divergence angle, 0.6°, was then used to scale the X and Y coordinates.

3.4.2 Momenta Generation

To generate the momenta of the neutron decay products, rejection sampling or Von Neumann rejection was applied to Eq. (1.8) to generate three-body decays (e, p, and ν) and Eq. (A.1) to generate four-body decays (e, p, ν, and γ). First, as there are 5 independent variables in Eq (1.8), 5 parameters were randomly sampled within their kinematically allowed energy ranges. The parameters chosen were the electron energy (E_e), the electron azimuthal angle (ϕ_e), the cosine of the electron inclination angle ($\cos\theta_e$), the neutrino azimuthal angle (ϕ_ν), and the cosine of the neutrino inclination angle ($\cos\theta_n u$). For four-body decay, there are 8 independent variables. In addition to the previously chosen parameters, four-body decay also randomly generated the photon energy (E_γ), the electron azimuthal angle (ϕ_γ), and the cosine of the electron inclination angle ($\cos\theta_\gamma$). Using conservation of energy and momentum, the four momenta of all particles can be calculated. Kinematically disallowed events are rejected. Using these randomly sampled four momenta, first Eq. (1.8) and Eq. (A.1) were evaluated and a scaled random number was "thrown" against the probability of decay. If the number was greater than the probability of decay, the process was repeated with a new set of randomly generated four momenta. If the number was less than the determined probability, the set of momenta was kept and combined with a randomly determined position. This combination was referred to as a neutron decay event.

Figures 3.3, 3.4, and 3.5 show the theoretical energy spectra from neutron decay for the protons, electrons, and photons respectively.
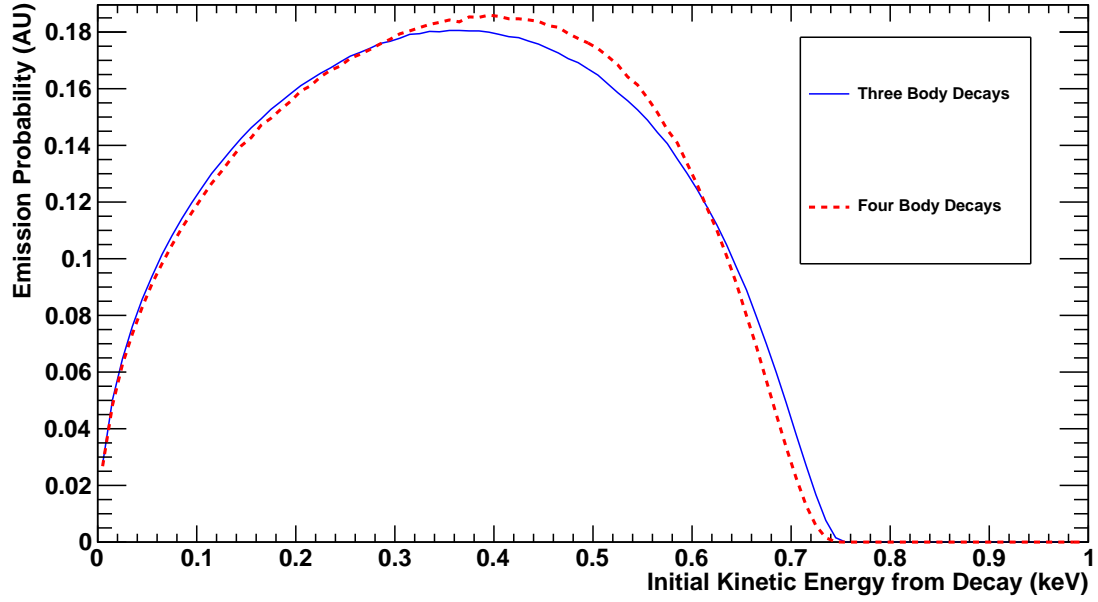
Figure 3.3: Plot of initial proton energies for both three and four-body decays ($E_\gamma > 14$ keV) from the event generator. Curves are scaled to have the same area.
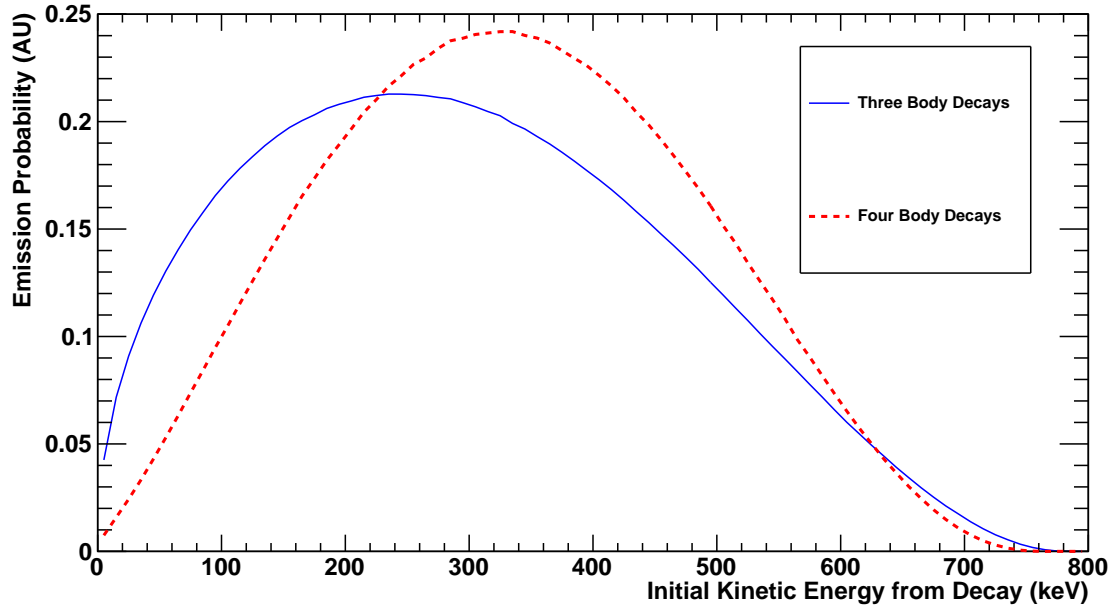
Figure 3.4: Plot of initial electron energies for both three and four-body decays ($E_\gamma > 14$ keV) from the event generator. Curves are scaled to have the same area.
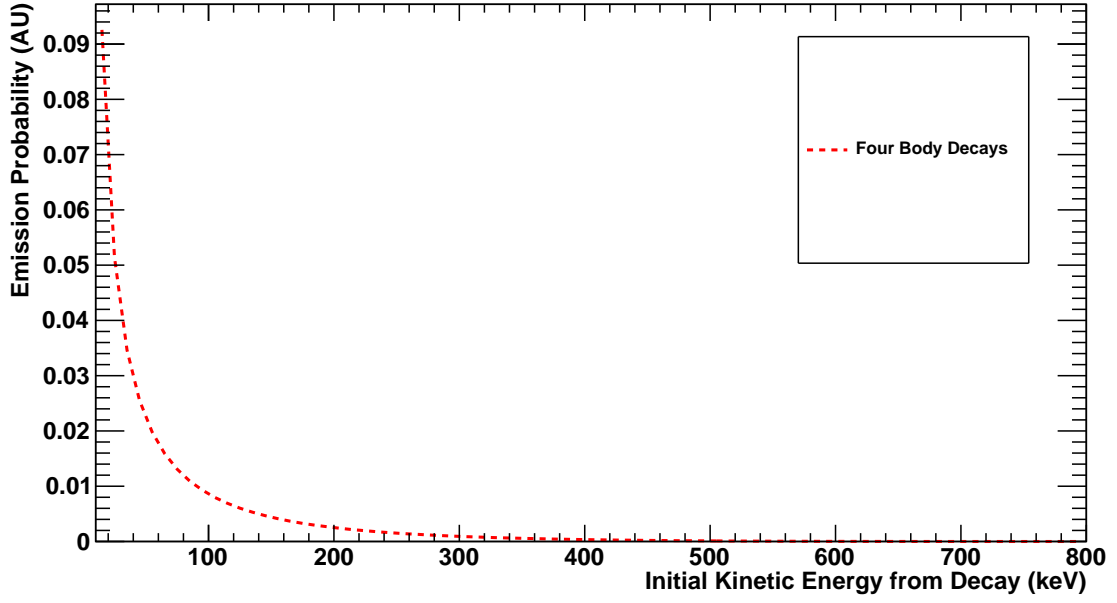
Figure 3.5: Plot of initial photon energies for four-body decays from the event generator.

3.5   Charged Particle Tracking

As described in Chapter 2, protons and electrons followed helical orbits around magnetic field lines and were accelerated or reflected by electric fields. In general the proton and electron tracks obeyed the principles of adiabatic particle motion [87]. In RDK I, both an adiabatic tracking algorithm and a Runge Kutta tracking algorithm were utilized. In RDK II, all MC results presented in this thesis were generated by a Runge Kutta algorithm packaged with Geant4.

3.5.1   Adiabatic Tracking

While an adiabatic particle tracking algorithm was not used in the final RDK II simulation, it is still valuable to discuss. In the RDK II apparatus, the magnetic field varies slowly in time and space relative to the period and radius of the orbits of the protons and electrons. As such, the protons and electrons will travel adiabatically using a guided center of motion [88]. A particle orbiting adiabatically will travel along a magnetic field line with the particle's behavior along the line determined by examining an invariant of motion. One such invariant is [9, 87]

$$\mu = \frac{p_\perp{}^2 c^2}{B},$$

(3.1)

where $p_\perp$ is the component of the particle's relativistic momentum that is perpendicular to the magnetic field, B is the magnetic field strength, and c is the speed of light.

For example, in a purely magnetic field (constant electric potential), the field can do no work on a particle. As B decreases, the invariant tells us that a particle's $p_\perp$ also decreases and, from conservation of energy, its $p_\parallel$, its momentum component parallel to magnetic field, increases. Thus particles transfer transverse momentum to longitudinal momentum in decreasing magnetic fields. The reverse is also true. Particles transfer longitudinal momentum to transverse momentum in increasing magnetic fields.

With the inclusion of electric fields, work can be done on the particles. Fortunately, the effect electric fields have on particles is relatively simple to calculate. A particle with an elementary charge of e and a kinetic energy parallel to the magnetic field line, $E_\parallel$, (expressed in electron volts) could have overcome a potential difference in volts of $\Delta V = E_\parallel / e$ before the potential was strong enough to have reflected the particle. At the center, the experiment's electrostatic mirror had a potential of ≈ 800 V relative to ground. This was sufficient to reflect all protons created at ground as they all had less than 800 eV of kinetic energy. Some electrons, depending on their initial kinetic energy and their emission angle relative to the magnetic field, could also be reflected by the static electric field.

3.5.1.1 Magnetic Reflection

While an adiabatic algorithm was not implemented in RDK II, the principle of adiabatic motion was used to investigate the phenomenon of the magnetic-mirror effect. A magnetic mirror occurs when a particle adiabatically travels from a low magnetic field to a sufficiently high magnetic field such that all of the longitudinal momentum is transferred to the transverse momentum. When this happens, a turning point is reached and the particle will reverse its motion along the magnetic field line, traveling backwards along its previous path.

In RDK II's active detection region, the magnetic field strength was relatively constant along the neutron beam, and the magnetic field strength decreased as the field lines approached the SBD (see Figure 2.4). As such, particles did not undergo magnetic reflection on their way to the SBD. Upon reaching the SBD, protons were accelerated by the SBD's negative potential and were eventually absorbed. Electrons, on the other hand, had a significant probability of backscattering off of the SBD's silicon (see Section 3.6). These scattered electrons were then accelerated away from the SBD, back towards the magnetic field bend and the neutron beamline. These electrons had the potential to see a magnetic mirror effect depending on their kinetic energy parallel to the magnetic field ($E_\parallel$), which can in turn be determined by the backscattered kinetic energy and the angle at which they

scattered from the silicon's surface. Specifically, an energy dependent critical angle, θ_c, can be determined. This angle was defined by the particle's scattered momentum relative to the SBD's surface normal. If the electron was emitted at an angle larger than this critical angle, it was magnetically reflected. If it was smaller, it overcame this difference in magnetic field and it exited the experiment downstream.

To solve for the critical angle (θ_c), two points in space were considered: the point where the electron was emitted (designated by $\mathbf{x_0}$) and the point of the highest magnetic field strength along the magnetic field line (designated by $\mathbf{x}_F$). If the electron passed by the point $\mathbf{x}_F$, then the electron traveled out of the experiment as no field, electric or magnetic, existed within the RDK II apparatus to stop it. To determine whether a backscattered electron's angle and energy would have caused it to be backscattered, it was sufficient to determine if it was reflected at the point in space corresponding to $\mathbf{x}_F$. By requiring the component of momentum that was parallel to the magnetic field ($P_{F_\parallel}$) to be zero, the solution will give a critical angle for a particular energy.

From Eq. (3.1):

$$\frac{P_{0_\perp}{}^2 c^2}{B_0} = \mu = \frac{P_{F_\perp}{}^2 c^2}{B_F}, \tag{3.2}$$

where B_0 & P_0 and B_F & P_F are the magnetic field strengths and electron momenta at $\mathbf{x_0}$ and $\mathbf{x}_F$ respectively. The term, c is the speed of light. From Eq. (3.2), it can then be shown that

$$P_{F_\perp}{}^2 c^2 = \frac{B_1 P_{0_\perp}{}^2 c^2}{B_0} = \frac{B_F P_0{}^2 c^2 sin^2\theta}{B_0}, \tag{3.3}$$

where θ is the polar angle from the SBD's surface normal vector. The relativistic energy equation at $\mathbf{x_0}$ is $T_0{}^2 = P_0{}^2 c^2 + m_e{}^2 c^4$, where m_e is the mass of the electron and T is the total energy of the electron. Substituting this into Eq. (3.3):

$$P_{F_\perp}{}^2 c^2 = \frac{B_F(T_0{}^2 - m_e{}^2 c^4)\sin^2\theta}{B_0}. \tag{3.4}$$

For $\mathbf{x}_F$, the energy-momentum relation is

$$T_F{}^2 = P_{F_\perp}{}^2 c^2 + P_{F_\parallel}{}^2 c^2 + m_e{}^2 c^4. \tag{3.5}$$

The SBD's electric potential (ΔV) accelerated the scattered electron, with charge e, back into the experiment. Thus,

$$T_F = T_0 + e\Delta V. \tag{3.6}$$

Substituting Eq. (3.4) & Eq. (3.6) into Eq. (3.5) while setting $P_{F_\parallel} = 0$ determines the

Electron Kinetic Energy (keV)	Critical Angle (degrees)
0	90*
50	90*
100	73
150	67
200	65
400	62
800	60

Table 3.3: The electron's critical angle of magnetic reflection from the SBD in the RDK II apparatus. The energy indicated is the kinetic energy after backacattering. Backscatter emission angles below the critical angle were not reflected (see Eq. (3.8) with B_0 = 3.3 T and B_F = 4.6 T). 90* indicates that no magnetic reflection in the apparatus was possible at this reflected energy.

critical angle, θ_c:

$$(E_0 + e\Delta)^2 = \frac{B_F(E_0{}^2 - m_e{}^2c^4)\sin^2\theta_c}{B_0} + m_e{}^2c^4. \tag{3.7}$$

Rearranging Eq. (3.7)

$$\sin\theta_c = \sqrt{\frac{B_0((T_0 + e\Delta)^2 - m^2c^4)}{B_F(T_0{}^2 - m^2c^4)}}. \tag{3.8}$$

It should be noted that removing the SBD's electric field simplifies the equation and removes its electron energy dependence:

$$\theta_c = \sin^{-1}\left(\sqrt{\frac{B_0}{B_F}}\right). \tag{3.9}$$

If θ_c is greater than 90°, this indicates that the particle did not magnetically reflect, no matter what angle it scattered into. The results of Table 3.3 show that magnetic reflections do not affect energies below 50 keV but they do affects a significantly large amount of the backscattered electrons at higher energies. Initially, the RDK II particle tracking simulation did not track backscattered electrons, as it was presumed that they did not significantly contribute to the signal. It was later shown to be an important component necessary to generate an accurate electron spectrum.

3.5.2 Runge-Kutta Tracking

As the adiabatic assumption could be violated in a number of locations in the apparatus, a more exact and precise solution was desired for RDK II particle tracking. The relativistic Lorentz force law governing the forces on the particles can be written as [89]

$$\frac{d^2\mathbf{x}}{dt^2} = \frac{d\mathbf{v}}{dt} = \frac{q}{m}\sqrt{1 - v^2/c^2}\left[\mathbf{E}(\mathbf{x}) + \mathbf{v} \times \mathbf{B}(\mathbf{x}) - \frac{1}{c^2}(\mathbf{v} \cdot \mathbf{E}(\mathbf{x}))\mathbf{v}\right], \tag{3.10}$$

where $\mathbf{v}$ is the velocity of the particle, $\mathbf{x}$ is the location of the particle, t is the local time, q is the charge, m is the mass, $\mathbf{E}$ is the electric field, $\mathbf{B}$ is the magnetic field, and c is the speed of light.

Eq. (3.10) must be integrated to determine where a particle traveled. One way to integrate this equation would be to use Euler's method. This method must be used on first order ordinary differential equations (ODEs). To determine $\mathbf{x}(t)$ based on initial conditions a second first order ODE,

$$\frac{d\mathbf{x}}{dt} = \mathbf{v}, \tag{3.11}$$

must also be defined. This creates a set of two coupled first order ODEs.

Using the initial conditions of the decay particle calculated in Section 3.4, a small step in time of size h can be taken. The results of this small, linear step modifies both the velocity and position of the particle according to Eq. (3.10) and Eq. (3.11). This process can be repeated for many steps until the desired result is reached. The accuracy of Euler's method is of course tied to the size of the step taken. Smaller steps result in better approximations of the integral.

Euler's method is an example of a first order ODE numerical integration method. Higher order methods exist and are generally classified as Runge-Kutta methods [90]. Of particular interest is the fourth order method, which has been proven to be robust, fast, and accurate [91]. It is typically simply called Runge-Kutta method (RK4).

Given a first order ODE,

$$\frac{d\mathbf{y}}{dt} = f(t, y), \ y(t_0) = y_0, \tag{3.12}$$

where $\mathbf{y}$ can be a vector or scalar quantity, it is then possible to integrate it iteratively over
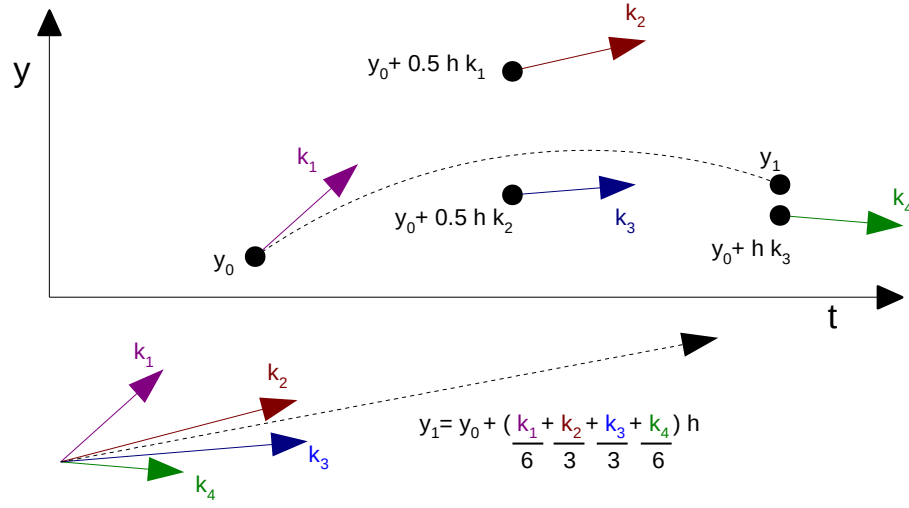
Figure 3.6: An example of the four trial steps taken by the RK4 algorithm and the resulting average that it outputs over a time step h from y_0 to y_1. This approximates the dashed curve that represents the actual path.

a step size h using

$$y_{n+1} = y_n + \frac{h}{6}(k_1 + 2k_2 + 2k_3 + k_4)$$

where

$$
\begin{aligned}
k_1 &= f(t_n, y_n) \\
k_2 &= f(t_n + \frac{h}{2}, y_n + \frac{h}{2}k_1) \\
k_3 &= f(t_n + \frac{h}{2}, y_n + \frac{h}{2}k_2) \\
k_4 &= f(t_n + h, y_n + hk_3).
\end{aligned}
$$

(3.13)

In essence, this algorithm takes four trial steps and then averages them together into a single larger step (see Figure 3.6). In the case of Eq. (3.10) and Eq. (3.11), they must be evaluated simultaneously at each trial step as the magnetic and electric fields are position dependent. The algorithm as described has a fixed time step, h, but the RK4 algorithm can also be extended to automatically adjust its time constant to output a fixed precision at the cost of an extra step of computation. This is called a dynamic RK4 algorithm [91].

53

Initially, both a fixed and dynamic RK4 algorithm for particle tracking were created in the analysis software, IGOR Pro. This proved to be too computationally intensive for further use, though it compared favorably with adiabatic calculations. The program was then ported to C++, which significantly improved computational performance. It also compared favorably with experimental results such as proton time of flight.

Subsequently, the dynamic RK4 algorithm built into Geant4 was utilized for all particle tracking. In Geant4, the charged particle tracking algorithm is called a "stepper". The Geant4 libraries contain many different steppers operating at many different orders. These were tested extensively to determine if any provided significantly different results from the RK4. None did. Geant4's tracking was also compared on identical event sets to the custom C++ tracking algorithm. This produced nearly identical results.

3.6   Particle and Matter Interactions

The RDK II detectors' peak height responses were each proportional to some function of the energy absorbed in their sensitive regions. Geant4 was used to determine the amount of energy absorbed in these active regions. In the case of the SBD and the LAAPDs, the active region consisted of doped silicon. For the BGOs detectors, the active region was considered to be the scintillator volume. Response contributions from nonproportionality and the light collection of the BGO's APD were applied later.

In Geant4, stable particles propagate until they have either left the simulated volume or are absorbed in the matter. Geant4 tracks particles to absorption by utilizing a production threshold for secondary particle generation. This threshold is defined as a distance. As the particle path is tracked, Geant4 will determine if secondary particles that can travel at least this threshold range can be generated. If the parent particle can generate secondaries, probabilistic secondary particle generation will determine the parent particle's energy loss mechanism in the matter. When this threshold is passed, a continuous energy loss formulation is used instead and the particle is tracked down to zero energy. This threshold is based on particle range instead of energy cutoff to account for the dramatically different ranges particles have in matter. The default threshold is 1 mm. In the RDK II simulation, this threshold was set to 1 nm. This was determined by recommendations from the literature [81] as well by adjusting the parameter to ensure invariance in the simulated results. For protons traveling through the gold layer and the inactive "dead" silicon layer of the SBD, it was determined that a threshold of 0.001 nm was sufficient.

Geant4 uses theoretical models, parametric fits to experimental data, and interpolation of public-domain data tables to determine a probabilistic model of particle and matter in-

teractions. For the Geant4 Livermore low energy library, the evaluated data libraries used were the EADL [92], EEDL [93], and EPDL [94] for atomic, electron, and photon data respectively.

Low energy photons in Geant4 can undergo either photoelectric conversion or Compton scattering. For the photoelectric effect, Geant4 uses "a parameterized photon absorption cross section to determine the mean free path, atomic shell data to determine the energy of the ejected electron, and the K-shell angular distribution to sample the direction of the electron." [95] Compton scattering is handled by calculating the Klein-Nishina differential cross section [96] while ignoring atomic shell effects.

For the BGO detectors, the photoelectric effect was particularly important. Higher energy photons can excite a K-shell electron in bismuth, which then can emit an ≈80 keV photon. If this occurred near the surface of the BGO, this secondary photon could have escaped the scintillator causing incomplete energy deposition. These K-shell x-rays were visible in the final photon spectrum (see Figure 4.9). These x-rays also provided for an calibration line when the neutron beam is on for the the BGO photon spectrum. This line allowed for a nonproportionality was evaluation [73].

Low energy protons and electrons in Geant4 can undergo elastic or inelastic Rayleigh scattering, bremsstrahlung, and ionization. In addition, Geant4 will model the resulting fluorescence and Auger electron emission of excited atoms.

Of particular importance is the case of elastic scattering. Since the elastic scattering cross section increases as the energy decreases, simulations become computationally intensive at lower energies. While Geant4 has a calculation mode, called "single scattering" that will simulate every elastic scattering event down to an arbitrary range cutoff, it is only feasible to do this for small test cases. Instead, multi-scattering algorithms are generally used to condense multiple scattering events into a net momenta change to the electron as determined by phenomenological approximations.

For low energy electrons, both theory and experiments have had difficulty in arriving at a consensus for quantity of electrons scattered from silicon, even at normal incidence [66, 80,81,97–100]. In the RDK II simulations, the default multi-scattering algorithm was used, but for small test cases, the single scattering algorithm was shown to agree well with the multi-scattering algorithm above 100 keV using the epγ/ep ratio method (see Section 4.2 for discussion of this analysis method).

Simulations were created for the calibration measurements taken off the neutron beam with radioactive sources for the SBD and BGO detectors (see Sections 2.4.1 and 2.5.1. This included both Geant4 simulations as well as simulations which utilized the Monte Carlo N-Particle (MCNP) transport code, Version 5 [101], which originates from Los Alamos

National Laboratory (LANL). MCNP was used validate Geant4 results. Agreement between the simulations was found to be good and sufficient for RDK II across all calibration sources and detectors.

3.7   Detector Response

Geant4 simulations determined the energy deposited by the daughter particles of neutron decay, but, as described in Section 3.1, the desired output of the MC simulation was in terms of a calibrated detected peak height. To achieve this, further processing was performed for all three detector types to add in their response. This was handled in C++ code that utilized ROOT libraries.

For the SBD, each energy deposit was randomly shifted by a Gaussian distribution to replicate energy resolution observed from source calibration measurements. This resolution was sufficiently constant in the energy range measured that a single FWHM of 5.4 keV was applied at all energies. In addition, a 20 nm thick dead layer of silicon was applied to the model to match proton energy distribution observed in the experimental data.

For the BGO detectors, the energy deposited was first adjusted to account for BGO non-proportionality by using a parametric fit to available data, as described in Section 2.5.1.2. Then, an energy independent correction for the position dependent light collection was applied, as described in Section 2.5.1.1. Finally, each adjusted energy deposit was randomly shifted by a Gaussian distribution to replicate energy resolution observed from source calibration measurements. In calibration measurements, this energy resolution varied slightly between individual BGO crystal and APD detectors and the detectors resolution exhibited energy dependence consistent with Poisson statistics. At 511 keV, the resolution's FWHM was ≈60 keV.

For the LAAPD detectors, the phenomenological model of charge collection described in Section 2.6.2 was applied during the Geant4 simulation. A 35 nm thick silicon dioxide layer reported by the manufacturer was also simulated on the outside of the LAAPDs. The energy resolution of the detectors was found to follow the following equation [75]

$$\text{FWHM} = \sqrt{57.6C + 0.144C^2}E, \tag{3.14}$$

where C is the collection efficiency, ranging from 0 to 1, at the depth the energy was absorbed and E is the energy in eV.

CHAPTER 4

Data Comparisons and Systematic Analysis

This chapter addresses the details of comparing the experimental data with simulations of theoretical predictions. First, a summary of experimental data is presented, which is followed by comparison methodologies. Next, a series of comparison plots are presented, followed by a summary of the systematic corrections and uncertainties present in the experiment.

An important note: All plots and results found in this dissertation are considered to be preliminary.

4.1   Experimental Data Summary

RDK II began operating on the beam line in December, 2008 and acquired its last neutron decay event in November, 2009. The data were divided by cycle, series, and run, with a cycle being the largest division of the data and a run being the smallest. Some data series were taken as diagnostics to evaluate systematic effects. This included series where the solenoid was turned off, the electrostatic mirror was varied, and the neutron beam was off.

As in RDK I, non-systematic data were taken at variety of electrostatic mirror voltages in data cycles 1 and 2. It was noticed that the ep trigger rate did not change as expected from 0 to 50 V on the mirror. Through investigations of the proton time-of-flight data, it was determined that there was a possibility of an anomalous electrostatic potential in the region downstream of the mirror that affected low energy protons. To address this issue, all further data, cycles 3 through 8, were taken at full, 1400 V mirror voltage. For full mirror voltage, there were approximately 64 million ep triggered events.

Later, during the analysis of the data, it was determined that data cycles 3 and 4 showed systematic disagreement with the MC simulation's proton time-of-flight spectrum. It was postulated that insufficient grounding of internal components was to blame. It was decided that the data from these cycles would be removed from the final analysis on this basis. The

Cut Name	Cut Value
Minimum Proton Energy	7 keV
Maximum Proton Energy	31 keV
Minimum Electron Energy	100 keV
Maximum Electron Energy	800 keV
Minimum Electron-Proton Time Difference	2 μs
Maximum Electron-Proton Time Difference	10 μs
Minimum BGO+APD Photon Peak Height	10
Maximum BGO+APD Photon Peak Height	800
Minimum LAAPD Photon Peak Height	0.3
Maximum LAAPD Photon Peak Height	20

Table 4.1: Preliminary Analysis Data Cut Table. These represent software cuts that must be applied to both the experimental and simulated data.

remaining cycles (5, 6, 7, and 8) included ≈21 million ep events and ≈1,700 epγ events after background subtraction per BGO detector after the analysis cuts were imposed (see Table 4.1). The second version of the LAAPD array (see Section 2.6) operated during data cycles 7 and 8 and it recorded ≈300 background subtracted epγ events per detector.

4.2   Experiment and Simulation Comparison

A few important determinations were made to ensure that comparisons between experimental and simulated data were accurate. For epγ coincidence, a decision was made on how to combine data from the individual detectors for each array. There were two detector combination methods that were considered. The first combination method was to add together all energy/peak heights from each detector in the array for each ep trigger. This essentially treated the array as a single photon detector. The second combination method was to analyze each BGO or LAAPD detector individually and later average their peak height responses. This individual detector method was the method chosen due to a significant number of series where one or more BGO detectors were not operational. This created complications in simulation as bismuth x-rays from inactive BGO crystals could significantly affect the energy spectrum near 80 keV.

As covered in Chapter 3, both the experimental and simulated photon data were expressed in units of calibrated peak height. While this ensured that the shape of both the experimental and simulated photon spectra were correctly compared, their relative scale was still not comparable. Two measurement methods were investigated which produced a scale where the spectra could be inter-compared: the epγ/ep ratio method (see Section 4.2.1) and the neutron flux method (see Section 4.2.2).

For either measurement method, there were two techniques of extracting a radiative branching ratio. The first technique, the integration technique, compares only the integral number of counts within a photon energy range when evaluating Eq. (4.4) or (4.8). The second technique, the fit technique, performs a chi-squared fit by allowing the branching ratio to float as a scaling constant. The chi-squared fit technique puts a greater emphasis on finding a branching ratio that will match the energy spectrum over the entire range. The integration technique, on the other hand, emphasizes whether a photon is on one side of the lower energy cutoff or the other. Both techniques were shown to agree within their respective uncertainties. As such, the difference between the two was taken as a systematic uncertainty (see Section 4.3).

4.2.1 Ratio Method

The epγ/ep ratio method was the same method used by RDK I. For the experimental data, a number of ep counts (C_{ep}) and a number of background corrected epγ counts ($C_{ep\gamma}$) were determined for a given series or set of series. The ratio, R_{Exp}, was formed:

$$R_{\text{Exp}} = \frac{C_{ep\gamma}}{C_{ep}}. \tag{4.1}$$

R_{Exp} has the advantage of being independent of the neutron flux, and many systematic corrections or uncertainties related to ep coincidence detections cancel when equally affected by three-body and four-body events.

A similar ratio (R_{Sim}) was formed from the simulated data. The ratio was slightly more complicated as three-body decay events (D_3) and four-body decay events (D_4) can both create electron and proton coincidence (ep) and electron, proton, and photon/gamma coincidence (epγ). The result is

$$R_{\text{Sim}} = \frac{B S_{ep\gamma}(D_4) + (1 - B) S_{ep\gamma}(D_3)}{(1 - B) S_{ep}(D_3) + B S_{ep}(D_4)}, \tag{4.2}$$

where B is the radiative branching ratio and S_{ep} and $S_{ep\gamma}$ is the probability of detection per event for each coincidence from the simulation.

The quantity, $(1 - B) S_{ep\gamma}(D_3)$, arises primarily from external electron bremsstrahlung occurring in the SBD. This allows the electron to both cause an ep trigger while still emitting photons that could be detected by the BGO detectors. A correction was applied and is accounted for in Section 4.3. It can also be assumed that $(1 - B) S_{ep}(D_3) + B S_{ep}(D_4) \approx B S_{ep}(D_3)$ as $B << 1$ and D_3 and D_4 have similar initial ep spectra.

With electron bremsstrahlung set to be a systematic correction, this results in

$$R_{\text{Sim}} = \frac{B S_{ep\gamma}(D_4)}{S_{ep}(D_3)}.$$ (4.3)

Presuming that the theory and simulation correctly modeled reality, $R_{Exp} = R_{Sim}$. If they do not agree, the source of the discrepancy must be present in one of the three terms in Eq. (4.3). The branching ratio will be calculated by combining Eq. (4.1) and Eq. (4.3) and allowing the branching ratio to vary:

$$B = \frac{R_{\text{Exp}} S_{ep}(D_3)}{S_{ep\gamma}(D_4)}.$$ (4.4)

Importantly, this branching ratio extraction presumes that the distribution of momenta that arises from QED theory is unaltered, even if the branching ratio extracted is different than theory. Given the agreement of the MC simulation with the experimental data in other data channels, this appears to be a reasonable assumption.

4.2.2   Flux Method

The other method that could be used to calculate the branching ratio used the neutron capture flux measured by the neutron beam monitor discussed in Section 2.2.3. This allowed for an absolute measurement that is independent of non-radiative neutron decay detection. For the experiment, a rate of epγ detections (r_{Exp}) was determined by dividing by the amount of time (t) over which the data was acquired:

$$r_{\text{Exp}} = \frac{K C_{ep\gamma}}{t},$$ (4.5)

where K is a dead time correction factor associated with the DAQ system. It was measured to be equal to ≈ 0.96, or 4% dead time.

Neutron capture flux, F_n, measured by the beam monitor is defined to travel at 2,200 m/s. Using this definition, a determination of the neutron decay rate in the simulated volume (n_{Sim}):

$$n_{\text{Sim}} = F_n \left(1 - \exp - \frac{L_{\text{Sim}}}{2,200 \frac{m}{s} \tau_n} \right),$$ (4.6)

where L_{Sim} is the neutron beam length that is simulated (see Section 3.4.1) and τ_n is the neutron lifetime. Using the probability of epγ detection per four-body events ($S_{ep\gamma}(D_4)$), the rate of electron, proton, and photon/gamma coincidence (epγ) determined by simula-

tions (r_{Sim}) was

$$r_{\text{Sim}} = BS_{ep\gamma}(D_4)n_{\text{Sim}} = BS_{ep\gamma}(D_4)F_n\left(1 - \exp{-\frac{L_{\text{Sim}}}{2,200\frac{m}{s}\tau_n}}\right). \qquad (4.7)$$

Similar to the epγ/ep method, a branching ratio was extracted:

$$B = \frac{r_{\text{Exp}}}{S_{ep\gamma}(D_4)n_{\text{Sim}}}. \qquad (4.8)$$

The disadvantage of this method is that it does not automatically cancel systematic corrections or uncertainties related to electron and proton detection, such as those from SBD dead time. This method is advantageous in that it does not depend on ep coincidences that originate from near the bend in the magnetic field. These ep coincidences were problematic because their helical paths do not project evenly onto the SBD. In regions downstream of the bend and near the photon detectors, the neutron beam and the magnetic field are parallel and relatively constant, which causes a symmetric projection of electrons and protons onto the SBD. Positional uncertainties in the neutron beam, the magnets, and the SBD can all influence whether an electron or proton originating from the bend region will hit the SBD or miss it. In the end, it was determined that efforts would be focused on the epγ/ep method as the uncertainty analysis was better understood. The neutron flux method will be evaluated for a possible future analysis.

4.2.3 Plots of Experimental and Simulated Data

This section contains both plots of experimental data and plots comparing experimental data with simulated theory. All experimental data are from the peak height method identified in 2.8.2 unless otherwise indicated. All simulated spectra have been scaled such that their integrals are identical to that of the experimental spectra. For all epγ hists, the average response per photon detector is plotted. All data are preliminary.

Figure 4.1 is a plot of the electron-photon timing spectrum under ep cuts for the BGO detectors, and it is the most straightforward demonstration that radiative neutron decay events are detected by the apparatus. A signal from correlated electrons and photons can be seen near zero time delay. This is due to the near simultaneous detection of electrons and photons produced by neutron decay. It is not centered at zero only due to differences in how the peak location is identified and timing differences between the boards. The uncorrelated photon background can also can be clearly seen and is constant on either side. Pre-peak and post-peak windows were created for background subtraction (see Section 2.8.2).

Figure 4.2 is a plot of the epγ/ep ratio for the BGO detectors for each series with
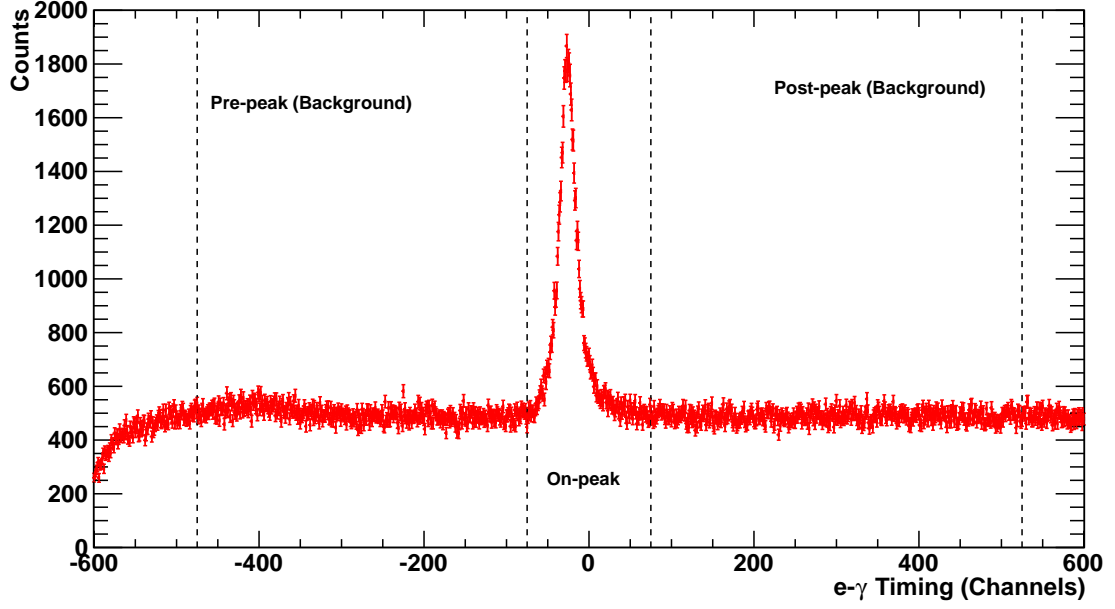
Figure 4.1: Plot of the electron-photon timing spectrum for the BGO detectors. The timing peak located near zero channels of separation is the clear indicator that radiative neutron decays were detected.

electron and proton cuts for the experimental data. The data are consistent with a line of constant slope within its statistics.

Figures 4.3 and 4.4 are plots of the proton energy spectra under ep and BGO epγ cuts. In general, agreement is very good between experiment and simulation, athough there is a small amount of noise that is present in the lower energy portion of the experimental spectra. This was identified to be background noise in the SBD, and it is expected to be mitigated with a forthcoming, improved electron and proton peak identification analysis. It is important to note that this noise, present in both spectra, would cancel in the epγ/ep ratio.

Figures 4.5 and 4.6 are plots of the electron energy spectra under ep and BGO epγ cuts. In general, agreement is very good, although there is a slight disagreement apparent in the ep spectra. This difference is likely due to inaccurate modeling of electron backscattering. It is important to note that low levels of inaccurate modeling of the electron backscatter should, for the most part, cancel in the epγ/ep ratio.

Figures 4.7 and 4.8 are plots of the proton time-of-flight spectra under ep and BGO epγ cuts. In general, agreement is very good between simulation and experiment. This indicates the the RK4 tracking algorithm and the field simulations are performing well.

Figure 4.9 is a plot of the photon energy spectra from the BGO detectors and Figure
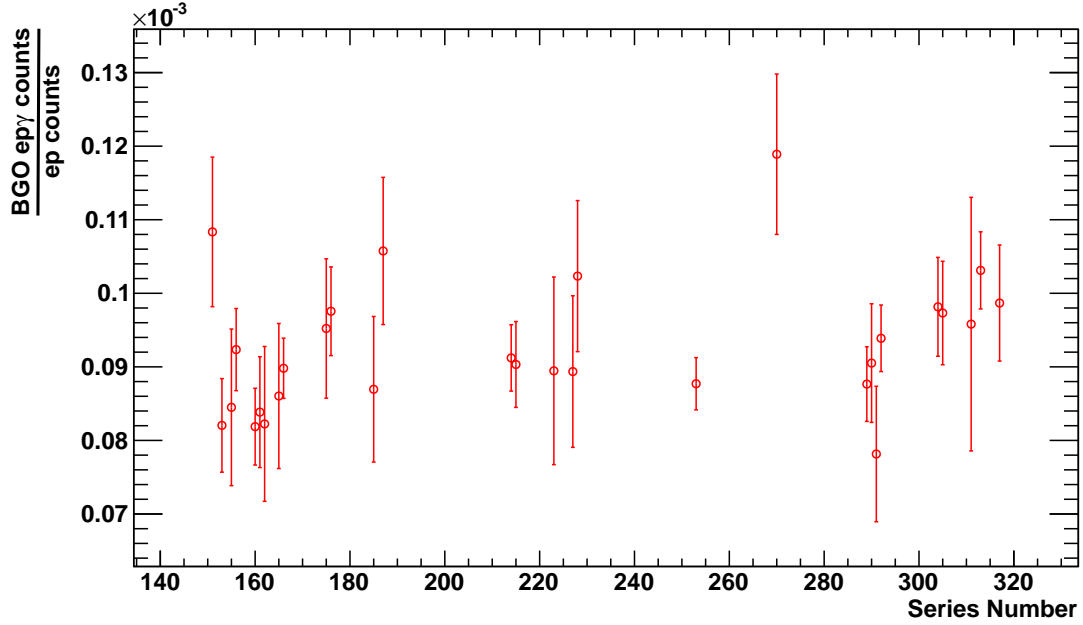
Figure 4.2: Plot of epγ detections per ep detections by series number

4.10 is a plot of the normalized residuals of the two spectra plotted with variable bin size and on a logarithmic calibrated peak height scale. The agreement between experiment and simulation is very good and no significant deviations are apparent. The slight "bump" in the spectra seen at a peak height of ≈70 is caused by bismuth x-rays from nearby BGO crystals.

Figure 4.11 is a plot of the photon energy spectra from the LAAPD detectors and Figure 4.12 is a plot of the normalized residuals of the two spectra. The agreement between experiment and theory is reasonable, except for the region near 5.9 keV, which is the location of the ^{55}Fe peak. This could be an issue with the background subtraction that has yet to be identified as the final LAAPD analysis is still underway. It should be noted that systematic uncertainty for the LAAPD detectors (not shown) is large compared to the statistical uncertainty in the LAAPD energy response (see Section 4.3).
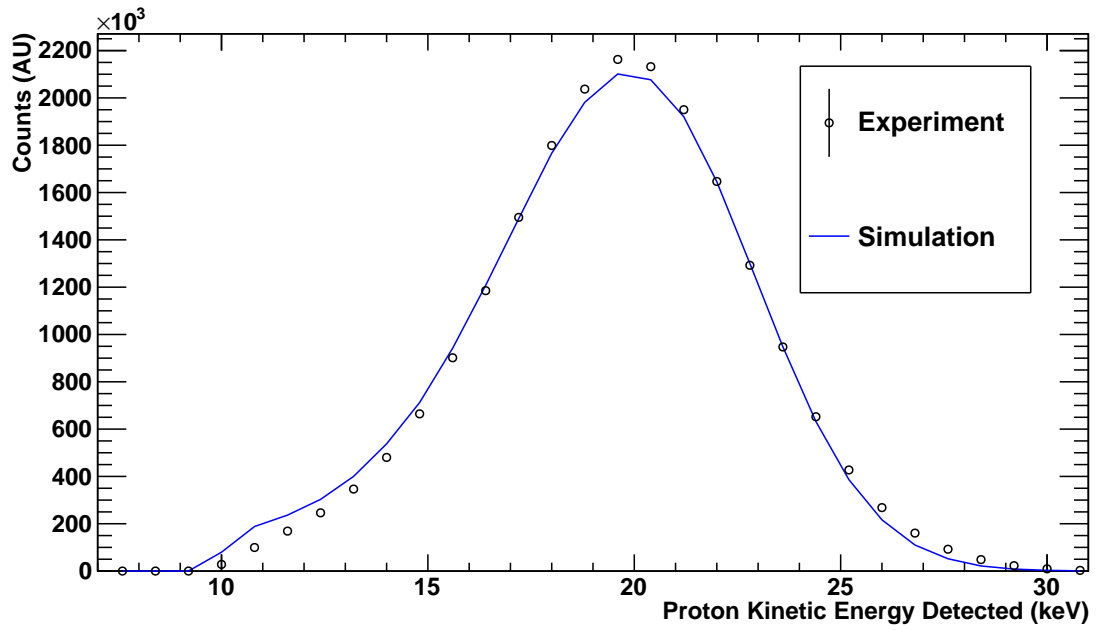
Figure 4.3: Plot of the proton peak height spectra in eр coincidence for both experimental and simulated data. The statistical error on the experimental data is too small to see.
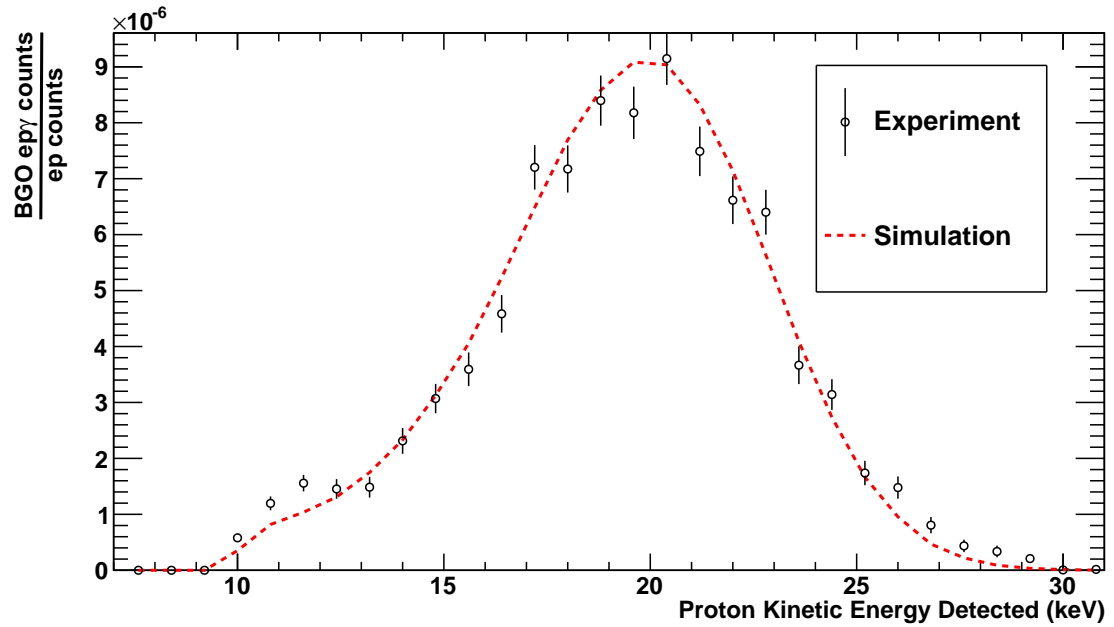
Figure 4.4: Plot of the proton peak height spectra in eрγ coincidence for the average of the BGO detectors for both experimental and simulated data. The experimental data's statistical error is shown.
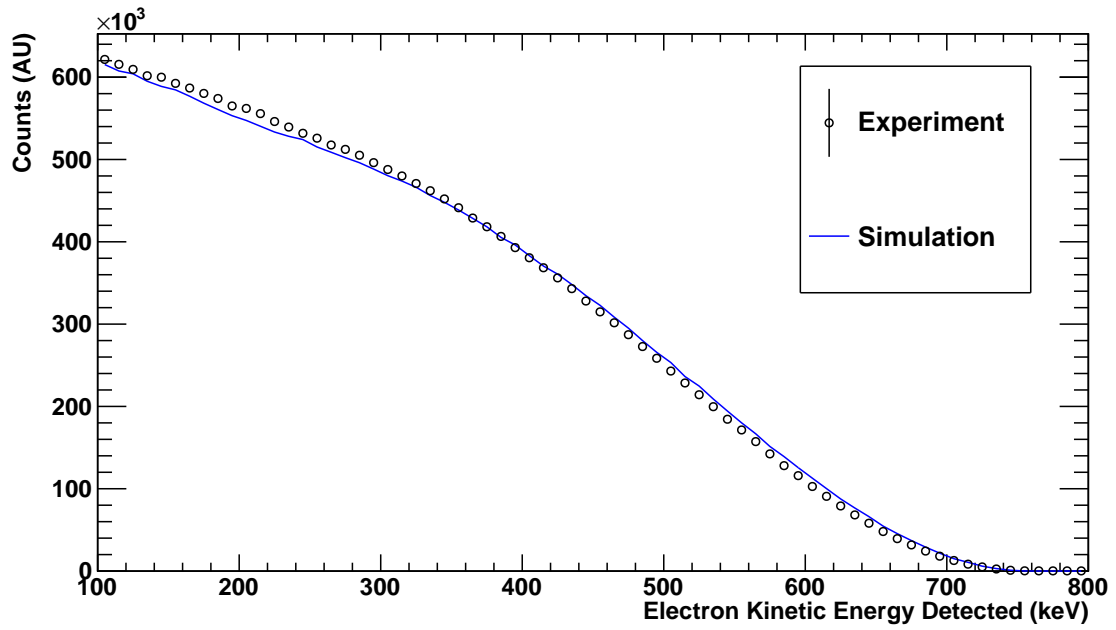
Figure 4.5: Plot of the electron peak height spectra in ep coincidence for both experimental and simulated data. The statistical error on the experimental data is too small to see.
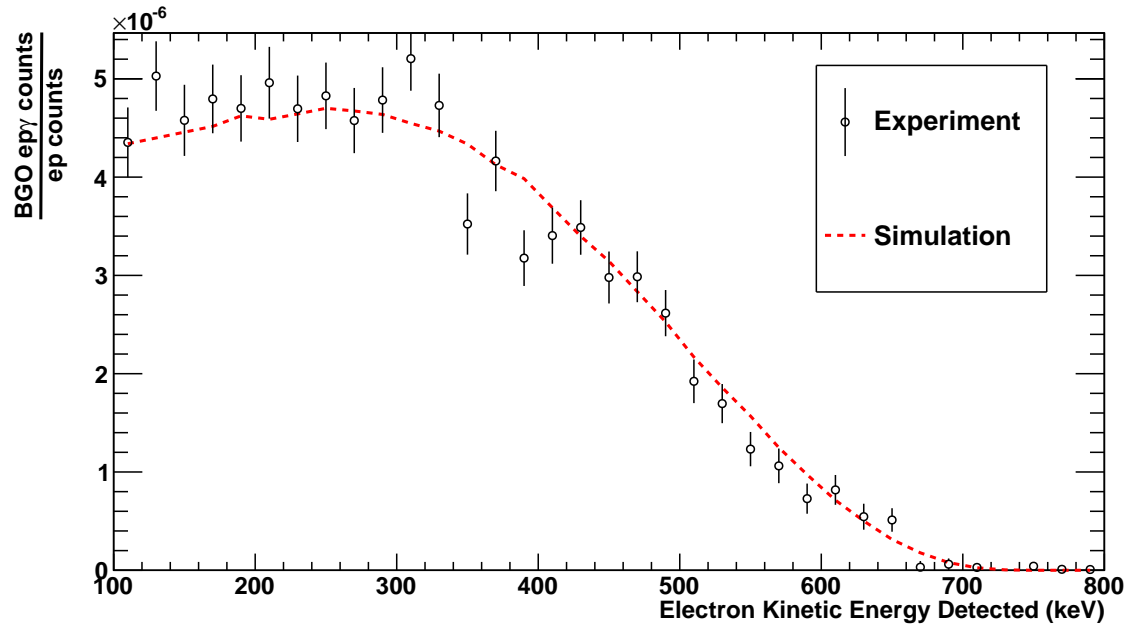
Figure 4.6: Plot of the electron peak height spectra in epγ coincidence for the average of the BGO detectors for both experimental and simulated data. The experimental data's statistical error is shown.
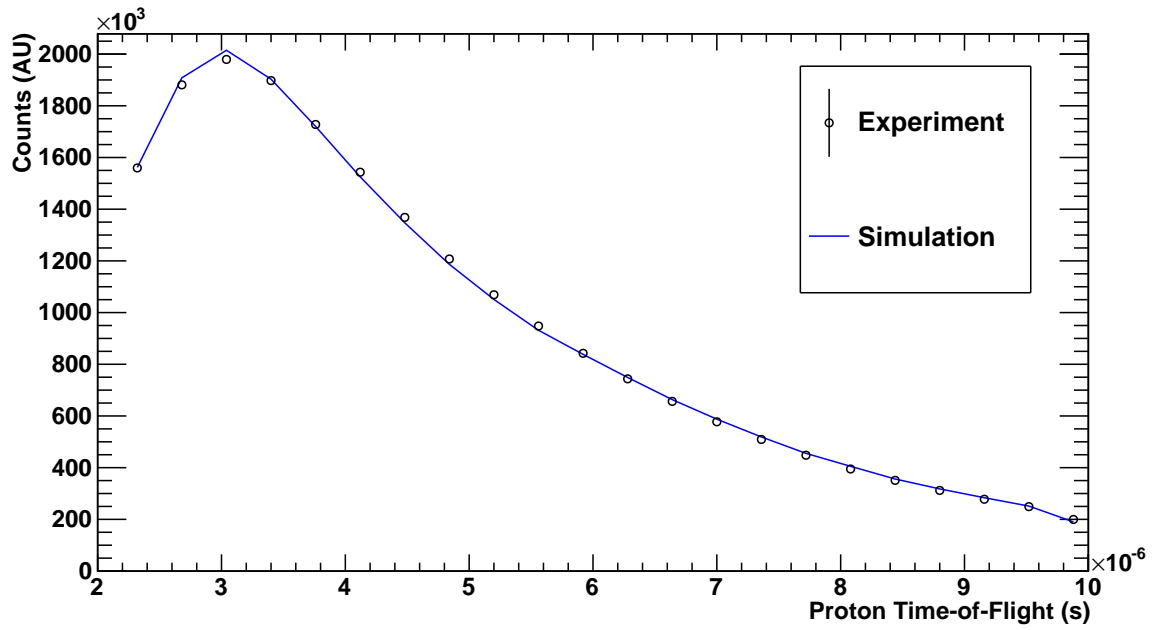
Figure 4.7: Plot of the proton time-of-flight spectra in ep coincidence for both experimental and simulated data. The statistical error on the experimental data is too small to see.
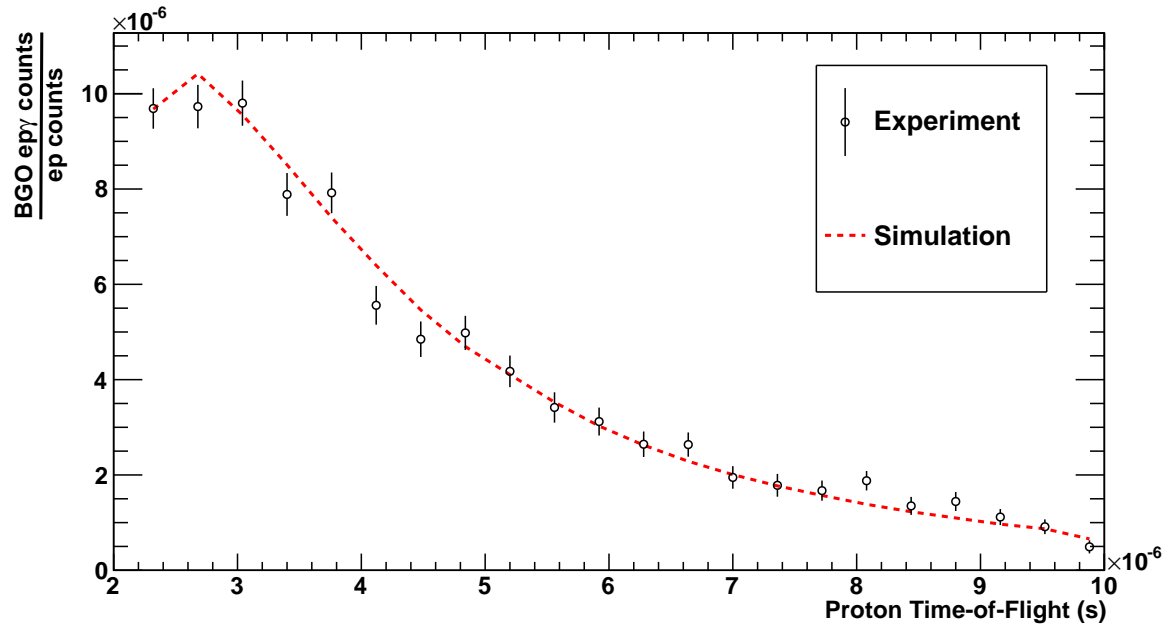
Figure 4.8: Plot of the proton time-of-flight spectra in epγ coincidence for the average of the BGO detectors for both experimental and simulated data. The experimental data's statistical error is shown.
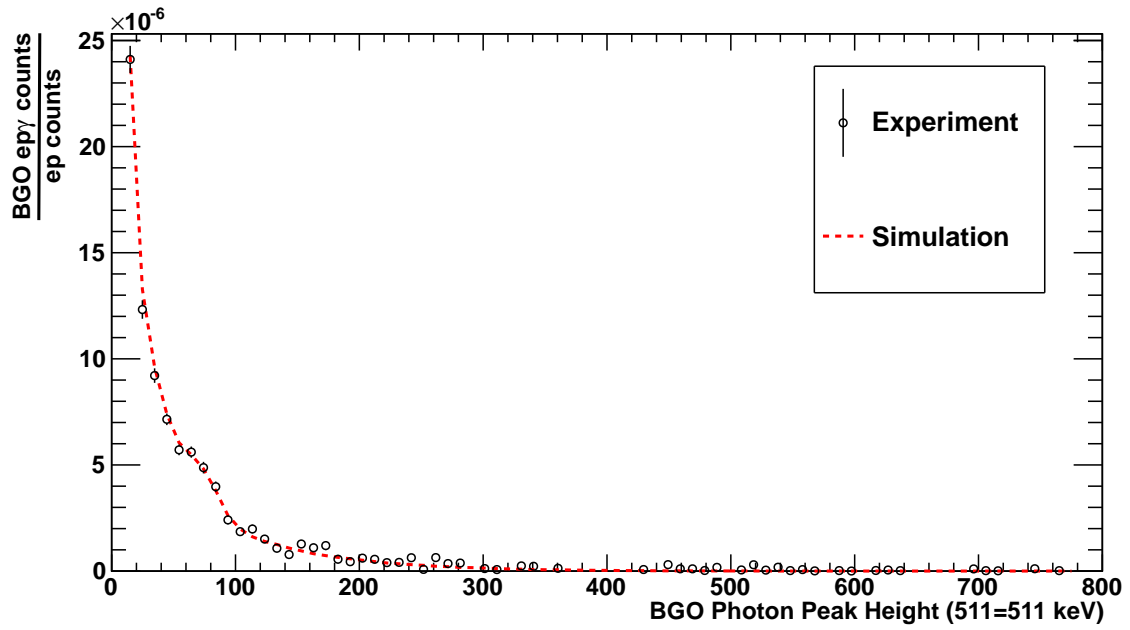
Figure 4.9: Plot of the photon peak height spectra for the average of the BGO detectors for both experimental and simulated data. The experimental data's statistical error is shown.
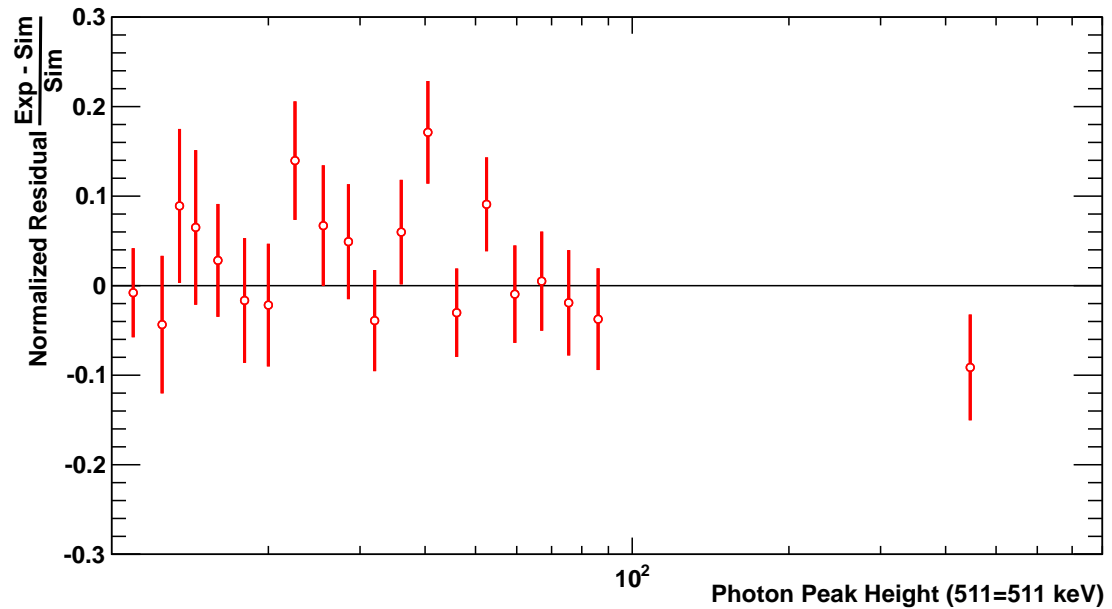
Figure 4.10: Plot of the normalized residuals for the photon peak height spectra for the average of the BGO detectors for the experimental data relative to the simulated data ($\frac{Exp-Sim}{Sim}$). Only statistical error is included.
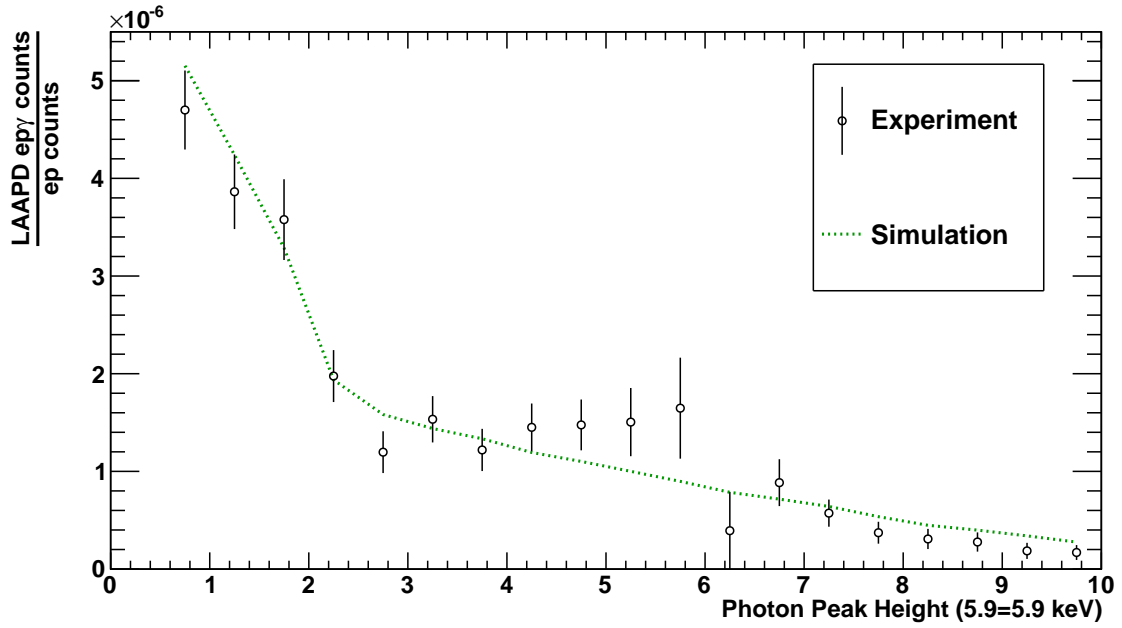
Figure 4.11: Plot of the photon peak height spectra for the average of the LAAPD detectors for both experimental and simulated data. The experimental data's statistical error is shown.
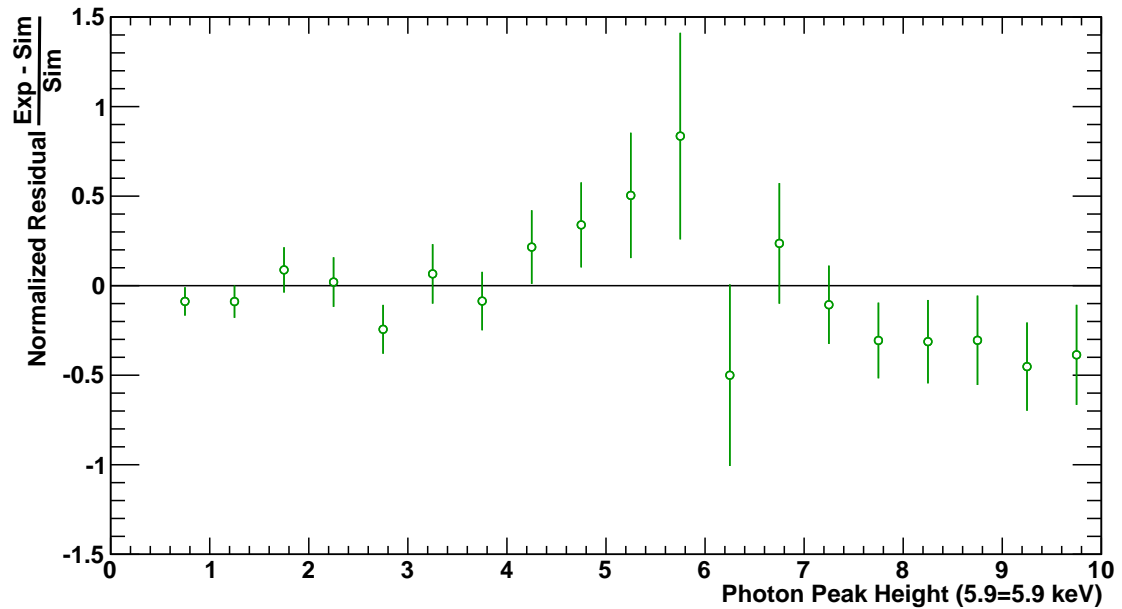
Figure 4.12: Plot of the normalized residuals for photon peak height spectra for the average of the LAAPD detectors for the experimental data relative to the simulated data ($\frac{Exp-Sim}{Sim}$). Only statistical error is included.

4.3 Systematic Uncertainties and Corrections

All systematic corrections and uncertainties present in the RDK II experiment were calculated with respect to a total measured branching ratio over the detector array's energy range. All were analyzed using the integration technique and the epγ/ep method and are shown in Table 4.2. There were few systematic corrections as every attempt was made to include all relevant effects in the simulation.

4.3.1 Photon Detectors

Sources of uncertainties for the photon detectors were specified to be those that arise from their energy response or from electronic artifacts. "Energy response uncertainty" includes uncertainty in non-proportionality and contributions from the detector's peak height resolution.

For the BGO detectors, the primary source of uncertainty arose from imprecise knowledge of BGO non-proportionality (see Section 2.5.1.2). To estimate the effect of this uncertainty, two envelope models which define the upper (+3%) and lower (-3%) uncertainty of the parametric fit to the non-proportionality were created: one envelope for higher non-proportionality and one envelope for less non-proportionality (see Figure 4.13). These three energy response models were then applied to the simulated data, and an uncertainty of $\pm1.8\%$ was calculated from their difference. Additional uncertainties in the BGO detectors' energy resolution and light collection were also assessed.

For the LAAPD detectors, the energy response uncertainty was estimated based on the differences seen in charge collection efficiency model fits (see Section 2.6.2) between the continuous spectra observed at SURF and the monochromator measurements performed at the NSLS. The maximal difference observed was $\pm10\%$ and this was estimated to be the uncertainty in the LAAPD energy response.

Photon electronic artifacts were not yet analyzed by the collaboration in time for this dissertation's publication. They will be identified based on a goodness-of-fit tests of the experimental data with a template photon peak. It is estimated that they will contribute less than $\pm1\%$ to the uncertainty analysis.

4.3.2 SBD Detector

Final SBD systematic correction and uncertainty analysis is expected to include corrections and uncertainties from electronic artifacts as well as investigations of the certainty of energy and timing cuts applied in the analysis.

Source of Uncertainty	BGO Corrections	BGO Uncertainties	LAAPD Corrections	LAAPD Uncertainties
Photon Detector				
Energy response	0%*	2.1%	0%*	10.0%
Electronic artifacts	tbd.	tbd.	tbd.	tbd.
SBD Detector				
Electronic artifacts	tbd.	tbd.	tbd.	tbd.
Electron energy thresholds	tbd.	tbd.	tbd.	tbd.
Proton energy thresholds	tbd.	tbd.	tbd.	tbd.
Electron-proton timing	tbd.	tbd.	tbd.	tbd.
Electron-photon timing	tbd.	tbd.	tbd.	tbd.
Correlated Photon Backgrounds				
Electron bremsstrahlung	-1.0%	0.1%	tbd.	tbd.
Model Uncertainties				
Photon detectors/mirror registration	0%*	tbd.	0%*	tbd.
SBD registration	0%*	2.6%	0%*	2.6%
Beam registration	0%*	1.6%	0%*	4.5%
Magnetic field registration	0%*	1.0%	0%*	2.4%
LAAPD bias leakage voltage	0%*	0%*	0%*	0%*
Electron backscattering	0%*	0%*	0%*	0%*
Monte Carlo statistics	0%*	0%*	0%*	0%*
Extraction method	0%*	tbd.	0%*	tbd.
Total Systematic	**-1.0%**	**3.9%**	**X%**	**11.7%**

Table 4.2: Preliminary summary of the systematic effects that contributed corrections and uncertainties to the measured branching ratio. All percentages represent the 68% level of confidence. "0%*" indicates that the systematic corrections or uncertainties are less than 0.05% in magnitude, but may not be identically zero. A number of corrections and uncertainties are to be determined by the collaboration; these are indicated by "tbd."
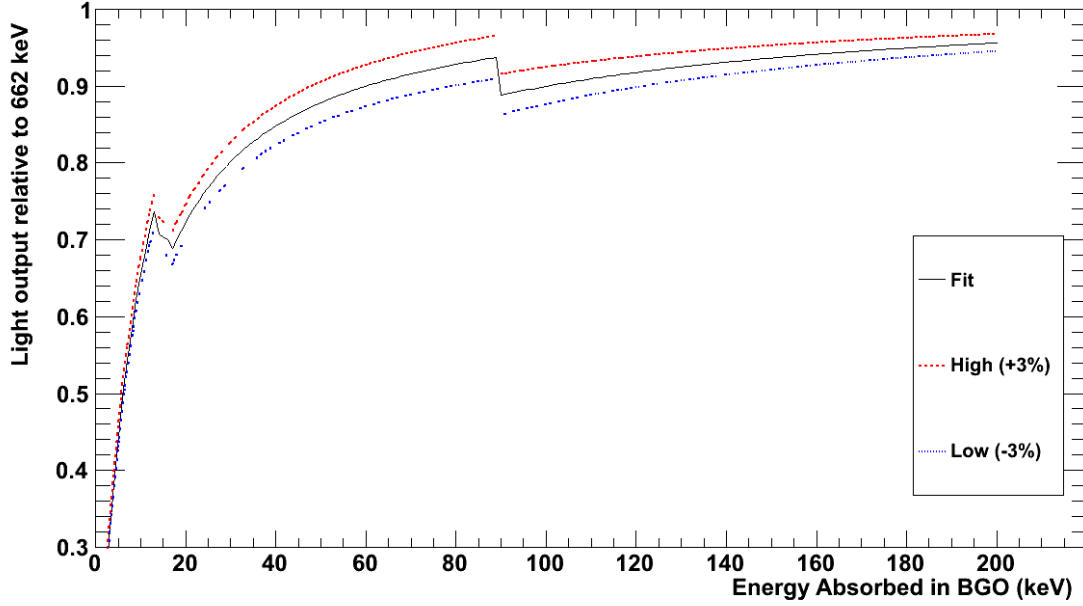
Figure 4.13: Plot of the parametric fit to the experimental BGO non-proportionality data in Figure 2.12 used in the MC simulation and the two envelope models that were also analyzed to determine the effect of its uncertainty.

Uncertainties in electron and proton energy thresholds as well as electron-proton and electron-photon timing were not yet analyzed by the collaboration in time for this dissertation's publication. They will be calculated by varying the thresholds of the cuts described in Table 4.1 when applied to the experimental analysis. The level at which the cuts will be altered will be based on uncertainties inherent to the detector response and the DAQ system. The variance in the epγ/ep ratio resulting from varying these cuts will be used to determine the uncertainties. These uncertainties are expected to contribute less than $\pm1\%$ to the uncertainty analysis.

Electron and proton electronic artifacts were not yet analyzed by the collaboration in time for this dissertation's publication. They will be identified based on a goodness-of-fit tests of the experimental data with a templates of electron and proton peaks. The methodology to determine uncertainties from these has yet to be determined. These uncertainties are expected to contribute less than $\pm1\%$ to the uncertainty analysis.

4.3.3   Correlated Photon Backgrounds

Sources of correlated photon backgrounds, those that will fall preferentially within the on-peak window in the electron-photon timing spectrum, were not suppressed by the epγ/ep

ratio method. Electron bremsstrahlung was the largest source of correlated background. Electrons that entered the SBD deposited some of their kinetic energy while they produced outer bremsstrahlung photons. These photons then could strike the photon detectors and produce an epγ coincidence which did not originate from radiative decay. For the most part, the RDK II photon detectors were shielded from this, however some BGO crystals did have a small solid angle exposed to the SBD surface. The systematic correction and uncertainty, -1.0%±0.1%, was estimated from Geant4 MC simulations of three body events.

4.3.4   Model Uncertainties

The uncertainties in the MC simulation of the apparatus included spatial registration (positional) uncertainties of various components, the precense of an unintended electric potential from the LAAPDs, electron backscattering uncertainties, MC statistics, and the extraction methodology.

The registration uncertainties were presumed to be on the level of ±1 mm and were simulated in both the correct position and the displaced positions in Geant4. The SBD's positional uncertainty in the direction of the magnetic field was found to be ±2 mm due to uncertainty in the amount of length contraction which occurred its mounting apparatus.

The results of the simulations showed that the registration uncertainties that altered the SBD's detection efficiency of electrons and protons that originated from decays occurring at the magnetic field bend were the most significant. These registration uncertainties were from SBD registration uncertainty (±2.6%) and beam registration uncertainty (±1.6%). The uncertainty in the magnetic field registration (±1.0%) did not alter the path of particles which originated from the bend, and thus was smaller. Photon detectors/mirror registration uncertainty analysis was not complete in time for publication of this dissertation, but is expected to be on the order of ±1.0%.

The bias voltage leakage of the second version of the LAAPD array was simulated using COMSOL Mutiphysics®. It was found that this field did not significantly contribute to the uncertainty (see Sections 2.3 and 3.3).

Uncertainty in the simulation's modeling of electron backscattering was investigated by simulating scattering with both a single-scattering and a multi-scattering algorithms (see Section 3.6). The difference between the results of these two methods did not significanty differ when the epγ/ep ratio was investigated .

Statistical uncertainty in the simulated model was not significant as the Flux high performance computing (HPC) Cluster at the University of Michigan was utilized to simulate over a fifty million three-body and four-body events.

The uncertainty in the branching ratio extraction method is the difference between using the integration technique and the fit technique. These extraction techniques were described in Section 4.2. This uncertainty will not be evaluated until the final analysis has been complete. It is expected to be less than $\pm 1.0\%$.

CHAPTER 5

Conclusion

The results of the RDK II experiment are addressed in this chapter. First, the preliminary data is discussed in relation to QED theory. Then future experiments related to RDK II and radiative beta decay are covered.

5.1 RDK II Results

The final data analysis for the radiative beta decay of the free neutron unfortunately could not be completed by the RDK II collaboration in time to be discussed in this dissertation. It is possible to state that preliminary data analysis indicates that the experimental branching ratio measured will be within 10% of its predicted QED value for both the BGO and LAAPD detectors. In addition, the shape of the QED photon spectrum simulated in the RDK II apparatus (see Figures 4.9, 4.10, 4.11, and 4.12) shows good agreement with the experimental data for both detector arrays.

The systematic error analysis, while incomplete, indicates that the BGO detectors will have an uncertainty on the level of $\approx$4% while the LAAPD detectors will have a uncertainty on the level of $\approx$12%. The statistical uncertainties for the BGO and LAAPD detectors will be $\approx$2% and $\approx$3% respectively.

RDK II's measurement will be the second measurement of radiative free neutron decay, and it will be the most precise measurement. While the uncertainty level is insufficient to test proposed new physical theories beyond QED (see Section 5.3) it is nevertheless still important to test even "the most successful" of theories, particularly in relatively simple systems.

5.2   Neutron Beam Lifetime

RDK II also makes two contributions towards resolving the puzzling discrepancies seen between neutron lifetime measurements made with cold neutron beams and those measured from UCNs trapped in bottles (see Figure 5.1). First, as was previously discussed in Section 1.3.1, radiative corrections affect the decay rate of the neutron at the ≈4% level. Any deviations from QED theory could alter the extraction of V_{ud} from the neutron lifetime and make comparisons to other systems invalid. Confirming that the neutron's radiative decay mode matches with QED theory strengthens confidence in these corrections.

The second contribution is of a more practical nature. An experimental collaboration was formed to perform a beam lifetime measurement at the ≈0.1% uncertainty level [102]. This experiment will take place on the NG-6 beamline at the NCNR and will utilize the same solenoid system utilized in RDK II and previous neutron beam measurements at NIST. Principally, the photon detectors and electrostatic mirror will be removed and replaced with a precision-machined multi-electrode trap. The electrodes will trap individual protons from neutron decay, while allowing electrons to escape undetected. Each proton will travel in a helical orbit towards a silicon detector after it is released from the trap. Due to the significant overlap in functionality, many of the lessons learned during the operation and analysis of RDK II can be applied to the beam measurement. In particular, the Geant4 charged particle simulation code used in RDK II can be applied to calculate proton trapping dynamics and their subsequent detection. This will benefit the exploration and understanding of the systematic uncertainties associated with beam measurement.
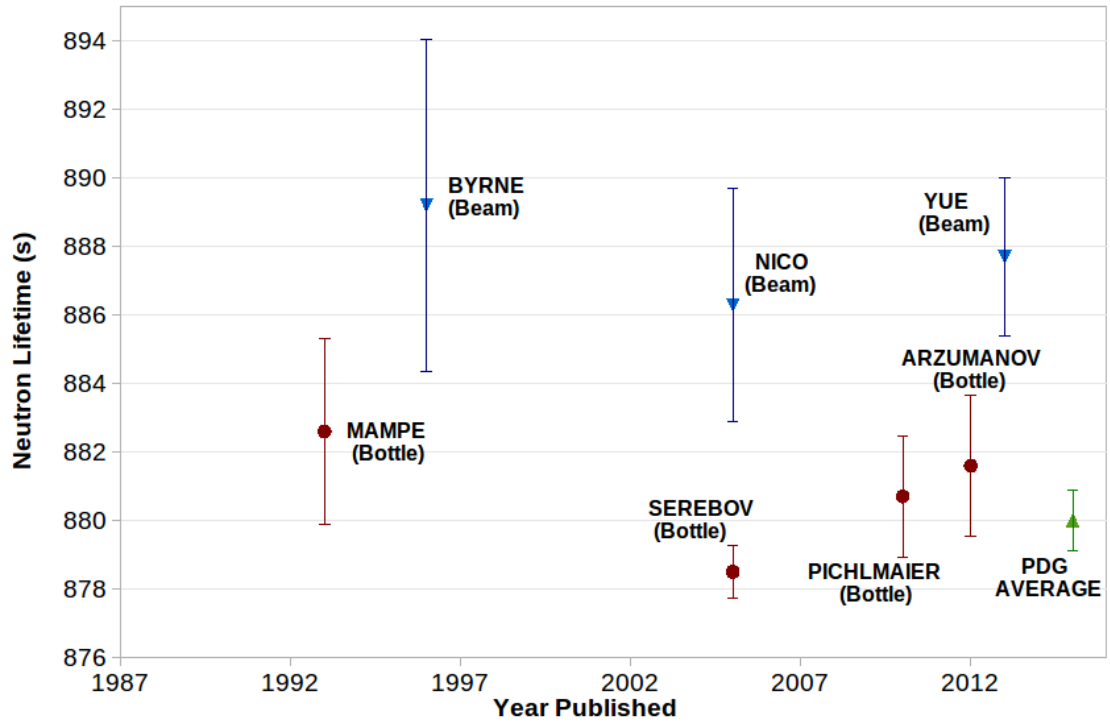
Figure 5.1: Plot of the neutron lifetime measurements [54, 103–107] included in the PDG average [20] and a recent recalculation of the most recent beam measurement by Yue et al. [39] which will supercede the Nico et. al. [54] value. After replacing the Nico et. al. measurement with the Yue et al. measurement, there is currently a 3.8σ discrepancy between cold neutron beam measurements and UCN bottle measurements of the neutron lifetime [39].

5.3   Future Radiative Decay Experiments

The goal of any future experiment that measures radiative neutron decay should be well defined. At this juncture, radiative neutron beta decay appears to be consistent with QED theory at the current experimental precision and in the energy ranges measured. One avenue of investigation would be to simply perform an additional measurement in the RDK II energy ranges with even higher precision. Within the SM, measurements would have to approach sub 1% precision in order to measure contributions from inner-bremsstrahlung. This would be challenging to perform with the RDK II apparatus as registration uncertainties that relate to the magnetic field bend and the performance of BGO crystals and LAAPDs would be difficult to reduce.

There are few significant changes that could be madeto reduce the uncertainty associated with positional registration. First, the detection apparatus could be designed from the ground up to be precision-machined. After manufacturing the detection apparatus could then be measured by a metrology laboratory. This could also include adjustable stages to precisely adjust the detectors' positions and measure the systematic effects of any such variations. An adjustable stage of this nature is being designed for the silicon detector used in the NIST beam neutron lifetime experiment. Another improvement to positional registration would be to increase the area of the SBD. This would degrade the SBD's energy resolution, but this effect would likely be manageable. Finally it might be possible to add additional electrodes in the active detection region to serve as mirrors to protons. This would provide greater understanding of the ep coincidence detection sensitivities. As discussed, there is a precision, segmented electrode system that will be used in the NIST beam neutron lifetime experiment, but the system would not be compatible with the current BGO detector array. It might be possible to use the electrode system with a detector array mounted in a similar fashion as the LAAPD array.

A possible replacement for BGO detectors would be to use high purity germanium (HPGe) detectors. A HPGe detector is similar in design to a SBD or an APD as it is a semiconductor detector doped in the pin configuration. The advantage of HPGe is that pure thick germanium crystals can be formed, which allows for greater depletion depths than silicon. This means that thicker detectors can be formed to detect high energy photons. HPGe detectors can easily detect photons in the energy range of 5.9 keV to 781 keV with a resolution of $\approx$200 eV and 2 keV respectively [108], which is far superior to BGO detectors. Germanium, unlike BGO scintillators, is also highly linear, even near its K and L edges [109]. The disadvantage of HPGe detectors is that germanium has a very small band gap energy (0.74 eV) and therefore necessitates that it be at or near liquid nitrogen tem-

peratures (77 K) to operate at reasonable noise levels. Like the LAAPD detectors, HPGe detectors are sensitive to high magnetic fields, but this can be minimized by choosing a direction such that the charge flow is parallel to the magnetic field [110]. As germanium is less dense than BGO, the detectors would have to be ≈30% thicker to absorb the same amount of photons in the upper energy range of radiative decay. This, along with any active cooling needed, make placing HPGe detectors in the existing RDK II solenoids difficult. Again, perhaps the most attractive option would be an array similar to the LAAPD array. This would provide sufficient room behind the detectors to establish cooling.

A future experiment could also investigate the Dirac structure of the weak current by measuring the polarization of radiative decay from polarized neutrons [7–9]. This would require both a source of polarized neutrons and a method of detecting their polarization. For polarized cold neutrons, there are two primary methods of generating them: either with a super mirror or with polarized ^{3}He [111]. While polarized cold neutron production is relatively straightforward, efficiently detecting polarized photons at the keV energy scale is exceedingly difficult.

Furthermore, improved statistics at higher radiative photon energies would test a possible source of time-reversal violation through the triple correlation $\mathbf{l_p} \cdot (\mathbf{l_e} \times \mathbf{k})$, where $\mathbf{l_p}$ and $\mathbf{l_e}$ are the proton and electron momenta, respectively, and $\mathbf{k}$ is the photon momentum [10, 11]. This would require significant improvements in the statistics in the high energy region and the capability of capturing the direction of emission of the proton, electron, and photon. One way of doing so would be to take a duplicate version of the RDK II solenoid system and place it on a cold neutron beam such that the SBD detectors can detect electrons going in either direction. This would also provide for detection of any backscattered electrons, eliminating any systematic corrections that they would introduce. Conveniently, a duplicate solenoid system already exists and currently is unused [104]. This "double" RDK II design would increase the active detection region by a factor of two and would double the number of electrons detected per unit length. Furthermore, the solid angle of photon detection is increased, particularly for detectors in a configuration similar to the LAAPD, guaranteeing greater than a factor of four improvement in epγ detection rate. A diagram of a concept system which uses both solenoid sets, as well as HPGe detectors and an electrode system, can be found in Figure 5.2.

Perhaps the best future for radiative neutron decay experiments would be in conjunction with other neutron decay experiments that measure the correlation coefficients that were discussed in Section 1.3.2. For example, measurements of the electron-antineutrino correlation (a) using an asymmetry approach require the detection of an electron as well as a proton [112, 113]. In future experimental efforts, the only additional component that
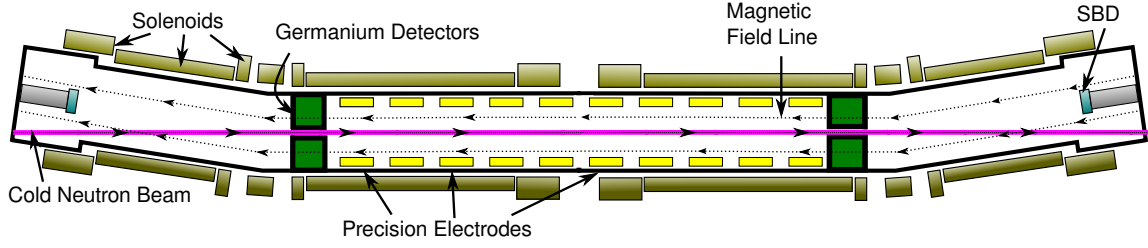
Figure 5.2: Diagram of a "double RDK" concept to measure radiative photon decay. In this concept, two RDK II solenoids and two SBDs are used in conjunction with precision-machined electrodes to restrict the active region and germanium detectors to measure radiative photons.

would need to be added to the design would be the photon detectors and a DAQ system to record the events.

5.4 Fierz Interference

One future avenue of research that uses the preexisting RDK II experimental data would be to investigate the Fierz interference term (b) in the free neutron. As explained in Chapter 1, the Fierz term should be zero in the standard model, as it arises from scalar or tensor couplings, which are not known to be present in weak decay. It has been measured to be consistent with zero, +0.0001±0.0026, in super allowed ($0^+ \rightarrow 0^+$) decays [114]. Recent efforts to directly measure this in the free neutron have set a limit of $|b| < 0.13$ (90% C.L.) [115] and a planned experiment, Nab, will measure both the Fierz term as well as the electron-antineutrino correlation term [113]. As can be extrapolated from Eq. (1.8), the Fierz term will directly affect the electron spectrum originating from neutron decay. Figure 5.3 emphasizes the small effect b has on the electron spectrum.

RDK II's electron spectrum contains sufficient statistics to consider measuring the Fierz interference term using the preexisting data. This was investigated early on during the data analysis, but concerns over the effect of imprecise modeling of electron backscattering by Geant4 and other simulation packages arose [81]. Further efforts to extract a Fierz term were put on hold to focus on the completion of radiative neutron decay measurements. With the radiative measurements nearing completion, it would be possible again to examine whether a Fierz term extraction with RDK II data was possible.
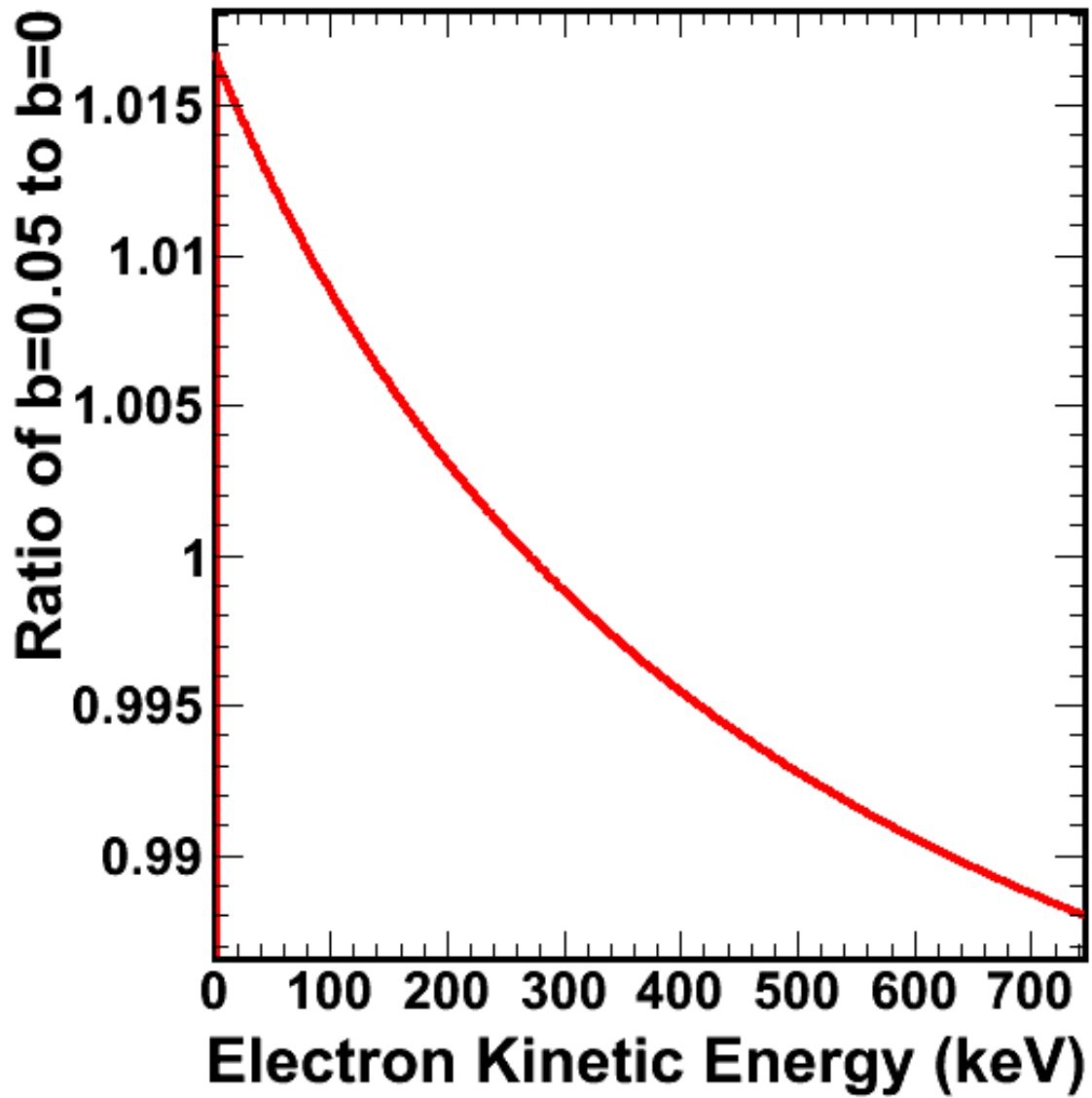
Figure 5.3: Plot of the effect of a non-zero Fierz interference ($b = 0.05$) term on the electron spectrum compared to no Fierz interference.

APPENDIX A

Radiative Decay Formula

The following formula is used in place of Eq. (1.10) in the four body event generator in the RDK II simulation.

$$
\frac{d\Gamma_{ep\gamma}}{dE_\gamma d\phi_\gamma d(\cos\theta_\gamma) dE_e d\phi_e d(\cos\theta_e) d\phi_\eta d(\cos\theta_\eta)} =
$$

$$
\frac{\alpha g_v^2}{\pi_4 \hbar}(E_{e_{max}} - E_{e_{min}})(E_{\gamma_{max}} - E_{\gamma_{min}})\left(2\pi\alpha\frac{E_e}{E_p(1. - e^{-2\pi\alpha\frac{E_e}{E_p}})}\left(\frac{E_p E_\gamma E_\eta}{2}\right)\right)
$$

$$
\left(2(1+\lambda^2)\left(\frac{E_\eta\big((E_e + E_\gamma)m_e{}^2 - E_\gamma(\mathbf{p}_e \cdot \mathbf{k})\big)}{(\mathbf{p}_e \cdot \mathbf{k})^2} + \frac{E_\eta E_e m_p{}^2}{(\mathbf{p}_p \cdot \mathbf{k})^2}\right.\right.
$$

$$
\left.- \frac{E_\eta(E_e(\mathbf{p}_p \cdot \mathbf{k}) - (E_p)(\mathbf{p}_e \cdot \mathbf{k}) + (2E_e + E_\gamma)(\mathbf{p}_p \cdot \mathbf{p}_e)}{(\mathbf{p}_e \cdot \mathbf{k})(\mathbf{p}_p \cdot \mathbf{k})}\right)
$$

$$
-(1-\lambda^2)\left(\frac{m_e{}^2\big((\mathbf{p}_e \cdot \eta) + (\eta \cdot \mathbf{k})\big) - (\mathbf{p}_e \cdot \mathbf{k})(\eta \cdot \mathbf{k})}{(\mathbf{p}_e \cdot \mathbf{k})^2}\right.
$$

$$
\left.\left.+ \frac{m_p{}^2(\mathbf{p}_e \cdot \eta)}{(\mathbf{p}_p \cdot \mathbf{k})^2} - \frac{(\mathbf{p}_e \cdot \eta)(\mathbf{p}_p \cdot \mathbf{k}) - (\mathbf{p}_p \cdot \eta)(\mathbf{p}_e \cdot \mathbf{k}) + \big(2(\mathbf{p}_e \cdot \eta) + (\eta \cdot \mathbf{k})\big)(\mathbf{p}_p \cdot \mathbf{p}_e)}{(\mathbf{p}_e \cdot \mathbf{k})(\mathbf{p}_p \cdot \mathbf{k})}\right)\right)
$$

$$
\text{(A.1)}
$$

APPENDIX B

Simulation Geometry

The geometry in the RDK II apparatus was simplified in the Geant4 model to use only the C++ classes: *G4Tubs*, which formed cylinders and rings, and *G4Box*, which formed boxes. Holes were made in objects appropriately using boolean subtraction (*G4SubtractionSolid*). Tables B.1, B.3, B.2, and B.4 contain the parameters used in the Geant4 model before length contraction. Length contraction was accounted for separately in the Geant4 simulation code.

Part Name	Material	Inner Radius	Outer Radius	z_0	z_F	Length	Center Along z	Offset x Dir.	Offset y Dir.
Straight Bore	Stainless Steel	5.85	6.11	45.28	0.00	45.28	22.64	0.00	0.00
High Voltage Tube	Aluminum	2.38	2.54	34.72	32.72	2.00	33.72	0.00	0.00
Front Nylon Spacer	Nylon	2.38	2.54	32.72	32.40	0.32	32.56	0.00	0.00
Large Nylon Spacer	Nylon	2.54	2.86	38.91	32.40	6.51	35.66	0.00	0.00
Main Ground Cylinder	Aluminum	2.86	3.18	45.10	32.40	12.70	38.75	0.00	0.00
Front Mirror Ground	Aluminum	2.54	3.18	32.40	32.24	0.16	32.32	0.00	0.00
Outer Mirror Ground	Aluminum	3.18	5.24	36.21	35.57	0.64	35.89	0.00	0.00
Downstream Nylon Spider	Nylon	3.81	5.40	35.57	33.67	1.90	34.62	0.00	0.00
G10 APD Holder	G10	3.49	5.40	33.67	32.40	1.27	33.04	0.00	0.00
Throwing Star 1	Aluminum	3.49	4.95	32.40	31.77	0.64	32.08	0.00	0.00
Aluminum Heat Shield	Aluminum	4.95	5.12	32.40	12.09	20.32	22.24	0.00	0.00
Throwing Star 2	Aluminum	3.49	4.95	12.72	12.09	0.64	12.40	0.00	0.00
Nylon Pusher Assembly	Nylon	3.49	5.40	12.08	9.38	2.70	10.73	0.00	0.00
Upstream Aluminum Tape 1	Aluminum	3.46	3.49	12.08	9.38	2.70	10.73	0.00	0.00
Upstream Aluminum Tape 2	Aluminum	3.49	3.81	9.38	9.35	0.03	9.36	0.00	0.00
Upstream Nylon Spider	Nylon	3.81	5.40	9.38	7.48	1.91	8.43	0.00	0.00
Upstream Aluminum Tape 3	Aluminum	3.78	3.81	9.35	7.88	1.47	8.61	0.00	0.00
BAPD Holder	Aluminum	1.75	5.50	4.10	3.78	0.32	3.94	0.00	0.00
Front Copper On Aperture	Copper	2.38	5.73	2.72	2.54	0.18	2.63	0.00	0.00
Lead Aperture	Lead	2.54	5.73	2.54	0.00	2.54	1.27	0.00	0.00
Inner Copper On Aperture	Copper	2.38	2.54	2.54	0.00	2.54	1.27	0.00	0.00
Upstream Support Rod 1	Aluminum	0.00	0.24	12.72	2.82	9.90	7.77	3.97	2.29
Upstream Support Rod 2	Aluminum	0.00	0.24	12.72	2.82	9.90	7.77	0.00	-4.59
Upstream Support Rod 3	Aluminum	0.00	0.24	12.72	2.82	9.90	7.77	-3.97	2.29
Hex Support Rod 1	Aluminum	0.00	0.33	31.77	12.72	19.05	22.24	3.97	2.29
Hex Support Rod 2	Aluminum	0.00	0.33	31.77	12.72	19.05	22.24	0.00	-4.59
Hex Support Rod 3	Aluminum	0.00	0.33	31.77	12.72	19.05	22.24	-3.97	2.29
Downstream Support Rod 1	Aluminum	0.00	0.24	37.70	31.77	3.81	33.67	3.97	2.29
Downstream Support Rod 2	Aluminum	0.00	0.24	37.70	31.77	3.81	33.67	0.00	-4.59

Part Name	Material	Inner Radius	Outer Radius	z_0	z_F	Length	Center Along z	Offset x Dir.	Offset y Dir.
Downstream Support Rod 3	Aluminum	0.00	0.24	37.70	31.77	3.81	33.67	-3.97	2.29
Long Adjustment Rod 1	Stainless Steel	0.00	0.24	44.70	8.43	36.27	26.56	0.00	4.59
Long Adjustment Rod 2	Stainless Steel	0.00	0.24	44.70	8.43	36.27	26.56	3.97	-2.29
Long Adjustment Rod 3	Stainless Steel	0.00	0.24	44.70	8.43	36.27	26.56	-3.97	-2.29
Short Adjustment Rod 1	Stainless Steel	0.00	0.24	44.70	34.62	10.08	39.66	4.59	0.00
Short Adjustment Rod 2	Stainless Steel	0.00	0.24	44.70	34.62	10.08	39.66	-2.29	-3.97
Short Adjustment Rod 3	Stainless Steel	0.00	0.24	44.70	34.62	10.08	39.66	-2.29	3.97
Magnet Coil 1	Copper	7.00	8.28	42.40	36.40	6.00	39.40	0.00	0.00
Magnet Coil 2	Copper	8.32	10.29	42.40	36.40	6.00	39.40	0.00	0.00
Magnet Coil 3	Copper	7.00	7.89	35.90	5.90	30.00	20.90	0.00	0.00
Magnet Coil 4	Copper	7.91	8.96	35.90	5.90	30.00	20.90	0.00	0.00
Magnet Coil 5	Copper	7.00	7.57	5.40	3.90	1.50	4.65	0.00	0.00
Magnet Coil 6	Copper	7.61	9.28	5.40	3.90	1.50	4.65	0.00	0.00
Magnet Coil 7	Copper	9.32	10.46	5.40	3.90	1.50	4.65	0.00	0.00
Aluminum Plug	Aluminum	0.00	2.06	67.00	62.00	5.00	64.50	0.00	0.00
Far Aluminum Tube	Aluminum	2.06	2.22	73.99	46.05	27.94	60.02	0.00	0.00
DS Cryostat Flange A	Stainless Steel	7.70	13.49	46.23	45.28	0.95	45.75	0.00	0.00
DS Cryostat Flange B	Stainless Steel	0.00	18.75	45.28	44.01	1.27	44.65	-5.72	0.00
Coil Tray 1, Part H	Aluminum	6.35	6.98	43.72	3.08	40.64	23.40	0.00	0.00
Coil Tray 1, Part I	Aluminum	6.98	12.70	43.72	42.40	1.32	43.06	0.00	0.00
Coil Tray 1, Part K	Aluminum	6.98	10.48	36.37	35.90	0.47	36.14	0.00	0.00
Coil Tray 1, Part L	Aluminum	6.98	10.48	5.87	5.40	0.47	5.63	0.00	0.00
Coil Tray 1, Part M	Aluminum	6.98	12.70	3.87	3.08	0.79	3.48	0.00	0.00
Grounding Strap Part 1	Copper	5.12	5.18	31.84	31.55	0.29	31.69	0.00	0.00
Grounding Strap Part 2	Copper	5.12	5.18	29.14	28.85	0.29	28.99	0.00	0.00
Grounding Strap Part 3	Copper	5.12	5.18	26.44	26.15	0.29	26.29	0.00	0.00
Grounding Strap Part 4	Copper	5.12	5.18	23.74	23.44	0.29	23.59	0.00	0.00
Grounding Strap Part 5	Copper	5.12	5.18	21.04	20.74	0.29	20.89	0.00	0.00
Grounding Strap Part 6	Copper	5.12	5.18	18.33	18.04	0.29	18.19	0.00	0.00
Grounding Strap Part 7	Copper	5.12	5.18	15.63	15.34	0.29	15.49	0.00	0.00
Grounding Strap Part 8	Copper	5.12	5.18	12.93	12.64	0.29	12.79	0.00	0.00
Grounding Strap Part 9	Copper	5.40	5.46	34.54	34.25	0.29	34.39	0.00	0.00
Grounding Strap Part 10	Copper	3.50	3.56	37.24	36.95	0.29	37.09	0.00	0.00
Grounding Strap Part 11	Copper	3.50	3.56	39.94	39.65	0.29	39.79	0.00	0.00
Grounding Strap Part 12	Copper	3.50	3.56	42.64	42.35	0.29	42.50	0.00	0.00

Table B.1: Parameters which define the cylinders or rings parallel to z axis. All dimensions of length are in cm.

Part Name	Material	Inner Radius	Outer Radius	z_0	z_F	Length	Center Along z	Offset x Dir.	Offset y Dir.
Bent Bore	Stainless Steel	5.85	6.11	0.00	-26.49	26.49	-13.25	0.00	0.00
Large Bent Bore	Stainless Steel	7.04	7.30	-25.68	-35.84	10.16	-30.76	0.00	0.00
Spacer Ring	Stainless Steel	6.11	7.04	-25.68	-26.49	0.81	-26.09	0.00	0.00
Magnet Coil 9	Copper	7.00	10.76	-3.90	-5.40	1.50	-4.65	0.00	0.00
Magnet Coil 10	Copper	7.00	8.58	-5.90	-23.40	17.50	-14.65	0.00	0.00
Magnet Coil 11	Copper	8.00	10.52	-23.90	-30.65	6.75	-27.28	0.00	0.00
SBD 1.5mm Si	Silicon	0.00	1.38	-27.80	-27.95	0.15	-27.88	0.00	0.00
SBD 1.5mm Si Holder	Al Oxide	1.38	1.75	-27.59	-28.08	0.49	-27.84	0.00	0.00
SBD 1.5mm Gold Coating	Gold	0.00	1.38	-27.80	-27.80	0.00	-27.80	0.00	0.00
SBD Aluminum Coating	Aluminum	0.00	1.38	-27.95	-27.95	0.00	-27.95	0.00	0.00
SBD 1.5 mm Plastic Lining	Acrylic	1.75	1.75	-27.59	-28.14	0.54	-27.87	0.00	0.00

Part Name	Material	Inner Radius	Outer Radius	z_0	z_F	Length	Center Along z	Offset x Dir.	Offset y Dir.
SBD 1.5mm Back Rings	Brass	1.51	1.75	-28.08	-28.11	0.03	-28.10	0.00	0.00
SBD 1.5mm Internal Disc	Brass	0.16	1.75	-28.11	-28.14	0.03	-28.13	0.00	0.00
SBD 1.5mm Spring	Brass	0.03	0.22	-28.14	-28.75	0.61	-28.45	0.00	0.00
SBD 1.5mm Hex Screw	Brass	0.21	0.42	-28.75	-29.19	0.44	-28.97	0.00	0.00
SBD 1.5mm Front Case	Brass	1.51	1.81	-27.52	-27.59	0.07	-27.56	0.00	0.00
SBD 1.5mm Mid Case	Brass	1.75	1.81	-27.59	-28.86	1.27	-28.23	0.00	0.00
SBD 1.5mm Back Case	Brass	0.42	1.81	-28.86	-28.91	0.05	-28.89	0.00	0.00
BeO Tube	Be0	2.89	3.05	-27.52	-45.23	17.71	-36.38	0.00	0.00
SBD 1.5mm Steel Tube	Stainless Steel	1.23	1.27	-29.01	-45.23	16.22	-37.12	0.00	0.00
Coil Tray 2, Part A	Aluminum	6.35	6.98	-3.08	-24.34	21.26	-13.71	0.00	0.00
Coil Tray 2, Part B	Aluminum	7.47	7.98	-23.88	-31.96	8.09	-27.92	0.00	0.00
Coil Tray 2, Part C	Aluminum	6.98	12.70	-3.08	-3.87	0.78	-3.48	0.00	0.00
Coil Tray 2, Part D	Aluminum	6.98	10.80	-5.40	-5.87	0.47	-5.64	0.00	0.00
Coil Tray 2, Part E	Aluminum	6.98	10.80	-23.40	-23.87	0.47	-23.64	0.00	0.00
Coil Tray 2, Part F	Aluminum	7.98	11.11	-30.65	-31.97	1.31	-31.31	0.00	0.00

Table B.2: Parameters which define the cylinders or rings parallel to 9.5°axis. All dimensions of length are in cm.

Part Name	Material	Inner Radius	Outer Radius	z_0	z_F	Length	Center Along z	Offset x Dir.	Offset y Dir.
Magnet Coil 8	Copper	7.00	10.15	1.75	-1.75	3.50	0.00	-0.25	0.00
Coil Tray 3, Part N	Aluminum	6.58	7.00	2.46	-2.46	4.93	0.00	-0.25	0.00
Coil Tray 3, Part O	Aluminum	10.95	12.83	1.98	-1.98	3.96	0.00	-0.25	0.00
Coil Tray 3, Part P	Aluminum	7.00	9.00	-1.75	-2.25	0.50	-2.00	-0.25	0.00
Coil Tray 3, Part Q	Aluminum	7.00	9.00	2.25	1.75	0.50	2.00	-0.25	0.00

Table B.3: Parameters which define the cylinders or rings parallel to 4.75°axis. All dimensions of length are in cm.

Part Name	Material	x^0	x^F	y^0	y^F	z^0	z^F	Offset x Dir.	Offset y Dir.
Active Area Bare APD 1	Silicon	-1.40	1.40	-1.40	1.40	3.90	3.89	3.01	-1.74
Active Area Bare APD 2	Silicon	-1.40	1.40	-1.40	1.40	3.90	3.89	-3.01	-1.74
Active Area Bare APD 3	Silicon	-1.40	1.40	-1.40	1.40	3.90	3.89	0.00	3.47
Si Bare APD 1	Silicon	-1.52	1.52	-1.52	1.52	3.90	3.89	3.01	-1.74
Si Bare APD 2	Silicon	-1.52	1.52	-1.52	1.52	3.90	3.89	-3.01	-1.74
Si Bare APD 3	Silicon	-1.52	1.52	-1.52	1.52	3.90	3.89	0.00	3.47
BAPD Backing 1	Aluminum Oxide	-1.70	1.70	-1.70	1.70	3.89	3.80	3.01	-1.74
BAPD Backing 2	Aluminum Oxide	-1.70	1.70	-1.70	1.70	3.89	3.80	-3.01	-1.74
BAPD Backing 3	Aluminum Oxide	-1.70	1.70	-1.70	1.70	3.89	3.80	0.00	3.47
G10 BAPD Back Pieces 1	G10	-1.69	1.69	-2.51	2.51	3.80	3.17	3.01	-1.74
G10 BAPD Back Pieces 2	G10	-1.69	1.69	-2.51	2.51	3.80	3.17	-3.01	-1.74
G10 BAPD Back Pieces 3	G10	-1.69	1.69	-2.51	2.51	3.80	3.17	0.00	3.47
Si Small APD 1	Silicon	-0.84	0.84	-0.78	0.78	32.43	32.40	1.09	4.08
Si Small APD 2	Silicon	-0.84	0.84	-0.78	0.78	32.43	32.40	2.99	2.99
Si Small APD 3	Silicon	-0.84	0.84	-0.78	0.78	32.43	32.40	4.08	1.09
Si Small APD 4	Silicon	-0.84	0.84	-0.78	0.78	32.43	32.40	4.08	-1.09
Si Small APD 5	Silicon	-0.84	0.84	-0.78	0.78	32.43	32.40	2.99	-2.99
Si Small APD 6	Silicon	-0.84	0.84	-0.78	0.78	32.43	32.40	1.09	-4.08
Si Small APD 7	Silicon	-0.84	0.84	-0.78	0.78	32.43	32.40	-1.09	-4.08

Part Name	Material	x^0	x^F	y^0	y^F	z^0	z^F	Offset x Dir.	Offset y Dir.
Si Small APD 8	Silicon	-0.84	0.84	-0.78	0.78	32.43	32.40	-2.99	-2.99
Si Small APD 9	Silicon	-0.84	0.84	-0.78	0.78	32.43	32.40	-4.08	-1.09
Si Small APD 10	Silicon	-0.84	0.84	-0.78	0.78	32.43	32.40	-4.08	1.09
Si Small APD 11	Silicon	-0.84	0.84	-0.78	0.78	32.43	32.40	-2.99	2.99
Si Small APD 12	Silicon	-0.84	0.84	-0.78	0.78	32.43	32.40	-1.09	4.08
Small APD Backing 1	Aluminum Oxide	-0.84	0.84	-0.78	0.78	32.53	32.43	1.09	4.08
Small APD Backing 2	Aluminum Oxide	-0.84	0.84	-0.78	0.78	32.53	32.43	2.99	2.99
Small APD Backing 3	Aluminum Oxide	-0.84	0.84	-0.78	0.78	32.53	32.43	4.08	1.09
Small APD Backing 4	Aluminum Oxide	-0.84	0.84	-0.78	0.78	32.53	32.43	4.08	-1.09
Small APD Backing 5	Aluminum Oxide	-0.84	0.84	-0.78	0.78	32.53	32.43	2.99	-2.99
Small APD Backing 6	Aluminum Oxide	-0.84	0.84	-0.78	0.78	32.53	32.43	1.09	-4.08
Small APD Backing 7	Aluminum Oxide	-0.84	0.84	-0.78	0.78	32.53	32.43	-1.09	-4.08
Small APD Backing 8	Aluminum Oxide	-0.84	0.84	-0.78	0.78	32.53	32.43	-2.99	-2.99
Small APD Backing 9	Aluminum Oxide	-0.84	0.84	-0.78	0.78	32.53	32.43	-4.08	-1.09
Small APD Backing 10	Aluminum Oxide	-0.84	0.84	-0.78	0.78	32.53	32.43	-4.08	1.09
Small APD Backing 11	Aluminum Oxide	-0.84	0.84	-0.78	0.78	32.53	32.43	-2.99	2.99
Small APD Backing 12	Aluminum Oxide	-0.84	0.84	-0.78	0.78	32.53	32.43	-1.09	4.08
BGO Crystal 1	BGO	-0.60	0.60	-0.60	0.60	32.40	12.40	1.09	4.08
BGO Crystal 2	BGO	-0.60	0.60	-0.60	0.60	32.40	12.40	2.99	2.99
BGO Crystal 3	BGO	-0.60	0.60	-0.60	0.60	32.40	12.40	4.08	1.09
BGO Crystal 4	BGO	-0.60	0.60	-0.60	0.60	32.40	12.40	4.08	-1.09
BGO Crystal 5	BGO	-0.60	0.60	-0.60	0.60	32.40	12.40	2.99	-2.99
BGO Crystal 6	BGO	-0.60	0.60	-0.60	0.60	32.40	12.40	1.09	-4.08
BGO Crystal 7	BGO	-0.60	0.60	-0.60	0.60	32.40	12.40	-1.09	-4.08
BGO Crystal 8	BGO	-0.60	0.60	-0.60	0.60	32.40	12.40	-2.99	-2.99
BGO Crystal 9	BGO	-0.60	0.60	-0.60	0.60	32.40	12.40	-4.08	-1.09
BGO Crystal 10	BGO	-0.60	0.60	-0.60	0.60	32.40	12.40	-4.08	1.09
BGO Crystal 11	BGO	-0.60	0.60	-0.60	0.60	32.40	12.40	-2.99	2.99
BGO Crystal 12	BGO	-0.60	0.60	-0.60	0.60	32.40	12.40	-1.09	4.08

Table B.4: Parameters which define the boxes parallel to the z axis. All dimensions of length are in cm.
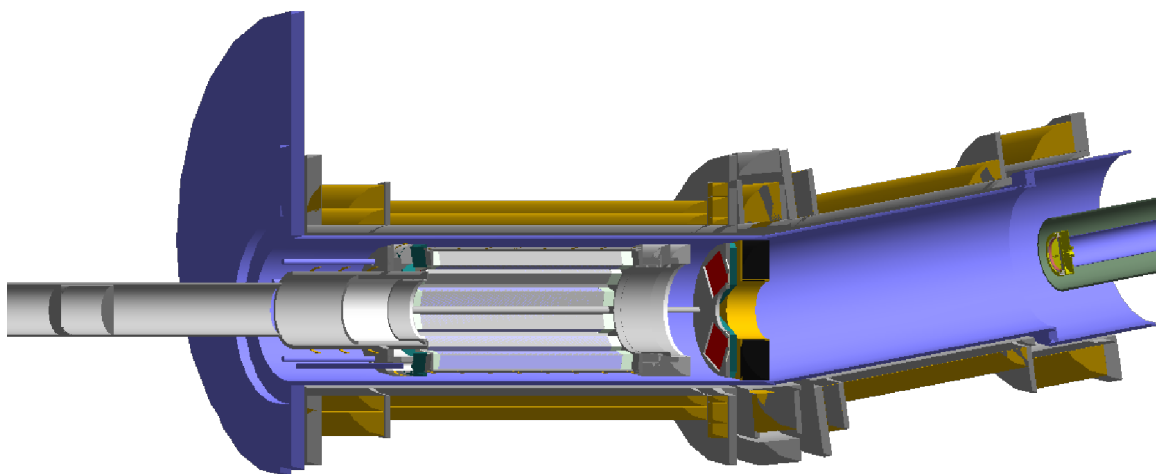
Figure B.1: Cross section rendering of the Geant4 model of the RDK II apparatus.

Bibliography

[1] A. I. Frank, Sov. Phys. Usp. **25**, 280 (May 1982)

[2] J. S. Nico, J. Phys. G **36**, 104001 (2009)

[3] M. E. Peskin and D. V. Schroeder, *An Introduction to Quantum Field Theory* (Westview Press, 1995)

[4] S. Weinberg, *The Quantum Theory of Fields* (Cambridge University Press, 1995)

[5] J. S. Nico, M. S. Dewey, T. R. Gentile, H. P. Mumm, A. K. Thompson, B. M. Fisher, I. Kremsky, F. E. Wietfeldt, T. E. Chupp, R. L. Cooper, E. J. Beise, K. G. Kiriluk, J. Byrne, and K. J. Coakley, Nature **444**, 1059 (Dec. 2006)

[6] R. L. Cooper, T. E. Chupp, M. S. Dewey, T. R. Gentile, H. P. Mumm, J. S. Nico, A. K. Thompson, B. M. Fisher, I. Kremsky, F. E. Wietfeldt, E. J. Beise, K. G. Kiriluk, J. Byrne, K. J. Coakley, and C. Fu, Phys. Rev. C **81** (Mar. 2010)

[7] V. Bernard, S. Gardner, U. G. Meißner, and C. Zhang, Phys. Lett. B **593**, 105 (Oct. 2004)

[8] Y. Gaponov and R. Khafizov, Nucl. Instrum. Methods A **440**, 557 (Feb. 2000)

[9] R. L. Cooper, *The Radiative Decay Mode of the Free Neutron*, PhD dissertation, University of Michigan, Department of Physics (2008)

[10] S. Gardner and D. He, Phys. Rev. D **87**, 116012 (Jun. 2013)

[11] S. Gardner and D. He, Phys. Rev. D **86**, 016003 (Jul. 2012)

[12] P. Ade *et al.* (Planck Collaboration)(2013), arXiv:1303.5062 [astro-ph.CO]

[13] E. Rutherford, Proc. R. Soc. London, Ser. A **97**, 374 (1920)

[14] W. Bothe and H. Becker, Z. Phys. **66**, 289 (May 1930)

[15] I. Joliot-Curie and F. Joliot, C. R. Acad. Sci. **194**, 273 (1932)

[16] J. Chadwick, Proc. R. Soc. London, Ser. A **136**, 692 (1932)

[17] J. Chadwick, Proc. R. Soc. London, Ser. A **142**, 1 (1933)

[18] M. Gell-Mann, Phys. Lett. **8**, 214 (1964), ISSN 0031-9163

[19] G. Zweig, *An SU(3) model for strong interaction symmetry and its breaking. Version 1*, Tech. Rep. (CERN, 1964) CERN-TH-401

[20] J. Beringer *et al.*, Phys. Rev. D **86**, 1528 (Jul. 2012), `http://pdg.lbl.gov`

[21] J. Campbell, *Rutherford Scientist Supreme* (AAS Publications, 1999)

[22] C. Jensen and F. Aaserud, *Controversy and Consensus: Nuclear Beta Decay 1911-1934* (Basel, 2000)

[23] L. M. Brown, Phys. Today(Sep. 1978)

[24] F. L. Wilson, Am. J. Phys. **36**, 1150 (Dec. 1968)

[25] J. Chadwick and M. Goldhaber, Nature **134**, 237 (Apr. 1934)

[26] A. Snell and L. Miller, Phys. Rev. **74** (1948)

[27] A. H. Snell, F. Pleasonton, and R. V. McCord, Phys. Rev. **78**, 310 (May 1950)

[28] J. M. Robson, Phys. Rev. **77**, 747 (1950)

[29] J. M. Robson, Phys. Rev. **78**, 311 (May 1950)

[30] P. E. Spivak, A. N. Sosnovskii, Y. A. Profok'ev, and V. S. Sokolov, in *Peaceful Uses of Atomic Energy: Proc. of Int. Conf. on the peaceful use of atomic energy, Geneva, 1955*, Vol. 2 (United Nations, NY, 1956) p. 33

[31] J. M. Robson, Phys. Rev. **82**, 306 (1951)

[32] T. D. Lee and C. N. Yang, Phys. Rev. **104**, 254 (Oct. 1956)

[33] C. S. Wu, E. Ambler, R. W. Hayward, D. D. Hoppes, and R. P. Hudson, Phys. Rev. **105**, 1413 (Feb. 1957)

[34] M. Goldhaber, L. Grodzins, and A. W. Sunyar, Phys. Rev. **109**, 1015 (Feb. 1958)

[35] M. T. Burgy, V. E. Krohn, T. B. Novey, G. R. Ringo, and V. L. Telegdi, Phys. Rev. **120**, 1829 (Dec. 1960)

[36] P. J. Mohr, B. N. Taylor, and D. B. Newell, Rev. Mod. Phys. **84**, 1527 (Nov. 2012)

[37] W. J. Marciano and A. Sirlin, Phys. Rev. Lett. **96** (Jan. 2006)

[38] W. J. Marciano, Physics Procedia **51**, 19 (2014), ISSN 1875-3892

[39] A. T. Yue, M. S. Dewey, D. M. Gilliam, G. L. Greene, A. B. Laptev, J. S. Nico, W. M. Snow, and F. E. Wietfeldt, Phys. Rev. Lett. **111**, 222501 (Nov. 2013)

[40] J. D. Jackson, S. B. Treiman, and H. W. Wyld, Phys. Rev. **106**, 517 (May 1957)

[41] J. Jackson, S. Treiman, and H. W. Jr., Nuc. Phys. **4**, 206 (1957)

[42] P. A. M. Dirac, Proc. R. Soc. London, A **114**, 243 (1927)

[43] E. Fermi, Rev. Mod. Phys. **4**, 87 (Jan. 1932)

[44] W. Heisenberg and W. Pauli, Z. Phys. **56**, 1 (Jan. 1929)

[45] W. Heisenberg and W. Pauli, Z. Phys. **59**, 168 (Mar. 1930)

[46] J. R. Oppenheimer, Phys. Rev. **35**, 461 (Mar. 1930)

[47] F. Bloch and A. Nordsieck, Phys. Rev. **52**, 54 (Jul. 1937)

[48] D. Hanneke, S. Fogwell Hoogerheide, and G. Gabrielse, Phys. Rev. A **83**, 052122 (May 2011)

[49] G. Aston, Proc. Cambridge Philos. Soc. **23**, 935 (Jul. 1927)

[50] V. Bernard, S. Gardner, U. G. Meißner, and C. Zhang, Phys. Lett. B **599**, 348 (2004)

[51] A. N. Ivanov, M. Pitschmann, and N. I. Troitskaya, Phys. Rev. D **88** (Oct. 2013)

[52] M. Beck, J. Byrne, R. Khafizov, V. Kozlov, Y. Mostovoi, O. Rozhnov, N. Severijns, and V. Solovei, JETP Lett. **76**, 332 (2002)

[53] J. S. Nico, M. Arif, M. S. Dewey, T. R. Gentile, D. M. Gilliam, P. R. Huffman, D. L. Jacobson, , and A. K. Thompson, Journal of Research of NIST **110**, 137 (May 2005)

[54] J. Nico, M. Dewey, D. Gilliam, F. Wietfeldt, X. Fei, W. Snow, G. Greene, J. Pauwels, R. Eykens, A. Lamberty, J. Gestel, and R. Scott, Phys. Rev. C **71** (May 2005)

[55] R. L. Cooper, R. Alarcon, M. J. Bales, C. D. Bass, E. J. Beise, H. Breuer, J. Byrne, T. E. Chupp, K. J. Coakley, M. S. Dewey, C. Fu, T. R. Gentile, H. P. Mumm, J. S. Nico, B. O'Neill, K. Pulliam, A. K. Thompson, and F. E. Wietfeldt, Nucl. Instrum. Methods A **691**, 64 (Nov. 2012)

[56] B. O'Neill, *Precision Measurement of the Radiative Decay Mode of the Free Neutron*, PhD dissertation, Arizona State University, Department of Physics (2012)

[57] R. E. Williams (Presented at the Neutron Summer School at NIST Gaithersburg, MD, 2007)

[58] K.-J. Kügler, W. Paul, and U. Trinks, Z. Phys. B **39**, 361 (1980)

[59] G. Ferguson, *5T Bent Magnet and Cryostat: Operator's Manual PN: 35913* (Oxford Instruments, 1992)

[60] J. Byrne, P. Dawber, M. van der Grinten, C. Habeck, F. Shaikh, J. Spain, R. Scott, C. Baker, K. Green, and O. Zimmer, J. Phys. G **28**, 1325 (Jun. 2002)

[61] J. Byrne, P. G. Dawber, C. G. Habeck, S. J. Smidt, J. A. Spain, and A. P. Williams, Europhys. Lett. **33**, 187 (1996)

[62] G. Knoll, *Radiation Detection and Measurement*, 4th ed. (Wiley, 2010) ISBN 978-0470131480

[63] "ORTEC," http://www.ortec-online.com/, Accessed: Jun 2014

[64] T. R. Gentile, M. S. Deweya, H. P. Mumm, J. S. Nico, A. K. Thompson, T. E. Chupp, R. L. Cooper, B. M. Fisher, I. Kremsky, F. E. Wietfeldt, K. G. Kiriluk, and E. J. Beise, Nucl. Instrum. Methods A **579**, 447 (Aug. 2007)

[65] H. V. Piltningsrud, J. Nucl. Med. **20**, 1279 (1979)

[66] G. Keil, Nucl. Instrum. Methods **89**, 111 (1970)

[67] W. W. Moses, S. A. Payne, W. S. Choong, G. Hull, and B. W. Reutter, IEEE Trans. Nucl. Sci. **55**, 1049 (Jun. 2008)

[68] M. Moszynski, M. Balcerzyk, W. Czarnacki, M. Kapusta, W. Klamra, A. Syntfeld, and M. Szawlowski, IEEE Trans. Nucl. Sci. **51**, 1074 (Jun. 2004)

[69] I. V. Khodyuk and P. Dorenbos, IEEE Trans. Nucl. Sci. **59**, 3320 (Dec. 2012)

[70] E. Sysoeva, O. Zelenskaya, and E. Sysoeva, IEEE Trans. Nucl. Sci. **43**, 1282 (Jun. 1996)

[71] M. A. Verdier, P. C. F. Di Stefano, P. Nadeau, C. Behan, M. Clavel, and C. Dujardin, Phys. Rev. B **84** (Dec. 2011)

[72] V. V. Averkiev, V. K. Lyapidevskii, and G. K. Salakhutdinov, Prib. Tekh. E ksp. [Instrum. Exp. Tech. (USSR)] **33**, 80 (Jul. 1990)

[73] T. Gentile, M. J. Bales, H. Breuer, T. E. Chupp, K. J. Coakley, R. L. Cooper, J. S. Nico, and B. O'Neill, "Nonproportionality in the scintillation light yield of bismuth germanate," (2014), manuscript in preparation

[74] T. R. Gentile, C. D. Bass, J. S. Nico, H. Breuer, and R. Farrell, Nucl. Instrum. Methods A **652**, 520 (Oct. 2011)

[75] T. R. Gentile, M. Bales, U. Arp, B. Dong, and R. Farrell, Rev. Sci. Instrum. **83** (May 2012)

[76] S. Agostinelli *et al.*, Nucl. Instrum. Methods A **506**, 250 (2003)

[77] "Geant4," http://geant4.cern.ch/, Accessed: Jun 2014

[78] R. Brun and F. Rademakers, Nucl. Instrum. Methods A **389**, 81 (1997), new Computing Techniques in Physics Research V

[79] "ROOT," http://root.cern.ch/drupal/, Accessed: Jun 2014

[80] A. Lechner, M. G. Pia, and M. Sudhakar, IEEE Trans. Nucl. Sci. **56**, 398 (Apr. 2009), ISSN 0018-9499

[81] G. Soti, F. Wauters, M. Breitenfeldt, P. Finlay, I. Kraev, A. Knecht, T. Porobić, D. Zákoucký, and N. Severijns, Nucl. Instrum. Methods A **728**, 11 (Jun. 2013)

[82] "BiotSavart," http://www.ripplon.com/BiotSavart/, Accessed: Jun 2014

[83] "IGOR Pro," http://www.wavemetrics.com/products/igorpro/igorpro.htm, Accessed: Jun 2014

[84] "COMSOL Multiphysics Ver. 4.3b," http://www.comsol.com/, Accessed: Jun 2014

[85] M. Matsumoto and T. Nishimura, ACM Trans. Model. Comput. Simul. **8**, 3 (Jan. 1998)

[86] "RANDOM.ORG," http://www.random.org/, Accessed: Jun 2014

[87] J. D. Jackson, *Classical Electrodynamics*, 3rd ed. (Wiley, 1998)

[88] T. G. Northrop and E. Teller, Phys. Rev. **117**, 215 (Jan 1960)

[89] D. J. Griffiths, *Introduction to Electrodynamics*, 3rd ed. (Addison Wesley, 1999)

[90] J. Butcher, Appl. Numer. Math. **20**, 247 (1996)

[91] W. H. Press, B. P. Flannery, S. A. Teukolsky, and W. T. Vetterling, *Numerical Recipes in C*, 2nd ed. (Cambridge University Press, 1992)

[92] D. E. Cullen *et al.*, *Tables and Graphs of Atomic Subshell and Relaxation Data Derived from the LLNL Evaluated Atomic Data Library (EADL), Z = 1 - 100*, Tech. Rep. UCRL-50400, Vol. 30 (Lawrence Livermore National Laboratory, 1991)

[93] D. E. Cullen, S. Perkins, and S. M. Seltzer, *Tables and Graphs of Electron Interaction Cross 10 eV to 100 GeV Derived from the LLNL Evaluated Electron Data Library (EEDL), Z = 1 - 100*, Tech. Rep. UCRL-50400, Vol. 31 (Lawrence Livermore National Laboratory, 1991)

[94] D. E. Cullen, J. H. Hubbel, and L. Kissel, *EPDL97: the evaluated photo data library '97 version*, Tech. Rep. UCRL-50400, Vol. 6 (Lawrence Livermore National Laboratory, 1997)

[95] V. Ivanchenko, D. Wright, and M. Maire, Physics Reference Manual: Geant4(Dec. 2012)

[96] O. Klein and Y. Nishina., Z. Phys. **52**, 853 (1929)

[97] J. Martin, J. Yuan, S. Hoedl, B. Filippone, D. Fong, T. Ito, E. Lin, B. Tipton, and A. Young, Phys. Rev. C **68** (Nov. 2003)

[98] J. Martin, J. Yuan, M. Betancourt, B. Filippone, S. Hoedl, T. Ito, B. Plaster, and A. Young, Phys. Rev. C **73** (Jan. 2006)

[99] O. Kadri, V. N. Ivanchenko, F. Gharbi, and A. Trabelsi, Nucl. Instrum. Methods B **258**, 381 (May 2007)

[100] A. Akkerman, M. Murat, and J. Barak, J. Appl. Phys. **106** (Dec. 2009)

[101] X-5 Monte Carlo Team, *MCNP - A General Monte Carlo N-Particle Transport Code, Version 5*, Los Alamos National Laboratory (Apr 2003)

[102] M. Dewey, K. Coakley, D. Gilliam, G. Greene, A. Laptev, J. Nico, W. Snow, F. Wietfeldt, and A. Yue, Nucl. Instrum. Methods A **611**, 189 (Dec. 2009)

[103] W. Mampe, L. N. Bondarenko, V. I. Morozov, Y. N. Panin, and A. I. Fomin, JETP Lett. **57**, 82 (Jan 1993)

[104] J. Byrne, P. G. Dawber, C. G. Habeck, S. J. Smidt, J. A. Spain, and A. P. Williams, Europhys. Lett. **33**, 187 (Jan 1996)

[105] A. Serebrov, V. Varlamov, A. Kharitonov, A. Fomin, Y. Pokotilovski, P. Geltenbort, J. Butterworth, I. Krasnoschekova, M. Lasakov, R. Tal'daev, A. Vassiljev, and O. Zherebtsov, Phys. Lett. B **605**, 72 (Jan 2005)

[106] A. Pichlmaier, V. Varlamov, K. Schreckenbach, and P. Geltenbort, Phys. Lett. B **693**, 221 (Oct 2010)

[107] S. S. Arzumanov, L. N. Bondarenko, V. I. Morozov, Y. N. Panin, and S. M. Chernyavsky, JETP Lett. **95**, 224 (May 2012)

[108] *Germanium Detectors*, Tech. Rep. C39606 (Canberra Industries, Inc, 2014)

[109] J. dos Santos, C. Monteiro, R. Morgado, and C. Conde, Appl. Radiat. and Isotopes **53**, 739 (2000)

[110] M. Agnello, E. Botta, T. Bressani, M. Bruschi, S. Bufalino, M. D. Napoli, A. Feliciello, A. Fontana, B. Giacobbe, L. Lavezzi, G. Raciti, E. Rapisarda, A. Rotondi, C. Sbarra, C. Sfienti, and A. Zoccoli, Nucl. Instrum. Methods A **606**, 560 (2009)

[111] O. Zimmer, P. Hautle, W. Heil, D. Hofmann, H. Humblot, I. Krasnoschekova, M. Lasakov, T. Müller, V. Nesvizhevsky, J. Reich, A. Serebrov, Y. Sobolev, and A. Vassilev, Nucl. Instrum. Methods A **440**, 764 (2000)

[112] F. E. Wietfeldt, J. Byrne, B. Collett, M. S. Dewey, G. L. Jones, A. Komives, A. Laptev, J. S. Nico, G. Noid, E. J. Stephenson, I. Stern, C. Trull, and B. G. Yerozolimsky, Nucl. Instrum. Methods A **611**, 207 (Dec. 2009)

[113] D. Počanić, R. Alarcon, L. Alonzi, S. Baeßler, S. Balascuta, J. Bowman, M. By-chkov, J. Byrne, J. Calarco, V. Cianciolo, C. Crawford, E. Frlež, M. Gericke, G. Greene, R. Grzywacz, V. Gudkov, F. Hersman, A. Klein, J. Martin, S. Page, A. Palladino, S. Penttilä, K. Rykaczewski, W. Wilburn, A. Young, and G. Young, Nucl. Instrum. Methods A **611**, 211 (2009)

[114] J. C. Hardy and I. S. Towner, Phys. Rev. Lett. **94**, 092502 (Mar 2005)

[115] K. P. Hickerson, *The Physics of Ultracold Neutrons and Fierz Interference in Beta Decay*, PhD dissertation, California Institute of Technology, Department of Physics and Astronomy (2012)